

**FINITE ELEMENT ANALYSIS OF REINFORCED CONCRETE AND STEEL FIBER  
REINFORCED CONCRETE SLABS IN PUNCHING SHEAR**

By

© Todd Puddicome, B.Eng.

A thesis submitted to the  
School of Graduate Studies  
in partial fulfillment of the requirements for the degree of

**Master of Engineering**  
**Faculty of Engineering and Applied Science**  
Memorial University of Newfoundland

**May 2018**

St. John's

Newfoundland

Canada

# Abstract

Punching shear capacity of reinforced concrete slabs is influenced by the following material properties: concrete compressive strength, flexural reinforcement ratio, inclusion of steel fibers in the concrete mix, and the reinforcing steel yield strength. A review of current finite element analysis models reveals that a unified approach to include all of these variables into one coherent model does not exist.

This thesis presents a finite element model capable of making accurate predictions on the ultimate punching shear load and load – deflection response of a reinforced concrete slab. The model simulates the nonlinear constitutive properties of reinforced concrete by proposing a robust model to represent the behavior through the Concrete Damaged Plasticity (CDP) constitutive model. The thesis defines the parameters for the CDP model in a finite element analysis and develops an expression to mitigate mesh size dependency. A tension – stiffening model is proposed using an exponential decay expression with variables to account for varying concrete compressive strength, flexural reinforcement ratio, inclusion of steel fibers in the concrete mix, and the reinforcing steel yield strength. The model is calibrated using a series of experimental data from the literature and validated by successfully replicating the punching shear behavior of experimental specimens data from the literature.

# Acknowledgements

The author would like to express his sincere gratitude to his supervisor Dr. Amgad Hussein for his patience, guidance, friendship, and true passion for advancing engineering education.

To my parents. I am always keenly aware that any success I may enjoy, whether personal or career achievements, all stem from growing up in an incredibly positive and supportive family environment.

# Contents

|  |      |
|--|------|
| Abstract .....   | i    |
| Acknowledgements .....                                       | ii   |
| Contents .....   | iii  |
| List of Tables .....   | vii  |
| List of Figures .....  | viii |
| List of Symbols .....  | xii  |
| 1 Introduction .....   | 1    |
| 1.1 General.....   | 1    |
| 1.2 Scope & Objectives .....                                 | 2    |
| 1.3 Thesis Outline.....                                      | 3    |
| 2 Literature Review .....                                    | 5    |
| 2.1 Punching Shear Failure Mechanism.....                    | 5    |
| 2.2 Variables that Influence Punching Shear Resistance ..... | 6    |
| 2.2.1 Concrete Strength.....                                 | 6    |
| 2.2.2 Flexural Reinforcement Ratio.....                      | 7    |
| 2.2.3 Column Size & Shape.....                               | 9    |
| 2.2.4 Size Effect.....                                       | 9    |
| 2.2.5 Flexural Reinforcement Yield Strength .....            | 10   |
| 2.2.6 Steel Fibers.....                                      | 10   |
| 2.3 Concrete in Compression .....                            | 11   |
| 2.3.1 Behavior of Normal Concrete in Compression.....        | 11   |
| 2.3.2 Behavior of SFRC in Compression.....                   | 13   |

|       |   |    |
|-------|---|----|
| 2.4   | Concrete in Tension .....                               | 16 |
| 2.4.1 | Tension Softening of Normal Concrete .....              | 16 |
| 2.4.2 | Tension Softening of SFRC .....                         | 20 |
| 2.4.3 | Tension Stiffening of Normal Reinforced Concrete .....  | 21 |
| 2.4.4 | Tension Stiffening of Reinforced SFRC .....             | 26 |
| 2.4.5 | Peak Tensile Strength .....                             | 30 |
| 2.5   | Literature Review of Punching Shear FEA .....           | 32 |
| 2.5.1 | Winkler & Stangenberg [53] .....                        | 33 |
| 2.5.2 | Youm et al [54] .....                                   | 35 |
| 2.5.3 | Wosatko et al [55] .....                                | 37 |
| 2.5.4 | Genikomsou & Polak [56] [57] [58] [59] .....            | 39 |
| 2.5.5 | Nana et al [61] .....                                   | 47 |
| 2.5.6 | Hawileh et al [62] .....                                | 49 |
| 2.5.7 | Summary .....   | 51 |
| 3     | Data Used in the Current Study .....                    | 52 |
| 3.1   | McHarg et al [19] .....                                 | 53 |
| 3.2   | Lee et al [20] .....                                    | 57 |
| 3.3   | Yang et al [18] .....                                   | 59 |
| 3.4   | Pourezza [63] .....                                     | 62 |
| 3.5   | Summary of Experimental Data .....                      | 63 |
| 4     | FEA Modelling of Reinforced Concrete .....              | 64 |
| 4.1   | Concrete Constitutive Model .....                       | 64 |
| 4.1.1 | Numerical Model for Concrete Compressive Behavior ..... | 72 |
| 4.1.2 | Numerical Model for Concrete Tensile Behavior .....     | 74 |

|       |   |     |
|-------|---|-----|
| 4.2   | Reinforcement Modelling .....                         | 77  |
| 4.3   | Finite Element Type .....                             | 79  |
| 4.4   | Finite Element Discretization.....                    | 79  |
| 4.5   | Boundary Conditions and Load Application.....         | 85  |
| 4.6   | Failure Criteria .....                                | 87  |
| 5     | Proposed Finite Element Model .....                   | 89  |
| 5.1   | Concrete Compressive Strength Parameter.....          | 89  |
| 5.1.1 | Modeling Concrete Behavior in Compression.....        | 90  |
| 5.1.2 | Modeling Concrete Behavior in Tension.....            | 91  |
| 5.1.3 | Results and Calibration.....                          | 92  |
| 5.2   | Flexural Reinforcement Ratio Parameter.....           | 100 |
| 5.3   | SFRC Fiber Volume Parameter.....                      | 107 |
| 5.3.1 | Modeling SFRC Behavior in Compression .....           | 108 |
| 5.3.2 | Modeling SFRC Behavior in Tension.....                | 109 |
| 5.3.3 | Results and Calibration.....                          | 109 |
| 5.4   | Flexural Reinforcement Yield Strength Parameter ..... | 113 |
| 5.5   | Tension-Stiffening Model Summary.....                 | 119 |
| 6     | Finite Element Model Verification.....                | 121 |
| 6.1   | Specimen FSB .....                                    | 121 |
| 6.2   | Specimen FCU .....                                    | 121 |
| 6.3   | Specimen FCB.....                                     | 123 |
| 6.4   | Specimen 90BF .....                                   | 124 |
| 6.5   | Specimen MU2.....                                     | 125 |
| 6.6   | Specimen MB2.....                                     | 127 |

|      |                                     |     |
|------|-------------------------------------|-----|
| 6.7  | Specimen MBF2.....                  | 128 |
| 6.8  | Specimen SB1 .....                  | 129 |
| 6.9  | Specimen R200 .....                 | 131 |
| 6.10 | Summary of Model Verification ..... | 133 |
| 7    | Conclusions & Recommendations.....  | 134 |
| 8    | References .....                    | 137 |

# List of Tables

|   |     |
|---|-----|
| Table 2.1: Models for the compressive behavior of concrete..... | 12  |
| Table 2.2: Models for the compressive behavior of SFRC.....     | 14  |
| Table 3.1: Summary of slab specimen properties.....             | 63  |
| Table 6.1: Tension Stiffening Properties FCU .....              | 122 |
| Table 6.2: Tension Stiffening Properties FCB.....               | 123 |
| Table 6.3: Summary of FEA vs Experimental Results.....          | 133 |

# List of Figures

|  |    |
|--|----|
| Figure 2-1: Critical shear crack [2].  | 6  |
| Figure 2-2: Stress – strain curve for concrete in compression.                           | 12 |
| Figure 2-3: Hillerborg’s Fictitious Crack Model [33].                                    | 19 |
| Figure 2-4: Bilinear stress – COD relation [35].   | 20 |
| Figure 2-5: Tension stiffening curve for reinforced concrete [25].                       | 22 |
| Figure 2-6: Tension softening and tension stiffening response [41].                      | 23 |
| Figure 2-7: Tension stiffening models: a) Scanlon & Murray [39] b) Lin & Scordelis [40]. | 23 |
| Figure 2-8: Tension stiffening model template [41].                                      | 24 |
| Figure 2-9: Nayal & Rasheed model calibration [41].                                      | 25 |
| Figure 2-10: Hsu & Mo weakening function for tension stiffening [44].                    | 26 |
| Figure 2-11: Distribution of stresses between cracks [31].                               | 27 |
| Figure 2-12: Abrishami & Mitchell tension stiffening results [45].                       | 28 |
| Figure 2-13: Tension stiffening of SFRC [31].  | 29 |
| Figure 2-14: Tension stiffening model SFRC vs RC [46].                                   | 30 |
| Figure 2-15: Parametric study of dilation angle [54].                                    | 36 |
| Figure 2-16: Youm load – displacement results [54].                                      | 37 |
| Figure 2-17: Wosatko finite element model [55].  | 38 |
| Figure 2-18: Load – deflection comparison of static vs quasi static [56].                | 40 |
| Figure 2-19: Influence of viscosity on load – deflection [56].                           | 41 |
| Figure 2-20: Influence of flexural reinforcement ratio [56].                             | 41 |
| Figure 2-21: Stress vs crack opening displacement [57].                                  | 42 |
| Figure 2-22: Bilinear strain softening diagram [57].                                     | 43 |
| Figure 2-23: Strain-softening curves [58].   | 45 |

|   |    |
|---|----|
| Figure 2-24: Genikomsou & Polak load – displacement curve [58].               | 46 |
| Figure 2-25: Nana FEA vs experimental results [61].                           | 48 |
| Figure 2-26: Hawileh FEA vs experimental results [62].                        | 51 |
| Figure 3-1: McHarg slab specimens [19].                                       | 55 |
| Figure 3-2: McHarg load deflection results [19].                              | 56 |
| Figure 3-3: Lee slab specimens [20].  | 58 |
| Figure 3-4: Lee load – deflection results [20].                               | 59 |
| Figure 3-5: Yang slab specimens [18].   | 60 |
| Figure 3-6: Yang load – deflection response [18].                             | 61 |
| Figure 3-7: Pourezza load vs deflection curves [63].                          | 62 |
| Figure 4-1: Drucker-Prager boundary surface [68].                             | 66 |
| Figure 4-2: Deviatoric cross-section of failure surface in CDP model [69].    | 67 |
| Figure 4-3: Concrete biaxial stress-strain curve [69].                        | 67 |
| Figure 4-4: Dilation angle in meridian plane.                                 | 68 |
| Figure 4-5: Parametric study – dilation angle specimen NU.                    | 69 |
| Figure 4-6: Parametric Study – dilation angle specimen SB1.                   | 70 |
| Figure 4-7: Viscosity parametric study using slab.                            | 71 |
| Figure 4-8: Compressive stress vs strain curve [69].                          | 74 |
| Figure 4-9: Tension stiffening curve with tensile damage [69].                | 76 |
| Figure 4-10: Modelling of reinforcement and its interface with concrete [71]. | 78 |
| Figure 4-11: Sample mesh size of 20 mm  | 81 |
| Figure 4-12: Parametric Study – mesh size.                                    | 82 |
| Figure 4-13: Mesh size calibration for 15 mm mesh.                            | 83 |
| Figure 4-14: Mesh size calibration for 25 mm mesh.                            | 84 |

|   |     |
|---|-----|
| Figure 4-15: Mesh size calibration for 30 mm mesh. ....                             | 84  |
| Figure 4-16: Weakening function vs mesh size. ....                                  | 85  |
| Figure 4-17: Test set-up [19]. ....   | 86  |
| Figure 4-18: Abaqus quarter slab model. ....  | 86  |
| Figure 5-1: Experimental results for uniform slabs [20]. ....                       | 90  |
| Figure 5-2: Specimen 30U FEA model compressive stress-strain diagram. ....          | 91  |
| Figure 5-3: Reference slab 30U tension stress-strain diagram. ....                  | 92  |
| Figure 5-4: Load vs displacement for 30U – varying $n$ . ....                       | 93  |
| Figure 5-5: Load vs displacement for 30U – varying $\gamma$ . ....                  | 94  |
| Figure 5-6: Calibrated load vs displacement for 30U. ....                           | 94  |
| Figure 5-7: FEA stress contours for 30U. ....                                       | 95  |
| Figure 5-8: Load vs displacement for 35U. ....                                      | 96  |
| Figure 5-9: Load vs displacement for 55U. ....                                      | 96  |
| Figure 5-10: Load vs displacement for 65U. ....                                     | 97  |
| Figure 5-11: Comparison of FEA models vs experimental data for U-series slabs. .... | 97  |
| Figure 5-12: Weakening function, $n$ vs concrete strength, $f_c'$ . ....            | 99  |
| Figure 5-13: Ultimate strain factor vs concrete strength. ....                      | 99  |
| Figure 5-14: Load vs displacement for 30B using 30U parameters. ....                | 102 |
| Figure 5-15: Load vs displacement for 30B – varying $n$ . ....                      | 102 |
| Figure 5-16: Load vs displacement for 30B – varying $\gamma$ . ....                 | 103 |
| Figure 5-17: Load vs displacement for 30B. ....                                     | 103 |
| Figure 5-18: load vs displacement for 35B. ....                                     | 104 |
| Figure 5-19: Load vs displacement for 55B. ....                                     | 104 |
| Figure 5-20: Load vs displacement for 65B. ....                                     | 105 |

|  |     |
|--|-----|
| Figure 5-21: Comparison of FEA model vs experimental data for B-series slabs. .... | 106 |
| Figure 5-22: Relationship for ‘n’. ....  | 106 |
| Figure 5-23: Relationship for ‘Y’. ....  | 107 |
| Figure 5-24: FEA slab FSU compressive stress-strain diagram. ....                  | 108 |
| Figure 5-25: FEA slab FSU tension stress-strain diagram.....                       | 109 |
| Figure 5-26: FSU Slab load vs displacement calibration for varying n.....          | 110 |
| Figure 5-27: FSU load vs displacement calibration for varying Y. ....              | 111 |
| Figure 5-28: FSU load vs displacement.....   | 111 |
| Figure 5-29: FEA stress contours for FSU. ....                                     | 112 |
| Figure 5-30: MU1 load vs displacement for n=0.4, Y=100.....                        | 116 |
| Figure 5-31: Influence on varying $f_y$ . ....                                     | 116 |
| Figure 5-32: FEA MU1 load – deflection calibration.....                            | 117 |
| Figure 5-33: $f_y$ calibration curve for $n$ . ....                                | 118 |
| Figure 5-34: $f_y$ variable calibration curve for Y. ....                          | 119 |
| Figure 6-1: FSB load vs displacement validation. ....                              | 122 |
| Figure 6-2: FEA Slab FCU load vs displacement.....                                 | 123 |
| Figure 6-3: FEA Slab FCB load vs displacement. ....                                | 124 |
| Figure 6-4: FEA Slab 90BF load vs displacement validation.....                     | 125 |
| Figure 6-5: FEA Slab MU2 load vs displacement. ....                                | 126 |
| Figure 6-6 FEA Slab MB2 load vs displacement. ....                                 | 128 |
| Figure 6-7: FEA Slab MBF2 load vs displacement. ....                               | 129 |
| Figure 6-8: Comparison of FEA tension stress-strain curves for SB1.....            | 130 |
| Figure 6-9: FEA SB1 Load vs Displacement verification. ....                        | 131 |
| Figure 6-10: FEA R200 load vs displacement verification. ....                      | 132 |

# List of Symbols

|                      |  |
|----------------------|--|
| $A_c$                | Concrete cross-sectional area  |
| $a_1$                | fraction of bond mobilized at first matrix cracking ( $\approx 0.5$ )            |
| $a_2$                | efficiency factor of fiber orientation in the un-cracked state ( $\approx 1.0$ ) |
| $b_o$                | Critical shear perimeter in punching shear                                       |
| $b_c$                | Ratio of plastic compressive strain to inelastic compressive strain              |
| $b_t$                | Ratio of plastic tensile strain to inelastic tensile strain                      |
| $c_1$                | Fictitious crack model parameter (3.00)  |
| $c_2$                | Fictitious crack model parameter (6.93)  |
| $\gamma$             | Ultimate strain factor   |
| $\gamma_c$           | Descent function   |
| $d$                  | Effective depth to the centroid of reinforcement                                 |
| $d_f$                | Diameter of steel fibers   |
| $d_a$                | Aggregate diameter   |
| $d_c$                | Concrete damage parameter in compressive   |
| $d_t$                | Concrete damage parameter in tension   |
| $E_{ci}$             | Modified concrete modulus of elasticity  |
| $\varepsilon_c$      | Concrete compressive strain  |
| $\varepsilon_c^{in}$ | Inelastic concrete strain  |
| $\varepsilon_c^{pl}$ | Plastic concrete strain  |
| $\varepsilon_{cr}$   | Cracking tensile strain  |
| $\varepsilon_o$      | Concrete strain  |

|                 |   |
|-----------------|---|
| $\varepsilon_u$ | Ultimate strain                                       |
| $\varepsilon_y$ | Yield strain  |
| $f'_c$          | Concrete compressive strength                         |
| $f_{cr}$        | Cracking tensile stress                               |
| $f_{ck}$        | Concrete characteristic compressive strength          |
| $f_{cm}$        | Average concrete cylinder strength                    |
| $f_{ct}$        | Peak concrete tensile stress                          |
| $f_{cu}$        | Concrete compressive strength at ultimate strain      |
| $f_{sp}$        | Concrete tensile splitting strength                   |
| $f_{ctm}$       | Average concrete tensile strength                     |
| $f_{cts}$       | Average concrete tensile strength of SFRC             |
| $f'_t$          | Peak concrete tensile stress                          |
| $f_y$           | Yield strength of steel                               |
| $f_{yf}$        | Yield strength of steel fibers                        |
| $G_f$           | Fracture energy of plain concrete                     |
| $G^I_f$         | Fictitious fracture energy of SFRC                    |
| $K_c$           | Shape factor in the Concrete Damaged Plasticity model |
| $\mu$           | Viscosity in the Concrete Damaged Plasticity model    |
| $\ell_c$        | Characteristic length                                 |
| $\ell_f$        | Length of steel fibers                                |
| $M$             | Bond parameter  |
| $n$             | Weakening function in concrete tensile stress-strain  |
| $n$             | Curve fitting factor                                  |

|               |  |
|---------------|--|
| $N_f$         | Axial force  |
| $\rho$        | Flexural reinforcement ratio   |
| $RI$          | Reinforcing index  |
| $\sigma_c$    | Concrete compressive stress  |
| $\sigma_t(w)$ | Concrete tensile stress at crack opening                             |
| $\tau$        | average interfacial bond strength of fiber matrix ( $\approx 2f_t$ ) |
| $V_f$         | Volume of steel fibers   |
| $\psi$        | Dilation angle in the Concrete Damaged Plasticity model              |
| $w$           | Crack opening width  |
| $w_c$         | Maximum crack opening width  |
| $w_1$         | Crack width at $f'_t/3$  |
| $w_u$         | Ultimate crack width   |
| $W_f$         | Weight percentage of steel fibers                                    |

# Chapter 1

## Introduction

### 1.1 General

Reinforced concrete slabs are important structural elements that have widespread use in building construction throughout the world. The efficiency of a reinforced concrete two-way slab is rarely ever realized through the flexure of the slab. Rather, the required design thickness is usually governed by the shear demands at the slab – column connection. In order to minimize the overall slab thickness, the designer must work to either reduce the shear stress concentration at the slab column interface or increase the slab shear resistance to prevent the column from the catastrophic failure of “punching” through the slab. This type of failure is brittle, providing very little warning to building occupants and can lead to a progressive collapse of the structure. Due to this danger, understanding and improving the shear capacity of reinforced concrete flat slabs is an area of considerable interest in the field of reinforced concrete research. To gain a better understanding of the behavior it is necessary to be able to accurately predict the overall elastic and inelastic deformation response of the slab as well as the punching shear strength.

Current design provisions for punching shear resistance of reinforced concrete slabs have been developed by empirical and statistical formulations derived through many years of experimental research. Despite the extensive amount of research on punching shear, there is still not a full understanding of this phenomenon. The development of reliable analytical techniques, such as finite element analysis (FEA), can reduce the time and cost of otherwise expensive experimental tests. An extensive amount of testing is required to cover the wide range of parameters that influence punching shear and gain an understanding of the behavior. Moreover,

physical modeling of punching shear slabs is time consuming and requires financial resources. As an alternative, finite element modeling can be used to supplement experimental studies. Finite element models are useful in being able to examine many parameters in a reasonable amount of time and can be based on realistic slab geometry that avoids the size effect encountered in small-scale physical models. Finite element models can also better simulate the loading and support conditions of an actual structure that could be limited by the constraints of a laboratory.

The challenge in using nonlinear finite element analysis is the proper selection of the material model that can represent the complex behavior of concrete. This complexity is due to the nonlinear behavior of concrete in compression and tension, tensile softening/stiffening, cracking and stiffness reduction, bond between concrete and reinforcing steel, aggregate interlock, and dowel action. The development of such a FEA model must first be calibrated with experimental results in order to establish the reliability of making predictions on the material's behavior.

## **1.2 Scope & Objectives**

The current thesis presents a finite element model that can predict the punching shear behavior of reinforced concrete slabs. The purposed model will predict, with reasonable accuracy, the ultimate load and load – deflection response of reinforced concrete slabs with varying the parameters that influence punching shear such as: concrete strengths, reinforcement ratios, steel fiber volume, and high strength steel reinforcement. A unified approach to include all of these variables into one general punching shear FEA model does not exist. This thesis will contribute to the research of FEA modelling of reinforced concrete by providing a punching shear model to fill this gap.

### 1.3 Thesis Outline

Chapter 2 contains the literature review. It begins with a discussion on the failure mechanism of punching shear and then precedes with a description of the variables that influence punching shear resistance and a description on the compressive and tensile behavior of concrete. Next, the literature review examines the use of finite element analysis to simulate the punching shear behavior of reinforced concrete flat slabs.

Chapter 3 describes the physical experiments and the test set-ups that are being modelled using finite element analysis and used to calibrate the material model that is proposed in the thesis.

Chapter 4 outlines the theoretical background and the parametric definitions for the constitutive FEA model used in this thesis. A parametric study is conducted to examine the effects that the constitutive parameters of dilation angle and the viscosity have on the load – deflection response of a concrete slab. The chapter then describes the implementation of the concrete compressive and tensile behavior into the model. This is preceded with a discussion on FEA modeling of the flexural reinforcement, the type of finite elements, boundary conditions, and load application. The chapter concludes with an investigation on convergence issues encountered in a FEA model with the discretization of the concrete slab into a finite element mesh and develops a methodology for achieving mesh size independency.

Chapter 5 discusses the development of the FEA model through calibration of the experimental results of previous researchers. The focus of this chapter to develop an expression for the tension stiffening parameters that accounts for varying the concrete compression strength,

varying the flexural reinforcement ratios, the inclusion of hooked steel fibers, and the yield strength of steel reinforcement.

The proposed FEA model is validated in Chapter 6. The model is used to simulate the punching shear behavior of nine slab specimens from the literature and compared with their experimental results.

Chapter 7 summarizes the findings of this thesis and presents recommendations for future research on this subject.

## Chapter 2

# Literature Review

### 2.1 Punching Shear Failure Mechanism

Punching shear failure occurs around a support where high shear stresses can develop. A punching failure is characterized by a wedge of concrete that punctures the slab above a column. The mechanism for punching shear failure initiates with a circumferential tensile crack on the top surface of the slab around the column perimeter. The crack develops first in regions of high shear stress adjacent to the corners of a column [1]. As the shear stress increases, more tensile cracks form around the column and propagate, under increasing load, to the line of contra-flexure in the slab. Recently, Muttoni [2] developed the Critical Shear Crack theory to describe how the opening of the shear cracks around a column increases with slab rotation as shown in Figure 2-1. He explains that as the cracks widen the concrete loses the ability to transfer shear across the crack interface by aggregate interlock. Flexural reinforcement in the slab begins to yield in the immediate vicinity of the column thus permitting larger rotations to occur about the slab-column interface. The shear cracks propagate through the slab and into the inclined concrete compressive strut, which is carrying the shear into the column. The loss of the compression strut from the intrusion of the shear crack eventually leads to the punching shear failure of the slab.

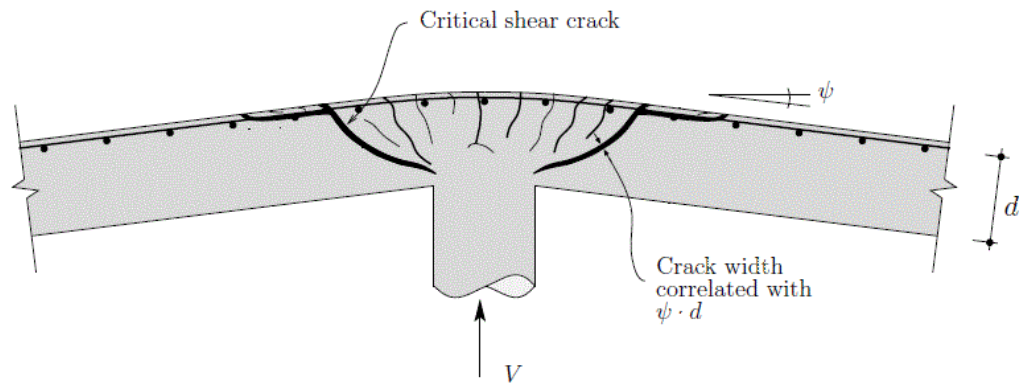


Figure 2-1: Critical shear crack [2].

## 2.2 Variables that Influence Punching Shear Resistance

Punching shear failure can be influenced through a number of variables in a concrete slab such as: concrete strength, flexural reinforcement ratio, column size, and the thickness of the slab. The state of the art reports by Regan [3] and CEB-FIB Model Code 2010 [4] provide a thorough analysis on the effect that each of these variables have on punching shear strength. A synopsis of the research into these variables will be discussed in this section. In addition, the effect of the yield strength of the flexural reinforcing steel will be discussed as another variable that effects the punching shear strength of reinforced concrete slabs. Finally, the review will examine how punching shear strength is enhanced through the use of steel fibers in the concrete mixture.

### 2.2.1 Concrete Strength

Early research by Moe [5] showed that the shear resistance of concrete is highly dependent on its tensile strength. The shear cracks that initiate punching shear failure develop when the tensile strength of the concrete is exceeded. The shear strength of concrete is generally

expressed as a function of its compressive strength  $f'_c$ . Since concrete compressive strength is proportional to its tensile strength, researchers typically express the shear strength as a function of compressive strength because it is more common to refer to concrete by its compressive strength. Graf [6] was one of the first to study the influence of the compressive strength on shear strength. From his research he determined that the relationship was not linear. Moe [5] followed up and proposed that the relationship could be approximated by the square root of  $f'_c$ . Marzouk & Hussein [7] showed that this relationship overestimated the effect of  $f'_c$  for high strength concrete which was later confirmed by Hallgren [8]. They found that the punching shear resistance correlated closer to the cubic root of  $f'_c$ . The North American codes ACI-318-14 [9] and CSA-A23.3-14 [10] use a square root expression and limit  $f'_c$  to 70 MPa. Some European design codes such as Eurocode2 (EC2) [11], CEB-FIP model code [4], and the British Standard (BS8110) [12] relate the shear strength to the cubic root of the concrete compressive strength.

### **2.2.2 Flexural Reinforcement Ratio**

The flexural reinforcement ratio,  $\rho$ , is the ratio of the cross-sectional area of the flexural reinforcement in the slab to the cross-sectional area of the concrete. Early investigations by Moe [5] and Elsnter & Hognestad [13] showed no increase in punching shear strength with higher flexural reinforcement ratios. Alexander & Simmonds [14] refuted this claim and asserted that the flexural reinforcement in Moe's [5] experiments did not contribute to the shear strength because it had experienced bond failure due to the closely spaced bars. Subsequent researchers have advocated that higher flexural reinforcement ratios do increase the slab shear strength [3] [7] [15]. Regan [3] showed that slab flexural reinforcement within a distance of three times the effective depth of the slab reinforcement,  $d$ , from the face of the column was effective in

increasing the shear strength. He concluded that slab reinforcement reduced the flexural cracking in the slab which increased the shear transfer due to aggregate interlock and also enhanced the shear transfer mechanism of dowel action. Marzouk & Hussein [7] also showed a significant increase of 63% when they increased  $\rho$  from 0.5% to 2.33%. Regan & Braestrup [16] and Sherif & Dilger [17] quantified the influence of the flexural reinforcement and suggested that the increase is proportional to the cubic root of  $\rho$ .

European codes, such as EC2 [11] and BS8110 [12], include the influence of the flexural reinforcement ratio on the shear strength of the slab. Both use a cube root expression for  $\rho$ .

$$\text{EC2:} \quad V_c = 0.18 \left[ 1 + \sqrt{\frac{200}{d}} \right] (100 \rho f_{ck})^{1/3} b_o d \quad (2-1)$$

$$\text{BS 8110:} \quad V_c = 0.79 \sqrt[4]{\frac{400}{d}} \left[ 100 \rho \frac{f_{cu}}{25} \right]^{1/3} b_o d \quad (2-2)$$

The North American codes differ significantly from the European standards on the use of flexural reinforcement on punching shear. The punching shear formulation in the American standard ACI 318-14 [9] does not account for the influence of the flexural reinforcement. Although the punching shear expression in the Canadian standard, CSA A23.3-14 [10], does not account directly for flexural reinforcement, it does require that a minimum amount of flexural reinforcement be concentrated in the immediate column region bounded by distance of 1.5 times the height of the slab from the column face. Tests by Yang et al [18], McHarg et al [19], and Lee et al [20] studied the effect of concentrating reinforcing bars over the column zone. They all

concluded that the use of the banded flexural reinforcement resulted in higher punching shear resistances than a uniform flexural reinforcing mat.

### 2.2.3 Column Size & Shape

The size and shape of a column has an influence on the shear stress distribution in the slab. Shear stress is inversely proportional to the critical shear perimeter and hence, the greater the column perimeter the lower the shear stress. ACI 318-14 [9] and CSA A23.3-14 [10] both use a distance of  $d/2$  to locate the critical shear periphery whereas BS8110 [12] use  $1.5d$  and EC2 [11] use  $2d$ . The shape of the column can induce shear stress concentrations at the corners. This effect is more pronounced in rectangular columns. Research by Hawkins & Criswell [1] showed that for ratios of long side to short side greater than two, the nominal shear strength decreases with increasing rectangularity.

### 2.2.4 Size Effect

The thickness of a slab has a pronounced effect on its punching shear strength. Similar to the critical shear perimeter, the thicker slab, reduces the shear stress throughout the section. Researchers such as Bazant & Cao [21] have shown that this reduction in shear stress is not linearly proportional to the thickness and, in fact, thicker slabs have smaller shear stresses at failure than shallower slabs. This phenomenon is known as the size effect. CSA A23.3-14 [10] and EC2 [11] recognize this effect and recommend a shear reduction factor for slabs thicker than 300 mm as:

CSA A23.3-14:

$$R_F = \frac{1300}{1000 + d} \quad (2-3)$$

EC2 2004:

$$R_F = 1 + \left(\frac{200}{d}\right)^{\frac{1}{2}} \quad (2-4)$$

The size effect is difficult to study experimentally because laboratories are usually limited to the size of the specimens that they can test and the loads that they can apply. Therefore, it is difficult and expensive to test full scale models. Many tests are performed on scaled models with reduced dimensions. However, care must be taken when using scaled test because the shear strength varies in a non-proportional manner. Finite element analysis can be used to eliminate this limitation when studying the capacity of thick slabs.

### **2.2.5 Flexural Reinforcement Yield Strength**

In addition to the flexural reinforcement ratio, the strength of the steel reinforcement also has an influence on punching shear behavior. Yang et al [18] found a 27% increase in punching shear strength when using reinforcement with a yield strength of approximately 800 MPa compared to conventional steel reinforcing with a yield strength of approximately 455 MPa when testing specimens of similar concrete strength and flexural reinforcement ratio. The increase was attributed to the fact that the higher strength bars did not yield prior to punching failure. As a result, the slab rotation is reduced which reduces the flexural cracks and increases the amount of aggregate interlocking.

### **2.2.6 Steel Fibers**

The tensile properties of concrete are greatly enhanced when small discrete steel fibers are added to the concrete mix. These steel fibers are randomly dispersed during the concrete mixing process and work to hold together the tensile cracks that initiate punching shear failure

until either the fiber yields or pulls-out of the concrete. The use of a steel fiber matrix in the concrete mix has the benefit of improving the post-cracking tensile characteristics, providing ductile compressive behavior, and enhancing the shear strength. Alexander and Simmonds [14] tested six slab specimens and demonstrated that adding steel fibers with a density of  $30 \text{ kg/m}^3$  to the mix increased the ultimate shear strength by 20% and improved the ductility of the connection. Harajli et al [22] also reported a significant increase in punching shear capacity; as high as 36% with steel fibers up to 2% by volume. Nguyen-Minh et al [23] found that the addition of steel fibers reduced the average crack width between 34 – 40% at the serviceability limit state. Their specimens experienced a 16% shear increase for a dosage rate of  $30 \text{ kg/m}^3$  up to 39% for a dosage rate of  $60 \text{ kg/m}^3$ .

The inclusion of the steel fibers does not have to be spread throughout the whole slab. Researchers have found improvements in punching shear with concentrating SFRC locally in areas of high shear stress [19] [20]. McHarg et al [19] showed significant improvements of 25% in punching shear strength with steel fibers concentrated around the column and an increase of 7% with the addition of fibers in the top concrete cover portion of the slab.

## **2.3 Concrete in Compression**

### **2.3.1 Behavior of Normal Concrete in Compression**

According to CSA A23.3-14 [10], the stress-strain curve exhibits an assumed linear behavior up to a stress level of around  $0.4 f'_c$ . Beyond a stress level of  $0.4 f'_c$ , micro cracks develop in the concrete and the behavior becomes highly non-linear. The curve ascends to an apex equal to the maximum compressive stress of the concrete and then descends until the strain

reaches the ultimate strain level assumed as 0.0035 as an average value. The stress – strain curve for concrete in compression is shown in Figure 2-2.

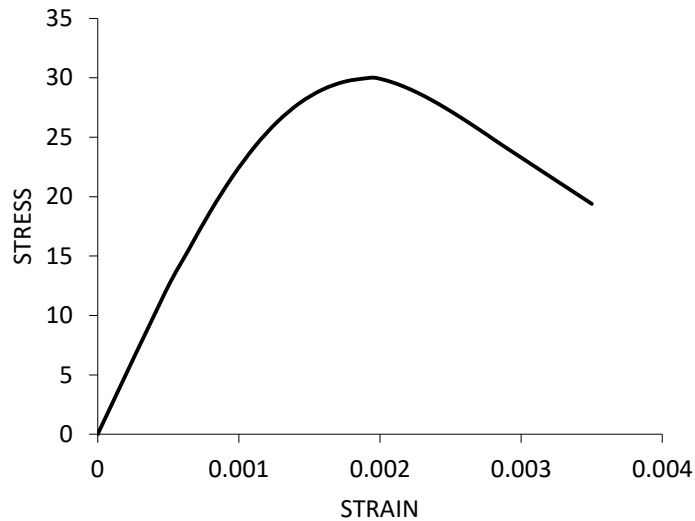


Figure 2-2: Stress – strain curve for concrete in compression.

Many analytical models have been developed to represent the stress-strain curve of concrete in compression. Table 2.1 presents two of the more widely used expressions to represent the compressive behavior of concrete.

Table 2.1: Models for the compressive behavior of concrete

| Researcher              | Compression Model   |
|-------------------------|---|
| Hognestad [24]          | $f_c = f_{c \max} \left[ \left( 2 \frac{\varepsilon}{\varepsilon_0} \right) - \left( \frac{\varepsilon}{\varepsilon_0} \right)^2 \right]$         |
| Collins & Mitchell [25] | $\frac{f_c}{f'_c} = \frac{n \left( \frac{\varepsilon_c}{\varepsilon_0} \right)}{n - 1 + \left( \frac{\varepsilon_c}{\varepsilon_0} \right)^{nk}}$ |

### 2.3.2 Behavior of SFRC in Compression

Experimental studies have been conducted to study the effect of fibers on all aspects of the compressive stress-strain curve: the linear-elastic branch, the point of cracking, the peak compressive load, the peak compressive strain, and the shape of the post-peak stress-strain curve. The literature on the effect of fiber volume on the peak compressive strength is inconclusive. Some studies show a slight increase in compressive strength with increasing fiber volume fraction [26] but others show a slight decrease in compressive strength with increasing fiber volume fraction [27]. A study published by Rizzuti & Bencardino [28] showed a slight increase in compressive strength (+2.25% to +4.35%) with low volume fiber fractions (1% to 1.6%) and a decrease (-1.35% to -7.5%) in higher volume fiber fractions (3% to 5%). Lee et al [29] showed that it was not necessarily the fiber volume fraction that affected the compressive strength but that the fiber aspect ratio had an influence too. They showed a correlation between the slump of SFRC and the compressive strength. For low slump SFRC concrete (caused by lower aspect ratios), the compressive strength was lower than those of high slump SFRC with higher aspect ratios.

Concrete in compression exhibits a volumetric expansion and ultimately fails due to tensile cracks in the unstressed direction. Ezeldin & Balaguru [26] postulated that the inclusion of steel fibers increase the compressive strength due to the transverse confinement of the steel fibers and this appears to be consistent with the work of Rizzuti & Bencardino [28] and Lee et al [29] for low fiber volume fractions. However, Hsu & Hsu [27] reported that SFRC do not contribute to concrete strength since more voids could be produced in the concrete matrix during mixing.

Although its effect on the peak compressive strength may be negligible, steel fibers have an influence on the post-peak response. It is a consensus from the literature that the maximum compressive strain of SFRC is higher than that of normal concrete and the post-peak softening branch of the compressive stress-strain curve is flatter. The addition of fibers enhances the descending branch of the compressive stress-strain curve. Due to the brittle nature of concrete, the descending (or softening) branch of the stress-strain curve ends shortly after the peak compressive stress. But for SFRC, the softening branch extends further and maintains a much smaller slope as the steel fibers enhance the deformability of the concrete in compression. This behavior provides a more ductile response and a higher ultimate strain [28]. The peak compressive strength is not significantly different as fiber volume is increased than that of the control specimen but the descending branch becomes noticeably flatter. Rizzuti & Bencardino [28] reported an increase of almost five-times in the ultimate strain of SFRC compared to that of normal concrete. Wang [30] found that the compression deformability did not improve for SFRC having volumetric fiber contents less than 0.5% and these specimens failed soon after reaching the peak compressive stress. Table 4.2 provides a summary of the models proposed for the stress-strain behavior of SFRC in compression.

Table 2.2: Models for the compressive behavior of SFRC

| Researcher                 | SFRC Compression Model  |
|----------------------------|---|
| Ezeldin & Balaguru<br>[26] | $f_c = f'_c \frac{\beta \left(\frac{\varepsilon}{\varepsilon_o}\right)}{\beta - 1 + \left(\frac{\varepsilon}{\varepsilon_o}\right)^\beta}$ <p>Where; <math>f'_c = f'_{cp} + 11.232RI</math>; <math>\beta = 1.093 + 0.2429RI^{-0.926}</math>;<br/> <math>\varepsilon_o = \varepsilon_{op} + 1427 \times 10^{-6}RI</math>; <math>E_c = E_{cp} + 9936RI</math></p> |

|                     |  |
|---------------------|--|
| Hsu & Hsu [27]      | $f_c = f'_c \frac{n\beta\left(\frac{\varepsilon}{\varepsilon_o}\right)}{\beta-1+\left(\frac{\varepsilon}{\varepsilon_o}\right)^{n\beta}} \quad \text{for } 0 \leq \varepsilon/\varepsilon_o \leq \varepsilon_d/\varepsilon_o$ $f_c = 0.6f'_c \exp\left[-0.7\left(\frac{\varepsilon}{\varepsilon_o} - \frac{\varepsilon_d}{\varepsilon_o}\right)^{0.8}\right] \quad \text{for } \varepsilon_d/\varepsilon_o \leq \varepsilon/\varepsilon_o$ <p>Where; <math>\varepsilon_d</math> is the strain at <math>0.6f'_c</math> in the descending branch</p> $\beta = \left(\frac{f'_c}{11.838(100V_f)^3 + 58.612}\right)^3 - 26V_f + 2.742$ <p><math>E = a_2f'_c + C_2</math> ; <math>\varepsilon_o = a_1f'_c + C_1</math>; where <math>a_1, a_2, C_1</math> &amp; <math>C_2</math> are constants</p> |
| Lee, Cho, & Oh [20] | $f_c = f'_c \left[ \frac{A\left(\frac{\varepsilon_c}{\varepsilon_o}\right)}{A-1+\left(\frac{\varepsilon_c}{\varepsilon_o}\right)^B} \right]$ <p>Where; For pre-peak: <math>A = B = \frac{1}{1-\left(\frac{f'_c}{\varepsilon_o E_c}\right)}</math> for <math>\varepsilon_c/\varepsilon_o \leq 1.0</math></p> <p>For post-peak: <math>B = \left(\frac{f'_c}{50}\right)^{0.064} \left[1 + 0.882\left(V_f \frac{l_f}{d_f}\right)^{-0.882}\right] \geq A</math></p> $A = 1 + 0.723\left(V_f \frac{l_f}{d_f}\right)^{-0.957} \quad \text{for } \frac{\varepsilon_c}{\varepsilon_o} > 1.0$ <p>Where; <math>\varepsilon_o = \left(0.0003V_f \frac{l_f}{d_f} + 0.0018\right) f'_c^{0.12}</math></p>   |

The expressions presented above have been developed for certain mixtures of SFRC that contain properties unique to that mix. Therefore, each expression presented in Table 2.2 has limitations and may not be applicable for all mix designs. For example, the expression by Ezeldin & Balaguru [26] was based on experiments with crimped steel fibers and may not be applicable for straight fibers or hooked-end fiber specimens and the Hsu & Hsu [27] model is only specific to fiber volume ratios up to 1%. The expression by Lee et al [29], was created for hooked-end fibers.

The elastic modulus of concrete is also influenced by SFRC. During the pre-peak response, Lee et al [29] found that the addition of steel fibers has little influence on the maximum compressive strength but did have an influence on the slope of the ascent of the stress-strain curve. The slope of the curve from initial stress to a limit of  $0.4 f'_c$  is assumed linear and is known as the Young's modulus of concrete. They presented the following equation for the elastic modulus of SFRC [29]:

$$E_c = \left( -367V_f \frac{l_f}{d_f} + 5520 \right) f_c^{0.41} \quad [\text{MPa}] \quad (2-5)$$

## 2.4 Concrete in Tension

### 2.4.1 Tension Softening of Normal Concrete

The uni-axial stress – strain behavior of concrete in tension initiates with a linear-elastic branch which ascends up to a point where cracking first starts to develop. Once cracking develops, a nonlinearity forms due to a reduction in stiffness. The concrete at a crack cannot transmit tensile stresses but the concrete between cracks is still capable of sustaining tensile forces due to the bond of the concrete matrix and aggregate friction interlock. As the tensile force increases, more cracks develop and less concrete is available to sustain tension. Under increasing tensile load, the concrete will continue to increase in stress up to its peak tensile stress,  $f'_t$ . The value of  $f'_t$  is generally accepted as  $0.33\sqrt{f'_c}$  [31]. Tensile stress above  $f'_t$  causes the cracking damage to become so high that any increase in deformation leads to a decreasing ability of the concrete to transfer stress [32]. This decline in tensile capacity is referred to as tension softening. During this softening process, the stress – strain curve in the post-peak

response descends until it reaches the ultimate tensile strain,  $\epsilon_u$ , where zero residual tensile strength exists.

Tension softening can be assessed experimentally, through direct tensile tests and modelled analytically based on the principles of fracture mechanics. The fracture mechanics approach can define concrete damage by evaluating the dissipated fracture energy required to generate micro cracks. The stress-deformation response of a concrete specimen subjected to tension cannot be expressed by an average stress-strain curve because the descending branch of a stress – strain curve does not represent the true behavior of the cracked portion. Rather, it is an idealization of the average material response. The first phase (i.e. ascending branch) of a specimen in tension can be described by a stress-strain diagram where the stress increases with deformation because the elongation during this un-cracked phase is the same along the whole specimen. As the specimen deforms into the post-peak stage, the stress starts to decrease with increased deformation. This occurs in areas where micro-cracks develop, known as fracture zones, where any increase in deformation leads to a decreasing ability to transfer stress. Once cracking is initiated, the un-cracked portion will experience elastic unloading and the cracked portion will exhibit strain softening. A generalized stress – strain curve for the full specimen cannot properly define the strain across the crack because the values vary depending on the location being measured. A stress – crack opening displacement curve is a more appropriate model than the stress – strain curve to characterize the crack behavior. Once the concrete is cracked, the definition of strain is not valid anymore.

The true stress – deformation response which represents the full elastic and inelastic range of a concrete specimen in tension can be achieved by the combination of two curves:

stress-strain curve ( $\sigma - \epsilon$ ) and stress versus crack opening displacement curve ( $\sigma - w$ ). The  $\sigma - \epsilon$  curve can be used to illustrate the stress relationship for strains at less than the peak point and the  $\sigma - w$  curve can be used to account for the localization of the induced cracks in the fracture zone [33].

The fracture mechanics approach to concrete was first introduced by Hillerborg [32] known as the Fictitious Crack Model. In this model, the fracture zone is represented by a simplified single crack with the hypothetical ability to transfer stress according to the  $\sigma - w$  curve (Figure 2-3).

An essential property of the  $\sigma - w$  curve is the area below the curve which is the measure of the energy per unit area required to generate a crack and is commonly known as the fracture energy,  $G_f$ . The fracture energy is thus a material property that can be obtained from experimentation. The accuracy of the simulation of the nonlinear behavior of concrete depends significantly on  $G_f$ .

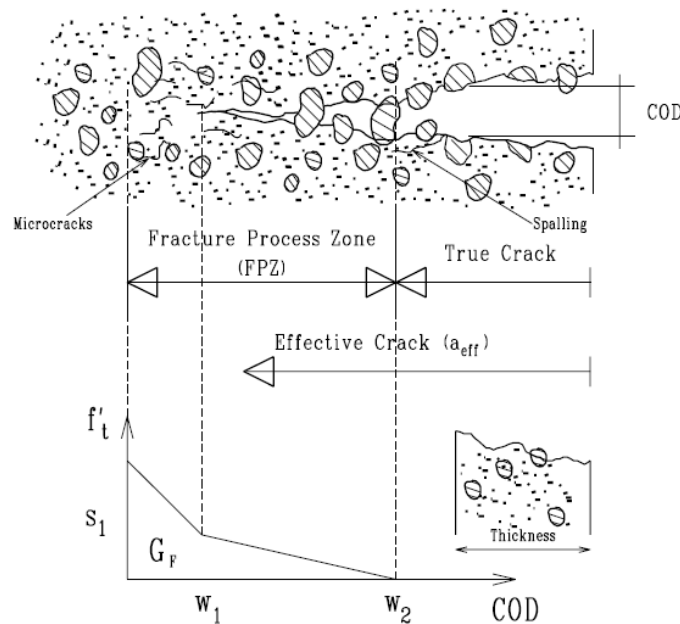


Figure 2-3: Hillerborg's Fictitious Crack Model [33].

The relationship between the stress-strain and the stress-displacement curve is defined by the characteristic length,  $\ell_c$ . From the stress-strain curve the characteristic length is equal to the ratio of the uniaxial tensile strength,  $f_t$  and modulus of elasticity. From the stress-displacement curve the characteristic length is equal to the ratio of the fracture energy  $G_f$  and  $f_t$ . Combining both expressions as a function of  $\ell_c$  yields the following expression:

$$\ell_c = E \frac{G_f}{f_t^2} \quad (2-6)$$

Bazant & Oh used fracture mechanics to develop their "Crack Band Model" to describe tension softening of concrete [34]. In their model, instead of considering the fracture zone as a single crack, they distributed the zone over a certain length equal to three times the aggregate size. The model was calibrated with available experimental data and yielded an empirical expression for fracture energy:

$$G_f = 0.0214 (f_t' + 127) f_t'^2 d_a / E_c \quad (2-7)$$

The CEB-FIB Model 1990 presented Equation (2-20) for calculating fracture energy. The 2010 version of CEB-FIB Model Code simplified this fracture energy equation to:

$$G_f = 73 f_{cm}^{0.18} \quad (2-8)$$

Whitman et al. [35] used the concept of fracture energy to create a bilinear strain softening diagram that can be easily implemented into a finite element analysis model. The diagram was defined by four parameters:  $f_t$ ,  $s_t$ ,  $w_1$ , and  $w_2$  as shown in Figure 2-4. These parameters were determined from experimentally obtained load-displacement diagrams by

means of a best fit where;  $w_1 = 0.75G_f / f_t'$ ,  $w_2 = 5G_f / f_t'$ , and  $s_1 = f_t' / 3$ . They also concluded that the fracture energy,  $G_f$ , of concrete is dependent on the un-cracked length of the specimen (i.e. ligament length), rate of loading, maximum aggregate size, and water-cement ratio.

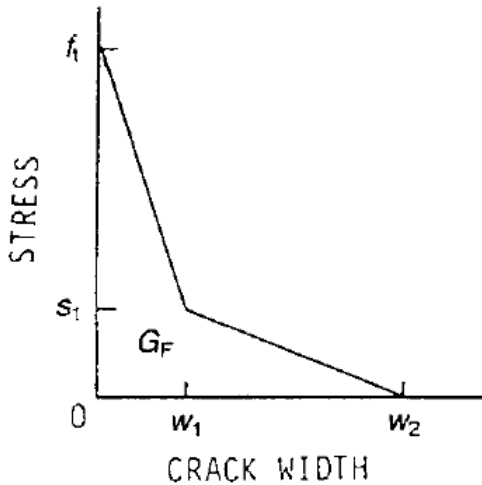


Figure 2-4: Bilinear stress – COD relation [35].

#### 2.4.2 Tension Softening of SFRC

The tensile properties of concrete are greatly enhanced when small discrete steel fibers are added to the concrete mix. These steel fibers are randomly dispersed during the concrete mixing process and work to hold the tensile cracks together until either the fiber yields or pulls-out of the concrete. The shapes of the stress – strain and stress – crack opening displacement curves for SFRC will differ from those for non-fibrous concrete due to the enhancement in post-cracking behavior. In SFRC, the bridging effect of the fibers provides an additional mechanism that significantly influences the transmission of tensile stresses across the cracks. This increase in tensile behavior significantly enhances the energy absorption and post cracking response of the concrete. As a result, the area under the  $\sigma - w$  curve will be much greater for SFRC than for plain concrete.

Barros & Cruz [36] evaluated the fracture energy of SFRC with three-point bending tests using displacement control. They tested a series of notched beams reinforced with 30, 60, and 90 kg/m<sup>3</sup> of hooked-end steel fibers. They found that the energy absorption capacity and fracture energy increased almost linearly with the fiber content. From their results they were able to assign fracture energy quantities to their SFRC specimens.

Teixeira et al [37] presented a numerical model for predicting the punching shear behavior of self-consolidating fiber reinforced concrete flat slabs. A part of their research included a parametric study on the influence of fracture energy on the deformational response of the slab. Their work yielded the following expression for the fracture energy of SFRC:

$$G_f^I = G_f(1.0 + 13.159W_f^{1.827}) \quad (2-9)$$

This equation was developed based on hook-ended steel fibers with an aspect ratio of 75 and with three distinct fiber ratios of 60, 75, and 90 kg/m<sup>3</sup>.

### **2.4.3 Tension Stiffening of Normal Reinforced Concrete**

Tension softening is a phenomenon unique to plain concrete. When reinforcement is present, the reinforcing bars intercept the tensile cracks and dominate the axial/flexural stiffness response of the member. The tensile stress is transmitted by the reinforcement and by a small portion of the un-cracked concrete between the cracks. This un-cracked concrete portion thus helps stiffen the element in what is known as tension – stiffening. Figure 2-5 shows a typical axial force versus average strain response of a reinforced concrete specimen superimposed on a plot with a bare steel bar. The ‘bare bar response’ is a plot of the behavior if tensile forces were only resisted by the steel bar and the contribution of the surrounding concrete was ignored. When

the concrete cracks at an axial tension just below  $N_2$  in the figure, the tension in the concrete is reduced and the load deformation response quickly approaches that of the bare bar. The maximum load is limited by the yield strength of the bar [38].

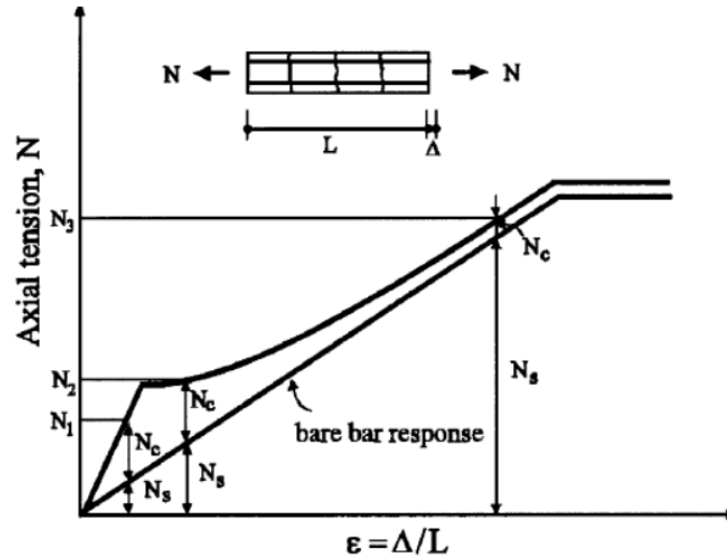


Figure 2-5: Tension stiffening curve for reinforced concrete [25].

The tension-stiffening stress-strain curve exhibits a much higher energy absorption response than the tension-softening curve due to the added rigidity of the steel bars. Figure 2-6 illustrates a typical comparison between the tension-stiffening and tension-softening diagrams highlighting the much more gradual decay of the tension-stiffening curve and the higher ultimate strains.

Numerous models have been proposed to describe the descending portion of the average stress-strain relationship (Figure 2-7). Scanlon & Murray [39] were the first to model tension stiffening in terms of a degraded concrete modulus. They proposed a model showing a linear behavior up to the tensile strength, followed by a series of discrete steps, each with a decreasing

modulus of elasticity. Lin & Scordelis [40] followed and fitted a polynomial expression to the falling branch of the stress-strain curve.

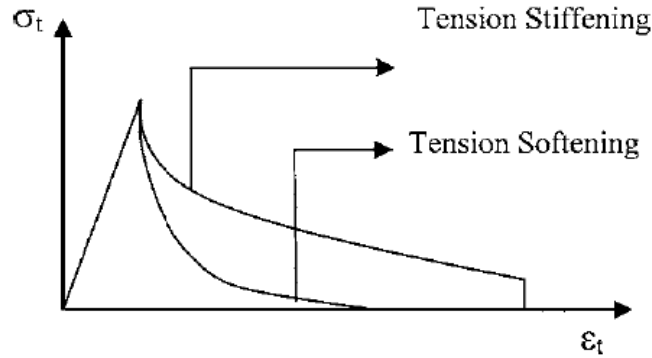


Figure 2-6: Tension softening and tension stiffening response [41].

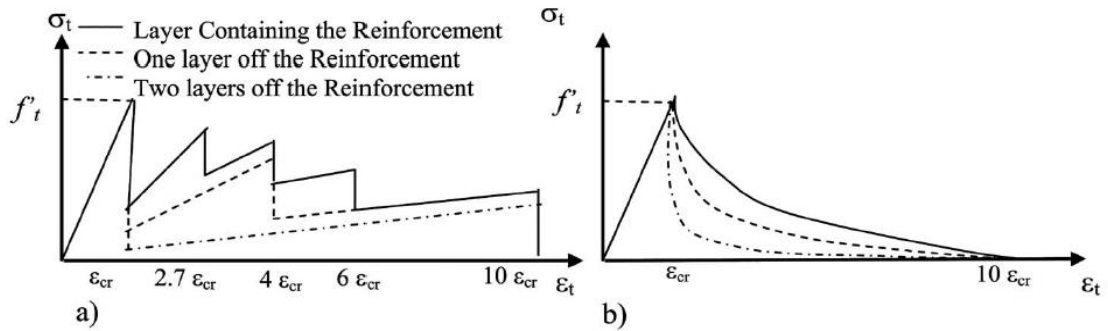


Figure 2-7: Tension stiffening models: a) Scanlon & Murray [39] b) Lin & Scordelis [40].

Several researchers used a bilinear model to predict the concrete stress-strain relation in tension (Figure 2-8). The parameters  $R_t$ ,  $P_t$ ,  $S_t$ , and  $F_t$  were inversely estimated from a combination of nonlinear analysis and experimental results on uni-axial specimens. Vebo & Ghali [42] reported a parameter set based on studies of reinforced concrete slabs. They proposed  $R_t = 0.45$ ,  $P_t = 0.9$ ,  $S_t = 2.2$ , and  $F_t = 12.2$ . Gilbert & Warner [43] presented a similar bi-linear model based on the difference of post-cracking response throughout the thickness of the reinforced concrete member. They presented a parameter set of  $R_t = 0.4$ ,  $P_t = 0.8$ ,  $S_t = 4$ , and  $F_t =$

10 for concrete adjacent to steel reinforcement and gave two other set of parameters for tensile “layers” located away from the steel reinforcing. This layered approach created a discontinuity in the global response because adjacent tension layers had the same strain but different tensile stresses. Nayal & Rasheed [41] refined the Gilbert & Warner [43] model to eliminate this discontinuity by replacing the layered stiffening parameters with a single set of stiffening parameters applicable to the entire tensile zone by calibrating their model to tests results. The best set of parameters that matched the experimental load-deflection curve was:  $R_t = 0.45$ ,  $P_t = 0.8$ ,  $S_t = 4$ , and  $F_t = 10$  (Figure 2-9).

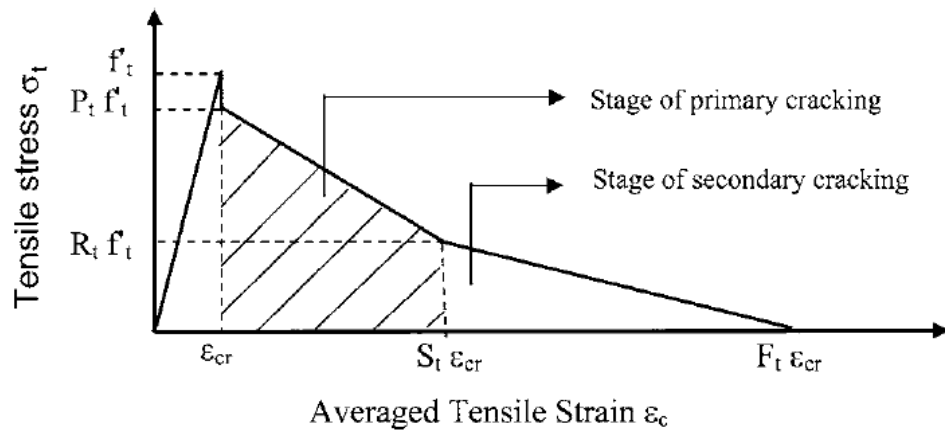


Figure 2-8: Tension stiffening model template [41].

Hsu & Mo [44] presented an exponential relationship to describe the descending branch of the tension stiffening curve.

$$\sigma_t = E_c \varepsilon_t \quad \text{if } \varepsilon_t \leq \varepsilon_{cr} \quad (2-10)$$

$$\sigma_t = f_{cm} \left( \frac{\varepsilon_{cr}}{\varepsilon_t} \right)^n \quad \text{if } \varepsilon_t > \varepsilon_{cr} \quad (2-11)$$

The rate of weakening,  $n$ , was given as 0.4 by Hsu & Mo [44]. Figure 2-10 shows the effect of varying the weakening function on the descending branch. As illustrated, increasing the weakening function decreases the descending branch of the curve. The ultimate tensile strain is defined by Hsu & Mo [44] as ten times the cracking strain.

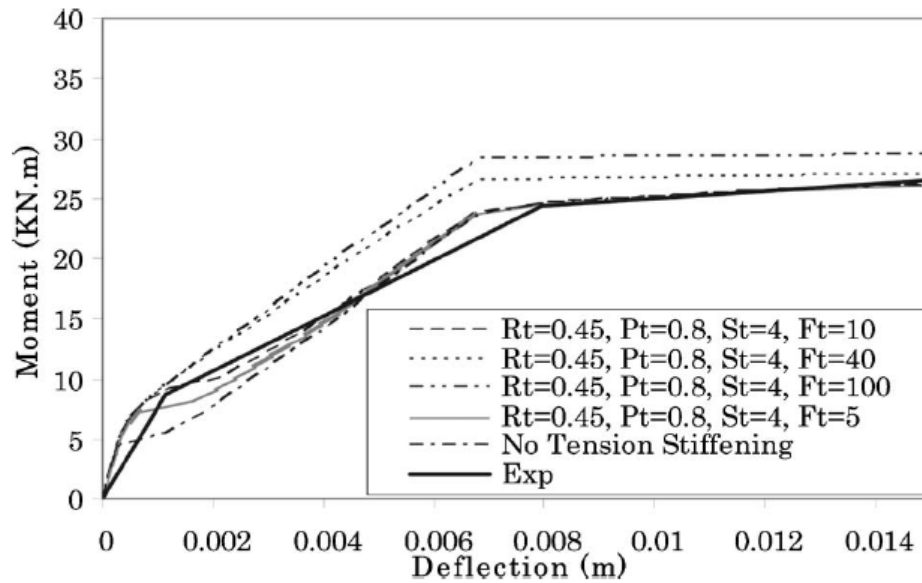


Figure 2-9: Nayal & Rasheed model calibration [41].

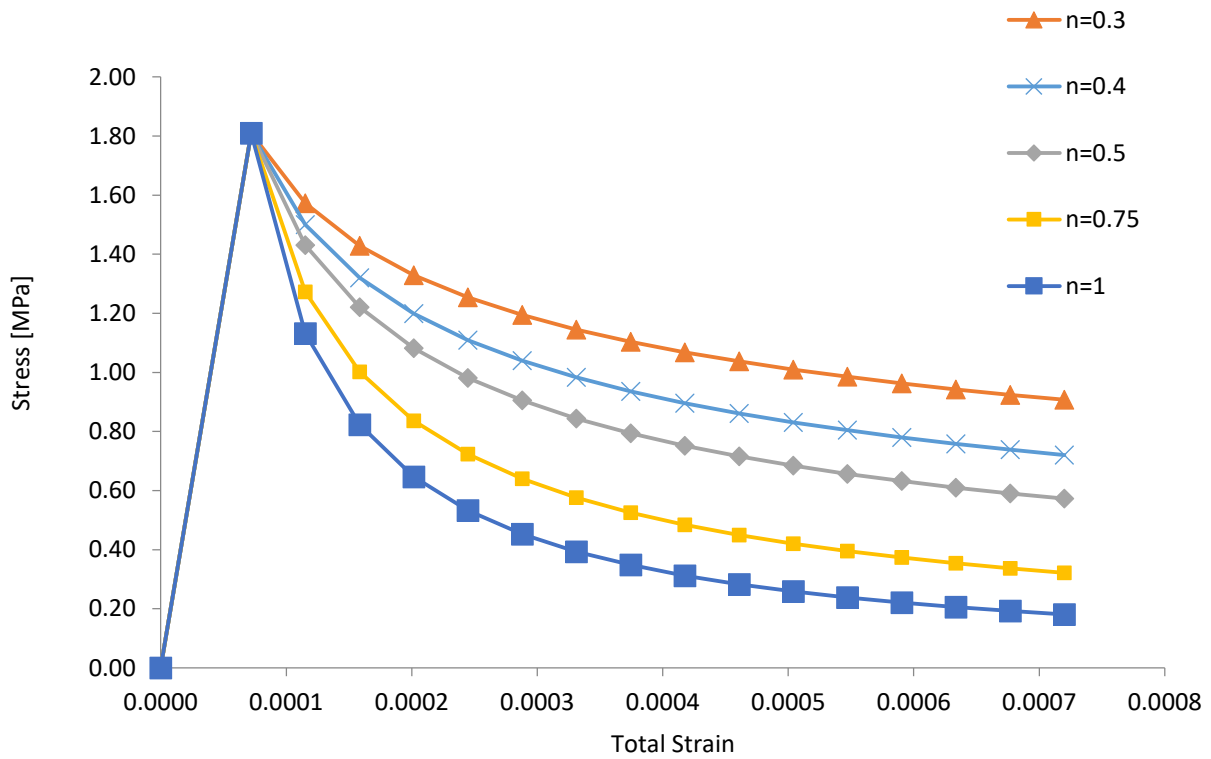


Figure 2-10: Hsu & Mo weakening function for tension stiffening [44].

#### 2.4.4 Tension Stiffening of Reinforced SFRC

The combination of tension stiffening and the post cracking residual tensile strength of steel fibers significantly affects the stress – strain tensile response of concrete (Figure 2-11). Steel fibers aid the bare steel bar and contribute to the axial stiffness of the specimen at the crack locations. Therefore, it is necessary to properly model the post-cracking resistance of SFRC for accurate predictions of the material’s performance.

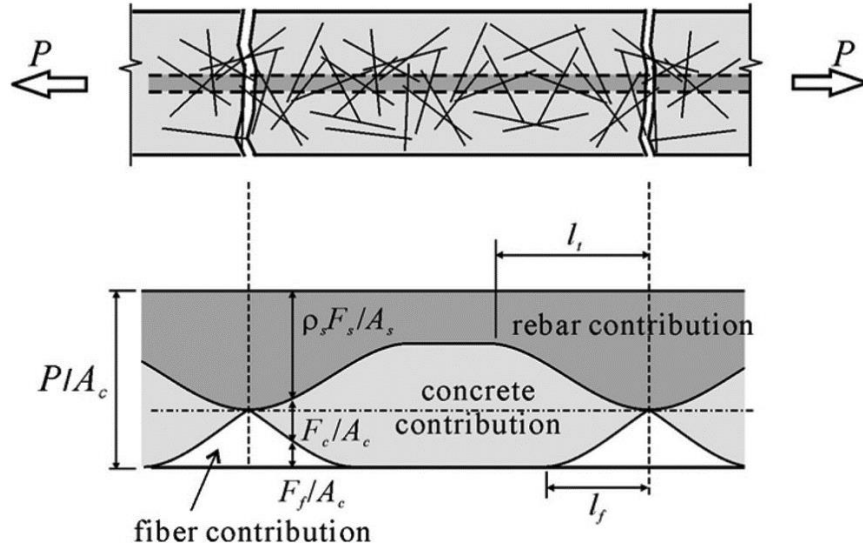


Figure 2-11: Distribution of stresses between cracks [31].

Abrishami & Mitchell [45] were among of the first to study the effect of steel fibers on tension stiffening through a series of uni-axial tensile tests. They concluded that the presence of steel fibers led to a significant increase in the tension stiffening of the reinforced concrete member. Figure 2-12 shows a sample test response from their experimental study. This figure illustrates that the SFRC specimen exhibited a greater tensile cracking load and greater tension stiffening after cracking than the reinforced concrete specimen without fibers. The authors concluded that SFRC displayed better tension stiffening due to the ability of the steel fibers to bridge across cracks and reduce the amount of tensile force transmitted directly into the steel bar. Hence, the tension stiffening effect of SFRC leads to a smaller decay in the stress carried by the concrete (Figure 2-13).

From their results, the authors derived an expression to predict the force at the crack in SFRC:

$$N_f = \frac{1}{6} V_f E_f A_c (\varepsilon - \varepsilon_y) \geq \frac{1}{6} V_f A_c f_{yf} \quad (2-12)$$

The authors acknowledge that this expression overestimated the point of first cracking (i.e. first point on the load – deflection curve of deviation from linearity) but correlated well with the concrete tensile stress-strain response of their experimental results.

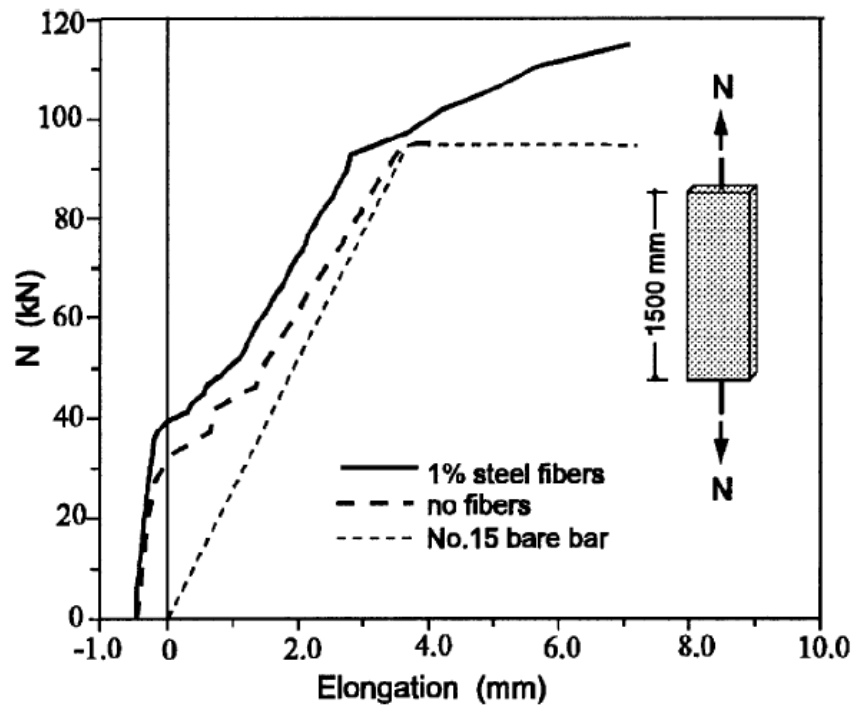


Figure 2-12: Abrishami & Mitchell tension stiffening results [45].

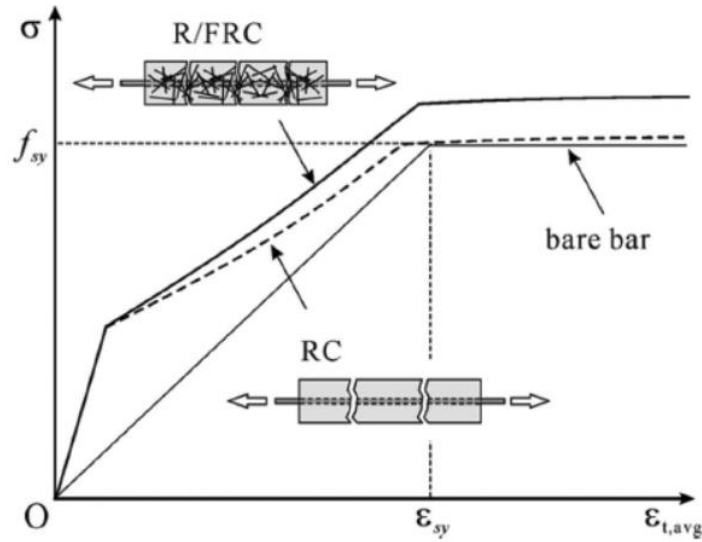


Figure 2-13: Tension stiffening of SFRC [31].

Tiberti et al [38] carried out a set of tension stiffening tests by varying the concrete strength, reinforcement ratio, fiber volume fraction, and fiber geometry. Their program consisted of fifty – nine uni-axial tensile tests on high strength concrete specimens (60 MPa to 95 MPa) and one hundred and nine normal strength concrete specimens. The authors generated a fairly comprehensive database of uni-axial tension tests of SFRC rectangular specimens reinforced with a central steel bar. The post cracking response of their SFRC specimens showed a noticeable enhancement in the post peak response. From their research they concluded that SFRC stiffens the post-cracking response of reinforced concrete members.

Lee et al [31] piloted a parametric study using a crack analysis procedure to derive a tension-stiffening model to reflect the effect of steel fibers on the tensile behavior that could be easily implemented into a finite element model. Their study considered the tensile behavior of steel fibers and the bond stress-slip relationship between the reinforcing bar and the concrete matrix to develop the following expression for tensile stress:

$$f_{c,TS} = \frac{f_{cr}}{1 + \sqrt{3.6c_f M \varepsilon_{t,avg}}} \quad (2-13)$$

where;  $M = \text{bond parameter} = \frac{A_c}{\sum d_b \pi}$

$c_f = \text{coefficient to consider steel fibers}$

$$= \text{for hooked fibers: } c_f = 0.6 + \frac{1}{0.034} \left( \frac{l_f}{d_f} \right) \frac{(100V_f)^{1.5}}{M^{0.8}}$$

$$= \text{for straight fibers: } c_f = 0.6 + \frac{1}{0.058} \left( \frac{l_f}{d_f} \right)^{0.9} \frac{(100V_f)}{M^{0.8}}$$

Naaman & Reinhart [46] plotted Figure 2-14 to illustrate the difference between the tension stiffening curves of SFRC and reinforced concrete without steel fibers.

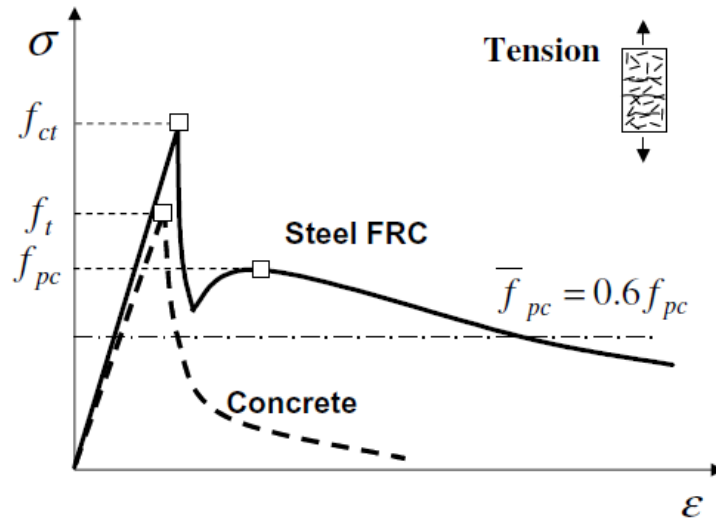


Figure 2-14: Tension stiffening model SFRC vs RC [46].

### 2.4.5 Peak Tensile Strength

The value of the peak tensile strength varies in the literature. The following are some typical expressions used for peak tensile strength:

- 1) Rankin [47] and MacGregor & Bartlett [48] recommended the value as the splitting tensile strength obtained from the equation:  $f_{sp} = 0.53\sqrt{f'_c}$  ;
- 2) Collins & Mitchell [25] recommend the value to be the uniaxial cracking strength:  $f'_{cr} = 0.33\sqrt{f'_c}$ . This is the value used to calibrate the tension stiffening curve by Hsu & Mo [44] as discussed earlier and the value used by Lee et al [31] for peak tensile strength;
- 3) EC2 [11] use the expression:  $f_{ctm} = 0.3 f_{ck}^{0.67}$

From a parametric study on the finite element analysis of flat slabs, Lim [49] concluded that the effect of peak tensile strength of concrete was insignificant on the ultimate punching shear load. He showed that by increasing  $f_t$  by 20% the ultimate load only increased by a corresponding 3% and by reducing  $f_t$  by 40% only reduced the ultimate load by 5%. He found that the tensile strength had more effect on the convergence of his finite element model. Too low of a tensile strength caused his model to diverge away from a solution. A closer examination of Lim's [49] results show that while the ultimate punching shear loads may be similar there is an obvious difference in the load deflection and ductility of the slab. Hence, the selection of the peak tensile strength can influence the punching shear behavior.

Naaman & Reinhart [46] showed, through a probabilistic analysis based on experimental results that the uniaxial tensile strength of SFRC is significantly affected by fiber volume ratio,  $V_f$ , and aspect ratio  $L/D$ . The parameters for their expression were developed for straight steel fibers. They defined the tensile strength of SFRC to be:

$$f_{ct} = f_t(1 - V_f) + \alpha_1\alpha_2\tau V_f(\ell_f / d_f) \quad (2-14)$$

Where;  $f_t = 0.292\sqrt{f'_c}$  (MPa);

In contrast to the work by Naaman & Reinhart [46], Bischoff [50] found that the use of steel fibers in the concrete mix does not appear to affect the response up to and including first cracking. Bischoff [50] concluded that the most influential contribution of steel fibers are in the enhancement of the ductility and post-cracking resistance of the slab. On the other hand, Abrishami & Mitchell [45] reported slight increases in cracking stress but only at fiber volume contents above 1%.

## **2.5 Literature Review of Punching Shear FEA**

Digital computing has revolutionized engineering research by enabling numerical calculations based on FEA to become a standard tool for the analysis of structures. FEA consists of a vast system of simultaneous algebraic equations that describe the behavior of a structure through a stiffness matrix. It works by subdividing the geometry of a continuum structure into simple components or “elements” that are interconnected at nodes and uses energy principles, such as the theorem of virtual work and the principle of minimum potential energy, to determine nodal displacements and nodal reactions. The resulting large amount of algebraic equations associated with FEA structural analysis made the method extremely cumbersome and impractical to use if it was not for the advent of digital computing.

In 1967, Ngo and Scordelis [51] were one of the first researchers to apply the technique of finite element analysis to study the behavior of reinforced concrete beams. Since that time finite element analysis has become a valuable tool for researchers to advance the understanding

of reinforced concrete crack formation and failure mechanisms. Due to computational limitations, early forms of FEA were performed with two-dimensional (2D) systems. The 2D structures can be simulated with a small number of degrees of freedom and thus require minimal computational effort. However, 2D elements are not sufficient to fully express the complex tri-axial stress state within the punching area. With advancements in digital computing it became possible to create more complex models using three-dimensional (3D) solid elements. Such elements offer high flexibility and accuracy in the discretization of reinforced concrete structures and generally lead to the most realistic analysis of punching shear [52].

The literature review in this section focuses on published research that involved the use of 3D solid elements to study the effect of punching shear on reinforced concrete slabs. The review concentrated on Abaqus computer software using the concrete damaged plasticity constitutive model. During the review particular attention is paid to the approach each author used for representing the tension stiffening behavior and for defining the CDP parameters used to solve plastic flow and yield functions. A thorough explanation the CDP model is provide in Chapter 4. A research paper using an alternate FEA program, Ansys, is provided at the end to show the differences, similarities, and capability of that program on modelling the punching shear behavior of reinforced concrete slabs.

### **2.5.1 Winkler & Stangenberg [53]**

Winkler and Stangenberg [53] demonstrated the effectiveness of the ‘concrete damaged plasticity’ model available in the finite element program Abaqus for modelling the punching shear failure of reinforced concrete slabs. They modelled a slab with an effective depth of 200

mm and a square plan dimension of 1450 mm concentrically loaded by a column stub. They used a stress-strain relation for uniaxial compression as:

*Ascending branch (where;  $\sigma_c \leq f_{cm}$ ):*

$$\sigma_c = \left( \frac{E_{ci} \left( \frac{\varepsilon_c}{f_{cm}} \right) - \left( \frac{\varepsilon_c}{\varepsilon_{c1}} \right)^2}{1 + \left( E_{ci} \left( \frac{\varepsilon_c}{f_{cm}} \right) - 2 \right) \left( \frac{\varepsilon_c}{\varepsilon_{c1}} \right)} \right) f_{cm} \quad (2-15)$$

*Descending branch (where;  $\sigma_c > f_{cm}$ ):*

$$\sigma_c = \left( \frac{2 + \gamma_c f_{cm} \varepsilon_{c1}}{2 f_{cm}} - \gamma_c \varepsilon_c + \frac{\gamma_c \varepsilon_c^2}{2 \varepsilon_{c1}} \right)^{-1} \quad (2-16)$$

The stress-strain relation used for uniaxial tension was derived from the following stress-crack opening relation:

$$\frac{\sigma_t(w)}{f_{ct}} = \left( 1 + \left( c_1 \left( \frac{w}{w_c} \right) \right)^3 \right) e^{-c_2 \left( \frac{w}{w_c} \right)} - \frac{w}{w_c} (1 + c_1^3) e^{-c_2} \quad (2-17)$$

The slab was modeled using 8-node solid continuum elements and the reinforcement was modelled as 2D truss elements. A perfect bond was assumed between the reinforcement and slab elements. The statics Riks method was used to solve the set of nonlinear equations and to address the issue of snap back. Parameters used to define the concrete damaged plasticity model included; dilation angle of 30°, shape factor of 0.667 and a stress ratio of 1.16. The results of the FEA analysis was compared with the experimental results. The FEA model showed a stiffer response in the elastic range and much more ductility in reaching the peak punching shear stress. It is noteworthy that the experimental deflection values were small and would have been very difficult to measure accurately during an experiment. The tension properties used for this slab are

only based on the uniaxial properties of plain concrete. The purpose of this model is to show that FEA is capable of replicating punching shear behavior. No attempt has been made to test how this model will perform by altering the material variables and as such this model does not provide the generality required to simulate a wide range of slabs with varying properties.

### 2.5.2 Youm et al [54]

Youm et al [54] created a nonlinear finite element model in conjunction with testing of five full scale slabs to analyze the failure mechanism of light weight aggregate concrete in punching shear. The concrete damaged plasticity model in Abaqus was used in the finite element simulation. The slabs were modeled as eight node solid elements and the reinforcement was modeled as 2D truss elements. The uniaxial tensile stress-strain behavior was assumed linear up to the point of cracking stress. The descending branch was modeled using the tension-stiffening exponential decaying expression by Hsu & Mo [44]:

$$f_c = f_{cr} \left( \frac{\varepsilon_{cr}}{\varepsilon_c} \right)^{0.4} \text{ when } \varepsilon_c \leq \varepsilon_{cr} \quad (2-18)$$

The exponential variable, given as 0.4 above, is known as the weakening function, n.

The cracking stress was given as:

$$f_{cr} = 1.23 \left( \frac{\text{Unit Density of LWAC} \left( \frac{kg}{m^3} \right)}{2200} \right)^{0.4} f_c^{0.2} \quad (2-19)$$

A main parameter for defining the concrete damaged plasticity model is the dilation angle. The authors compared the load-deflection results using dilation angles of 20°, 31°, and 45° (Figure 2-15). The dilation angle of 31° showed a near perfect correlation with the load

deflection response from the experimental observation. In general, all five slab specimens that were modeled showed a very strong correlation between the finite element model and the experimental results (Figure 2-16). The ascending branch followed a very similar line as the experimental data and then, at the point of punching shear, the FEA curve experienced a very sharp downward trend. The two experiments (N-GR-C slab and L-SH-C slab) shown in Figure 2-16 have concrete compressive strengths that varies from 34 MPa to 47 MPa and a flexural reinforcement ratio,  $\rho$ , which varies from 0.24% to 0.15%. In developing the tension-stiffening curve the author only describes selecting 0.4 for the weakening function (see Equation (2-18)), but neglected to disclose what effect of varying the weakening function would have on the load-deflection results. Even though the concrete strength and flexural reinforcement varied in the specimens, the weakening function remained constant. The constant value of the weakening function appears to suggest that it is independent of the value of  $f'_c$  and  $\rho$ . This assertion would be in contrast to the literature data which showed tension-stiffening increases with increases in  $f'_c$  and  $\rho$ .

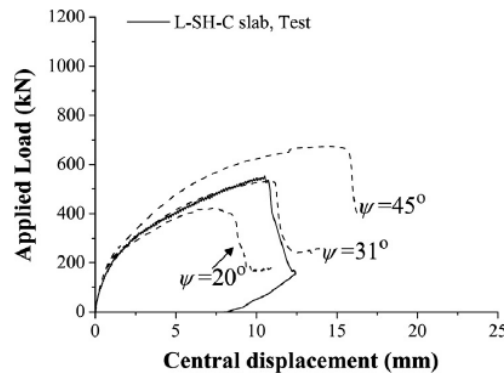


Figure 2-15: Parametric study of dilation angle [54].

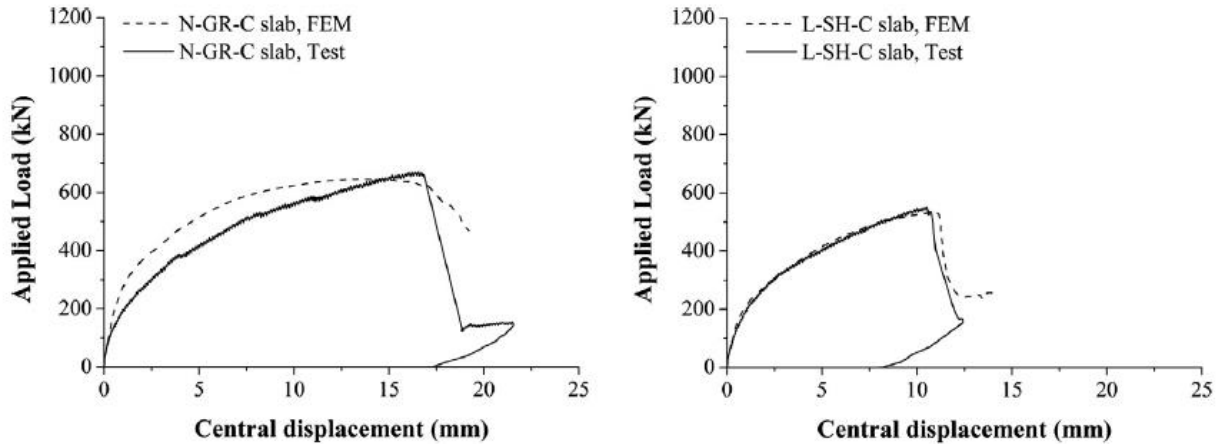


Figure 2-16: Youm load – displacement results [54].

### 2.5.3 Wosatko et al [55]

Wosatko et al [55] developed a numerical simulation for punching shear using the ABAQUS ‘concrete damaged plasticity’ model. The slab specimen that was simulated, denoted as SB1, was experimentally tested at the University of Waterloo (Figure 2-17). The overall dimensions were 1800 mm × 1800 mm × 120 mm and the slab was simply supported along a 1500 mm × 1500 mm square perimeter. The slab was loaded through a 150 mm × 150 mm centrally located column stub. The slab contained flexural and compressive reinforcement and had a concrete compressive strength of 44 MPa. The authors adopted a strain softening approach to model the tensile properties of the slab and assigned a fracture energy,  $G_f$ , of 106.5 N/m and a dilation angle,  $\psi$ , of 5°.

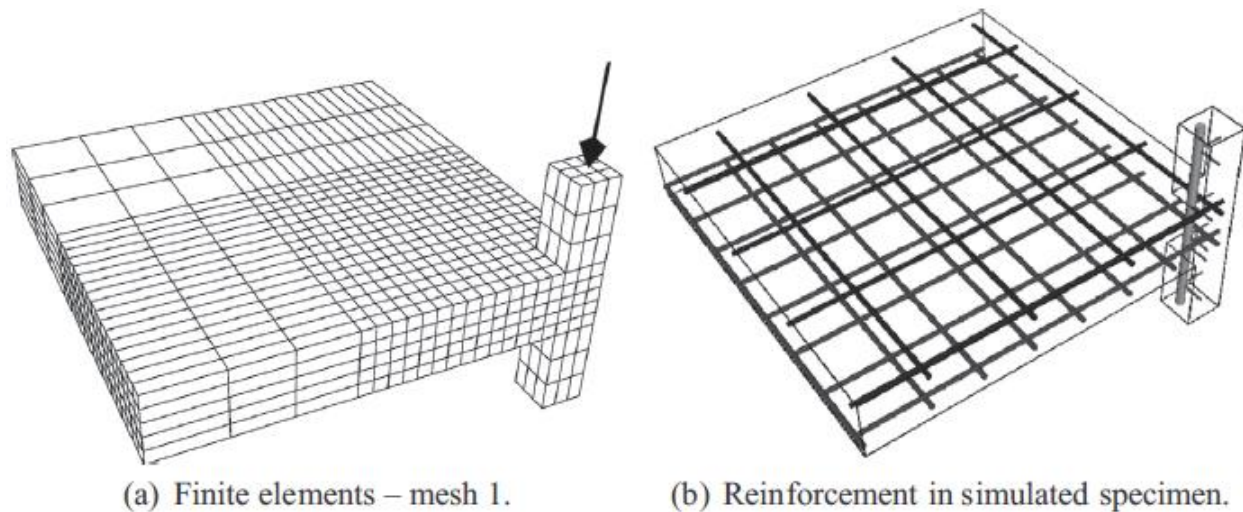


Figure 2-17: Wosatko finite element model [55].

The focus of their study was on the relationship between the finite element mesh size and the viscosity parameter,  $\mu$ . For a mesh size of 20 mm x 20 mm x 20 mm (mesh 1) the best predicted load-carrying capacity was obtained for using  $\mu$  equal to 0.01. However, for a finer mesh size of 12 mm x 12 mm x 12 mm (mesh 3) the results for  $\mu$  as 0.01 underestimated the load-deflection response. They concluded, from the strain contour diagram of the equivalent tensile plastic strain that mesh 3, with  $\mu$  as 0.002, seemed to represent the most realistic fracture mode. However, their load-deflection curve was still below the experimental result curve which suggests that these parameters still under-estimate the load-deflection response. The authors also found that when  $\mu$  equaled 1 the slab became too stiff and when  $\mu$  equaled 0 the solution resulted in localized deformation and premature failure. They concluded that the punching shear capacity grows with an increase in  $\mu$  thereby demonstrating that viscous regularization is a very important parameter when creating a finite element model. The authors did not offer a relationship correlating mesh size and viscosity with the load – displacement behavior.

#### 2.5.4 Genikomsou & Polak [56] [57] [58] [59]

In a series of published papers, Genikomsou and Polak expanded on the work by Wosatko et al [55] and modelled the same slab specimen (SB1) using the concrete damaged plasticity model in Abaqus but with different parameters. This literature review will focus on the evolution of their SB1 model in their four published papers [56] [57] [58] [59].

Genikomsou and Polak [56] presented a finite element model for the slab specimen SB1 with the damaged plasticity model parameters of: dilation angle of  $38^\circ$ , shape factor of 0.67, stress ratio of 1.16, and eccentricity of 0.1. A stress vs crack opening displacement approach was used to simulate the tensile response of the concrete. The fracture energy was calculated as 0.9 N/mm according to the CEB-FIB Model Code 1990 [60]. This model only specified tensile damage parameters. A static analysis approach was used in ABAQUS/Standard with a viscosity,  $\mu$  taken as 0.000085 and then compared to a quasi-static analysis with the dynamic procedure of ABAQUS/Explicit at a very slow rate of velocity. As shown in Figure 2-18, both analysis procedures compare well with the experimental results. The quasi-static analysis shows a noticeable downward trend which was interpreted by the authors as the point of punching shear failure. The static analysis does not show this same downward trend and thus it is not clear how the authors determined that punching shear had occurred and why the curve was cut-off at a deflection of 15 mm. The authors conducted a parametric study on the sensitivity of the viscosity parameter. Figure 2-19 shows the influence of the viscosity parameter on the load-deflection response. The graph shows that the higher the viscosity parameter the stiffer the load-deflection response. The authors also used the FEA model to show the influence that the flexural reinforcement ratio,  $\rho$ , had on the punching shear resistance (Figure 2-20). They successfully

showed that the higher the flexural reinforcement ratio the higher the punching shear resistance. However, they did not offer an analytical expression to quantify this relationship or how  $\rho$  will affect the tensile stiffening properties of their concrete tensile stress-strain model. Their approach for calculating the tensile stress strain values does not provide the capability to account for enhanced tension stiffening effect of increasing  $\rho$ . In their model, the authors ignored the tension-stiffening effect and just added more reinforcing bars to the model.

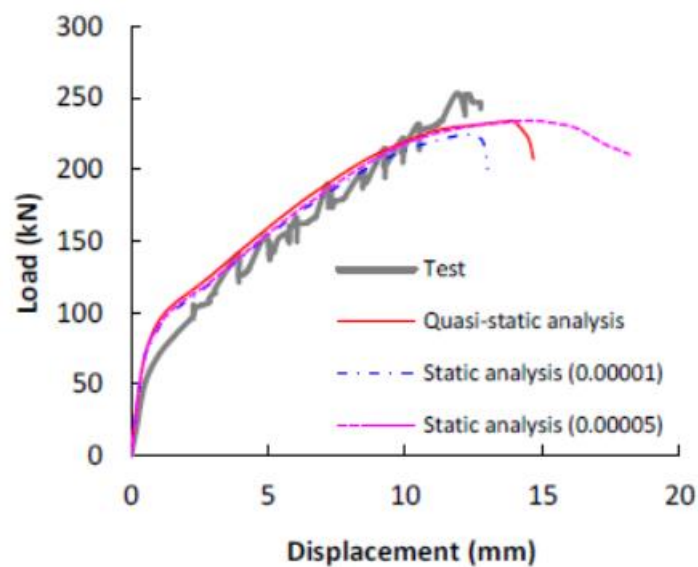


Figure 2-18: Load – deflection comparison of static vs quasi static [56].

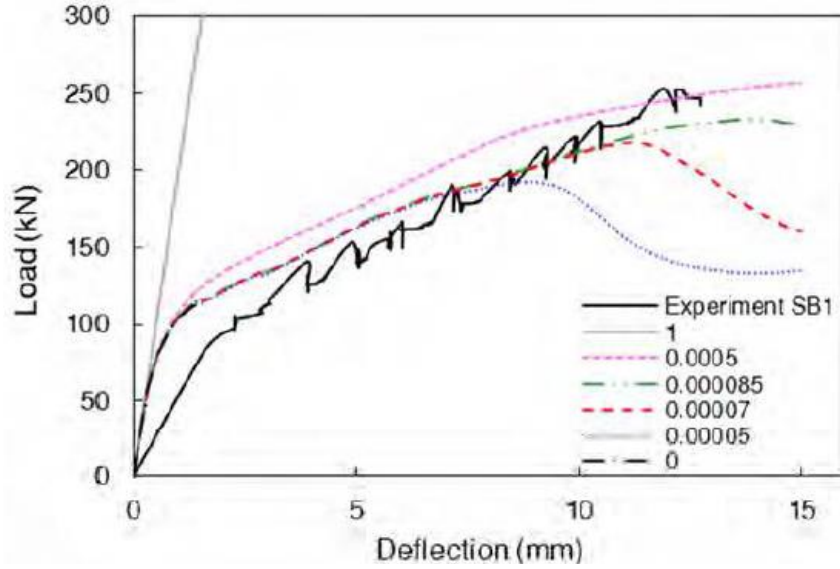


Figure 2-19: Influence of viscosity on load – deflection [56].

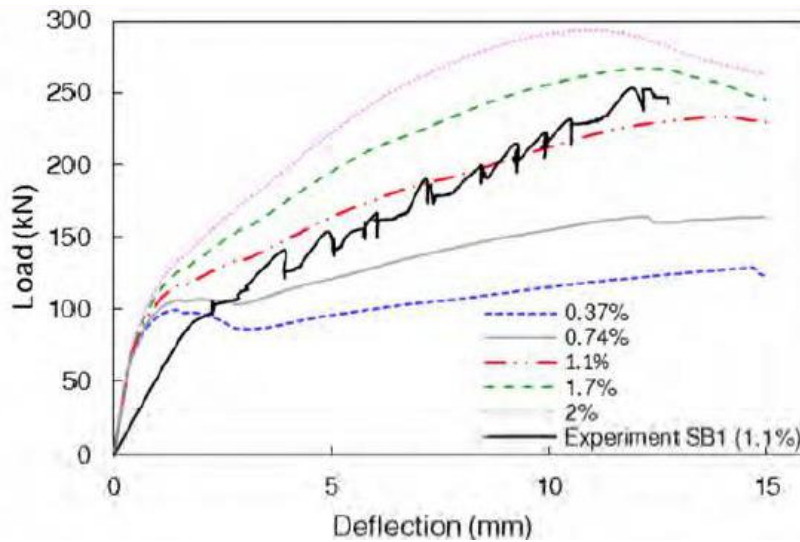


Figure 2-20: Influence of flexural reinforcement ratio [56].

Genikomsou & Polak [57] again modelled slab SB1 and included a model for an edge slab specimen and for an interior slab specimen with axial and horizontal loads. The damaged plasticity model parameters used the same values as their previous paper with the only exception that the dilation angle was increased from  $38^\circ$  to  $40^\circ$  with justification provided for the change.

The authors used the Hognestad parabola to define the uni-axial compression stress-strain relationship and represented the uni-axial tensile stress-strain relationship by a tensile stress vs crack opening displacement (COD) bilinear diagram (Figure 2-21). The peak tensile stress was taken as the uni-axial tensile stress:  $f_t = 0.33\sqrt{f'_c}$ . The fracture energy was obtained using the empirical formula in CEB-FIB Model Code 1990 as:

$$G_f = G_{fo} (f_{cm}/f_{cmo})^{0.7} \quad (2-20)$$

Where  $f_{cmo} = 10$  MPa,  $G_{fo} = 0.026$  N/mm, and  $f_{cm} = f_{ck} + 8$  MPa.

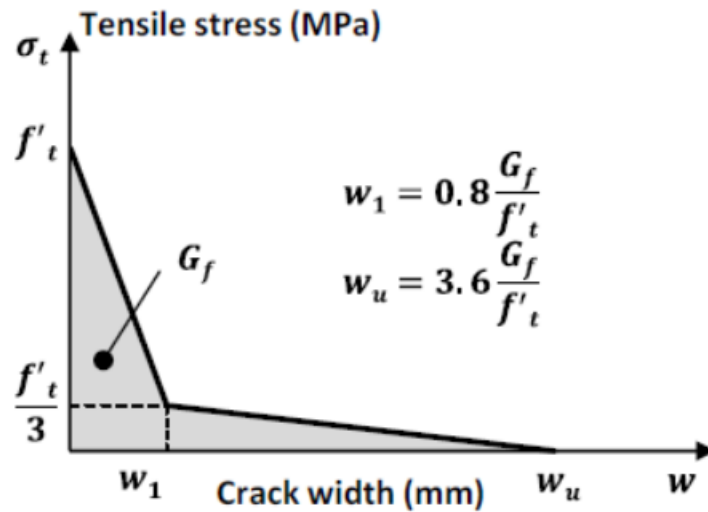


Figure 2-21: Stress vs crack opening displacement [57].

The authors converted the stress-COD curve into a stress-strain curve to minimize the localization of the fracture zone. The relationship between COD and strain is presented in Figure 2-22. The formula uses the characteristic length,  $l_c$ , which for 3D elements, can be defined as the cubic root of the elements volume.

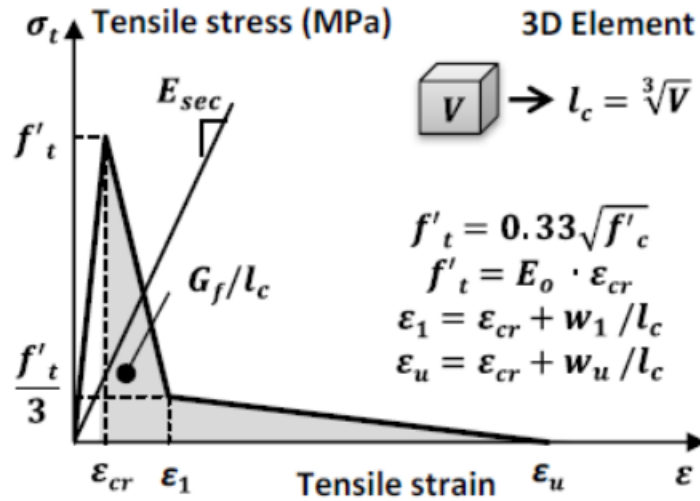


Figure 2-22: Bilinear strain softening diagram [57].

This paper provided several parametric studies. The following is a summary of their findings:

1. Dilation angle,  $\psi$  – an increase in dilation angle increased the punching shear resistance.
2. Shape factor,  $Kc$  – increasing  $Kc$  led to a very small but negligible decrease in load-deflection response at failure load.
3. Effect of Damage – if only tensile damage is considered, the results overestimate the failure load; when damage was applied to both tension and compression the model underestimated the failure load; it was noted that damage in compression, had a significant effect on the results but this was not included in their study. The authors concluded that for the described problem of punching shear, the definition of the damage parameters should not be taken into consideration even if the numerical results

underestimate the loading capacity. They stated that damage parameters are only important for cyclic and dynamic loading.

4. Mesh size – The authors show that the model is mesh size dependent. For mesh sizes greater than 20 mm, the solution cannot converge but instead gives a ductile and unrealistic behavior. Finer mesh sizes (less than 20 mm) and the solution converges prematurely giving a more brittle response.
5. Fracture Energy – an increase in fracture energy leads to stiffer load-displacement response. The authors calculated the fracture energy as 0.082 N/mm according to CEB-FIB 1990 which was slightly higher than the 0.1 N/mm value presented in their previous paper [56].

Genikomsou and Polak [58] used the same slab specimen SB1 to model a slab with shear bolts. The presentation of slab SB1 has some notable modifications from their previous papers. The concrete tensile relationship was again calculated using a fracture energy approach but this time they used an exponential softening curve:

$$\frac{\sigma}{f_t'} = f(w) - \left(\frac{w}{w_c}\right) f(w_c) \quad (2-21)$$

$$f(w) = \left(1 + \left(\frac{c_1 w}{w_c}\right)^3\right) \exp\left(-\left(\frac{c_2 w}{w_c}\right)\right) \quad (2-22)$$

The new softening curve is shown in Figure 2-23 superimposed with the bilinear strain softening diagram presented in their previous paper.

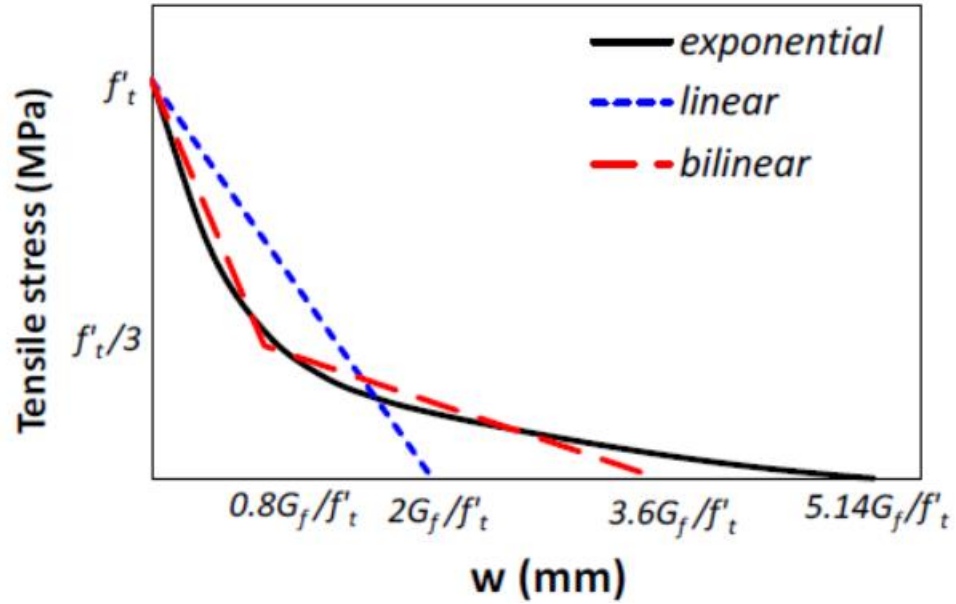


Figure 2-23: Strain-softening curves [58].

In the determination of the fracture energy, the authors found that the newer CEB-FIB Model code 2010 [4], increased the fracture energy from 0.082 N/mm (given in CEB-FIB 1990) to 0.148 N/mm. This increase in fracture energy led to a stiffer load–displacement response. Contrary to their recommendation in [57] regarding ignoring the damage parameters, the authors focus on the effect of the compressive damage on the load response. They conclude that the best results occur when the plastic strains equal 0.7 times the inelastic strains. The final load – displacement curve is presented in Figure 2-24.

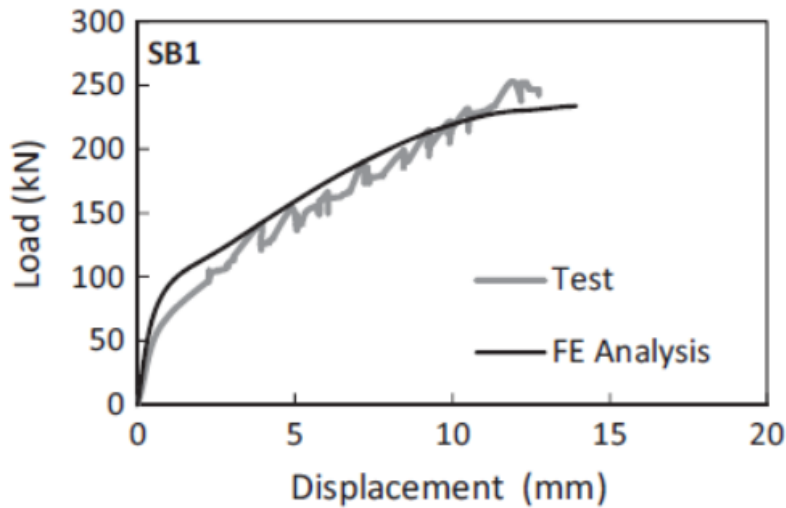


Figure 2-24: Genikomsou & Polak load – displacement curve [58].

Genikomsou and Polak [59] built upon their work in [58] and modeled three slabs with different shear bolt patterns. In this analysis, they used ABAQUS/Explicit and all the same parameters from [57] to model SB1. The model effectively showed the increase in punching shear capacity with the addition of the shear bolts.

The model development, findings, and conclusions presented in the four papers by Genikomsou & Polak were calibrated to one set of experimental data, slab specimen SB1. All of their analysis revolved around a specimen with constant parameters (i.e. concrete strength, tension stiffening, reinforcement ratio, etc.). No attempt was made to determine the applicability of the approach they used in modeling specimen SB1 would have on simulating other slab specimens with different parameters. Therefore, the generality of their model was not established since it was limited to only one experiment. It is not known how the punching shear model that they developed would behave when the factors that influence punching shear behavior are varied. Although the authors did perform numerous parametric studies, they did not establish any

expressions to aide a user in trying to model a slab with different properties (such as concrete strength, flexural reinforcement ratio, and reinforcement strength) than that of specimen SB1.

### **2.5.5 Nana et al [61]**

Nana et al [61] presented a numerical investigation using the concrete damaged plasticity model in Abaqus to model their experimental results on punching shear of concrete slabs. Their experimental program studied the influence of concrete strength and loading area on the punching behavior of slabs. They tested a series of nine slabs with varying geometries. Their FEA model was calibrated based on the experimental results of their specimens. The FEA model that they developed was used to further study the effects of slab depth, concrete aggregate size, flexural reinforcement, and the size of the loaded area. The tensile behavior of the slab was modeled using a fracture energy approach. Like Genikomsou & Polak, Nana et al [61] used the CEB-FIB Model code 1990 [60] & 2010 [4]. The only calibration that they performed was on the FEA numerical parameter of the dilation angle used in the constitutive model. The authors recommended to use a dilation angle of  $37^\circ$  to model concrete with a compressive strength of less than 25 MPa and found that the dilation angle would increase with an increase in concrete strength.

A comparison of the load-deflection response of the FEA model and experimental results showed good agreement with each other. A sample of their results is shown in Figure 2-25.

The author's represented the tensile behavior of the slab with a tensile-softening approach through the use of fracture energy even though the slab was reinforced. The fracture energy approach that they used to model the tensile behavior of the slab was effective for the slab

specimens that they tested with varying concrete strength and aggregate size. This is because the fracture energy approach is dependent on these two properties and they are direct variables in the fracture energy expression in the CEB-FIB Model Code [4] [60]. However, the fracture energy approach is not suitable to represent changes in the flexural reinforcement ratio. The fracture energy expression that the authors used does not contain an expression to alter the tension-stiffening properties of a slab with any changes in the flexural reinforcing ratio.

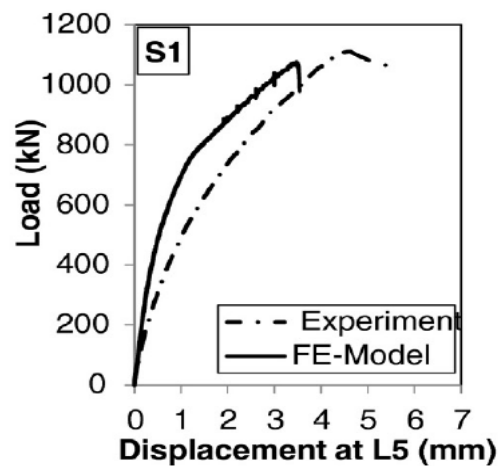


Figure 2-25: Nana FEA vs experimental results [61].

The authors did not achieve satisfactory results from their experimental tests on the influence of increasing  $\rho$ . Instead of seeing an increase in punching shear with an increase in  $\rho$ , the authors experienced a slight decrease. They acknowledged this discrepancy and attempted to use their FEA model to predict the ‘actual’ results. The authors did not have any reliable experimental results to calibrate their model to, so therefore they based their prediction solely on the output of a model calibrated for just compressive strength. The FEA model did show an increase with increasing  $\rho$ , however their FEA model is not capable of accounting for increased tension-stiffening due the higher concentration of reinforcing because there is no variable in the CEB approach that they used to represent concrete in tension to adjust for tension-stiffening. The

CEB approach only accounts for tension-softening which is a phenomenon unique to plain concrete. The slight increase in punching shear that they did experience in their model is contributed to the independent tensile strength of the 2D rebar elements and does not reflect any benefit to the shear resistance caused by tension-stiffening. It is anticipated, with the inclusion of tension-stiffening, that the authors should have experienced a much larger punching shear resistance with their increase in  $\rho$ .

The inability of the fracture energy method to adjust for flexural reinforcing is a major drawback to this approach when developing a robust model capable of representing all aspects of punching shear. The model developed in this thesis will be based on a stress-strain relationship similar to the approach used by Youm et al [54] which is more adaptable to account for more variables from the influencing parameters of punching shear.

### **2.5.6 Hawileh et al [62]**

Hawileh et al [62] developed a FEA model using the program ANSYS to study punching shear behavior. The authors compared their model with the high strength steel reinforcing test specimen data by Yang et al [18] which also included a specimen with SFRC. Their model used 3D solid elements to represent the concrete and steel reinforcement and implemented the tri-axial plastic concrete model available in ANSYS. The tension stiffening curve followed a bilinear trend. The ascending branch was assumed linear up to the point of the modulus of rupture. Then it dropped instantly by 60% of the tensile concrete strength and proceeded to decrease linearly to an ultimate tensile strain of six times the strain at the tensile rupture strength. The element used to model the reinforcing included a factor to simulate the bond-slip behavior between the reinforcing and the concrete. The authors used the CEB-FIP model [60] to calculate the bond

stress-slip. This expression could be adjusted for varying reinforcement ratios. They also accounted for the inclusion of steel fibers by introducing a tensile relaxation coefficient inherent in the ANSYS constitutive mode. For SFRC they set this value to 0.85. Punching shear failure was assumed to take place at the onset of yielding of the steel reinforcement followed by concrete crushing (taken at a strain of 0.003).

The results from Hawileh et al showed a very good agreement for the ultimate punching shear loads and the mid-span deflection between the FEA model and the experimental results. A sample of their results is presented in Figure 2-26. A main criticism of their research is in their results for slab specimen MB2. There was a premature failure of slab specimen MB2 in the lab caused by bond failure of the reinforcing and not caused from punching shear. The Hawileh et al model was used to simulate the punching shear behavior and would not have captured this bond failure. It would have been expected that their FEA model would have produced a much different load-deflection curve; one with a higher peak punching shear and displacement. However, their load-deflection results from their FEA model matched the experimental results for MB2 very closely. No mention of this discrepancy was made in their paper.

The authors' FEA model was too specific to the set of slabs included in their study. Their approach did show some generality that could lend itself to modelling other slabs, however, no other slab specimens were tested to analysis the robustness of their model. The purpose of this thesis is to develop a finite element model that will predict, with reasonable accuracy, the ultimate load and load-deflection curve for a wide range of concrete slabs with a number of varying parameters that influence punching shear strength.

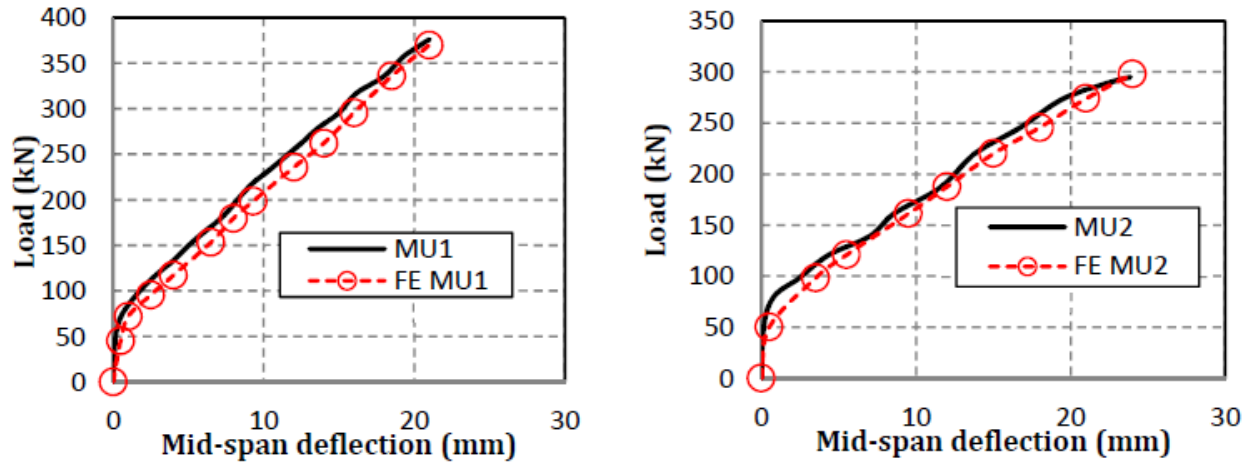


Figure 2-26: Hawileh FEA vs experimental results [62].

### 2.5.7 Summary

A commonality of the available research presented above is that no model presented a unified approach to modelling punching shear with varying material properties. Each model was created specific to the experimental slab specimen that it was simulating. The creation of the models did not provide the generality required to simulate a wide range of slabs with varying properties. None of the authors established any expressions to model variations in the variables that influence punching shear such as: concrete strength, flexural reinforcement ratio, and reinforcement strength.

## Chapter 3

### Data Used in the Current Study

Reinforced concrete is a complicated material to model due to its nonlinearity in both compression and tension stress-strain behavior. In order to represent the behavior accurately, finite element models must be calibrated based on the observations of physical models available from experiments. Finite element simulations require that the punching shear failure mechanism be reproduced properly and include accurate predictions of tension softening and tension stiffening behavior. To create models, the stress-strain relationship of the concrete material model must be calibrated with experimental data. The models should predict the actual behavior, such as the load-deflection output of the experimental results.

The phenomenon of punching shear has received a lot of attention from researchers from the early decades of the twentieth century and still on-going today. Consequently, the experimental database is vast but it does not always provide a consistency of results across a range of researchers. Therefore, to develop a robust FEA model capable of predicting punching shear, this thesis will focus on test data from a research program from McGill University that features slab specimens that were physically modeled to include all of the punching shear parameters under consideration in this thesis. The experimental results from this research program forms the basis of the model developed in this thesis. The research program consisted of three published papers that built upon each other. The test set-up and slab specimens were similar in the three papers but each paper investigated the influence of different parameters on punching shear strength. McHarg et al [19] studied the effect of flexural reinforcement ratio in the column vicinity as well as the concentration of SFRC around the column and a layer of

SFRC in the top slab cover. Lee et al [20] overlapped McHarg et al [19] by also studying the influence of the flexural reinforcement ratio but they included testing the effect of varying the concrete strength as well as using high strength SFRC within a distance of  $2d$  from the column face. Yang et al [18] focused their punching shear study on the effect of high strength flexural reinforcing in combination with SFRC and a varying flexural reinforcing ratio.

Not all of the experimental data available in these three papers will be used to create the FEA model. The slab specimens that are not used in the development will be used in the verification process. Once the model is established it will be used to simulate the load – deflection results of the other available slab test data. This verification process is necessary to establish that the model can represent punching shear behavior on slab specimens outside of the ones used for calibration. To further validate the effectiveness of the model, it will also be used to simulate the experimental punching shear behavior of two other researcher programs in the literature conducted by Genikmosou & Polak [56] and Pourezza [63]. The work by Genikmosou & Polak [56] was reviewed extensively in Chapter 2 and will not be reiterated here. A summary of Pourezza's [63] research on the punching shear strength of SFRC slabs will be provided in this section.

The preceding sections will describe the test data from the research that will be used in this thesis to calibrate and validate the FEA punching shear model.

### **3.1 McHarg et al [19]**

McHarg et al. [19] conducted an experimental program to investigate the strategic use of SFRC on punching shear capacity by concentrating SFRC just around the slab-column joint and

only in the top slab cover. They tested six slab-column specimens of 2300 mm square, 150 mm thick, with a 225 mm square column stub. The first slab series (N-series) was normal 30 MPa concrete, the second slab series (FS-series) was 30 MPa SFRC (0.5% steel fibers) placed at 500 mm around the column, and the third slab series (FC-series) was 30 MPa SFRC (0.5% steel fibers) used at the top slab cover (40 mm). The slab specimens are illustrated in Figure 3-1. Each series consisted of two slab specimens; one with uniformly distributed top reinforcement and the other with banded top reinforcement. The concentrated SFRC showed significant improvement in punching shear strength (25% increase), enhanced ductility, and reduced crack widths. The addition of fibers to the concrete cover slightly increased the load-carrying capacity up to 7%. The test also studied the effect of concentrating reinforcing bars over the column zone to which they concluded that the use of the banded top reinforcement resulted in higher punching shear resistances. The authors concluded that the ultimate strength of the slab was influenced more by the addition of the fibers than by the distribution of the reinforcing steel. Figure 3-2 shows the load-deflection results of the slab specimens.

| Distribution of Flexural Reinforcement |             |            |
|--|-------------|------------|
|  | Uniform (U) | Banded (B) |
| N Series                               | <p>NU</p>   | <p>NB</p>  |
| FS Series                              | <p>FSU</p>  | <p>FSB</p> |
| FC Series                              | <p>FCU</p>  | <p>FCB</p> |

Figure 3-1: McHarg slab specimens [19].

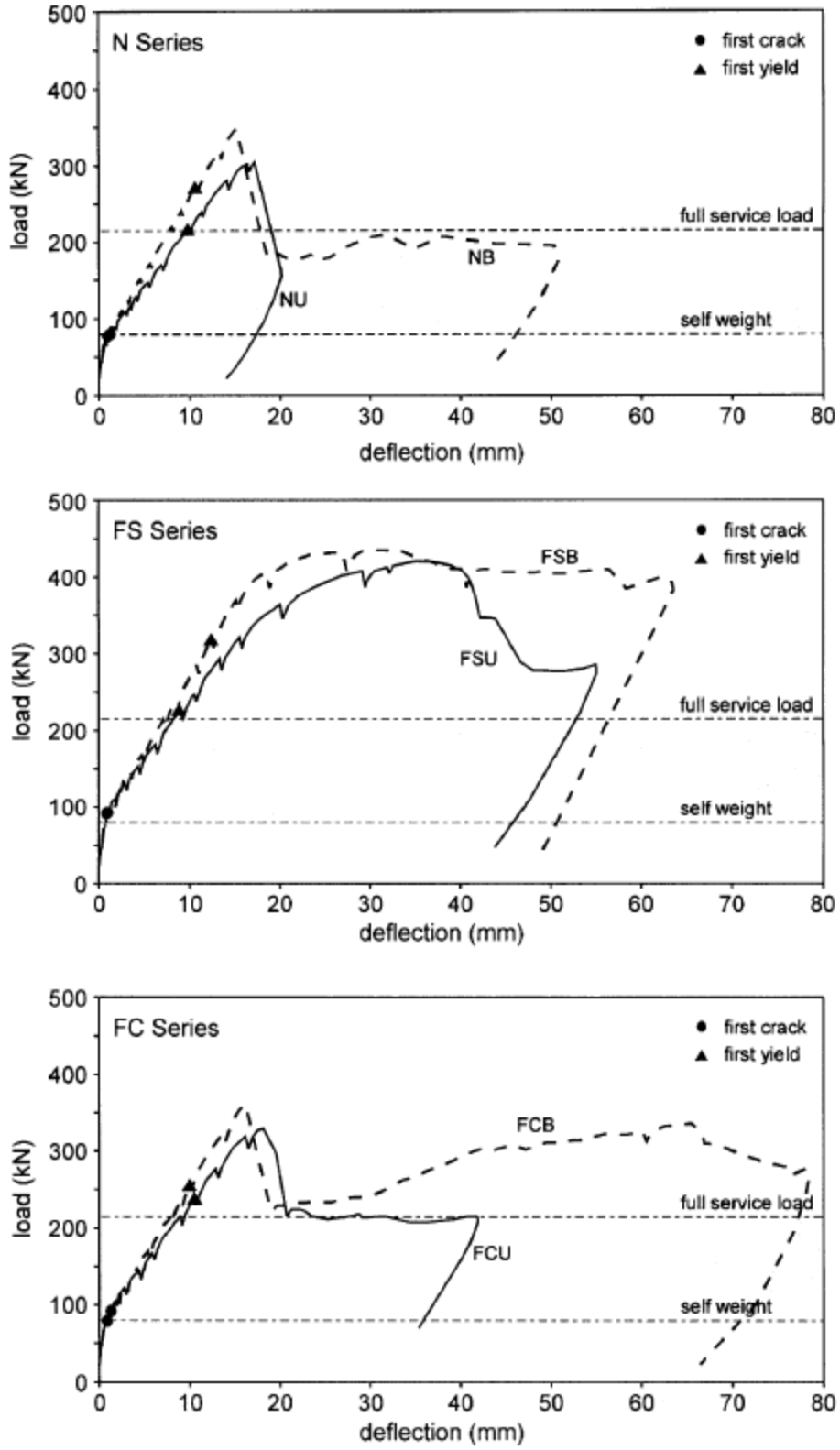


Figure 3-2: McHarg load deflection results [19].

### 3.2 Lee et al [20]

Lee et al [20] followed up on the work of McHarg et al [19] by also testing the influence of concentrated SFRC around the column with banded and uniform reinforcing. They tested eleven slab-column specimens of similar geometry to McHarg et al (Figure 3-3). In contrast to McHarg et al, who used the same concrete strength throughout their experiment, Lee et al tested eight specimens with varying concrete strength to study the effect of banded reinforcement versus uniform reinforcement. They cast two specimens with concentrated 40 MPa concrete mixed with 0.5% steel fibers 500 mm around the column with a uniform and banded top reinforcing layout. They also cast two specimens with 90 MPa SFRC at a distance of  $2d$  from the column face. Like the work by McHarg et al [19], they found that concentrating the SFRC around the column for a distance of 500 mm lead to an increase in punching shear strength and lower crack widths. The failure mode behaved much more ductile than the sudden punching experienced with non-fiber reinforced slabs. The authors found that the addition of fibers increased the shear failure perimeter to a region just outside the concentrated fiber zone. When using puddled high strength SFRC at a distance of 180 mm ( $2d$ ), the authors reported that there was a significant improvement in the punching shear performance although the specimen did not appear to exhibit the same amount of ductility as that with the wider puddled SFRC (Figure 3-4).

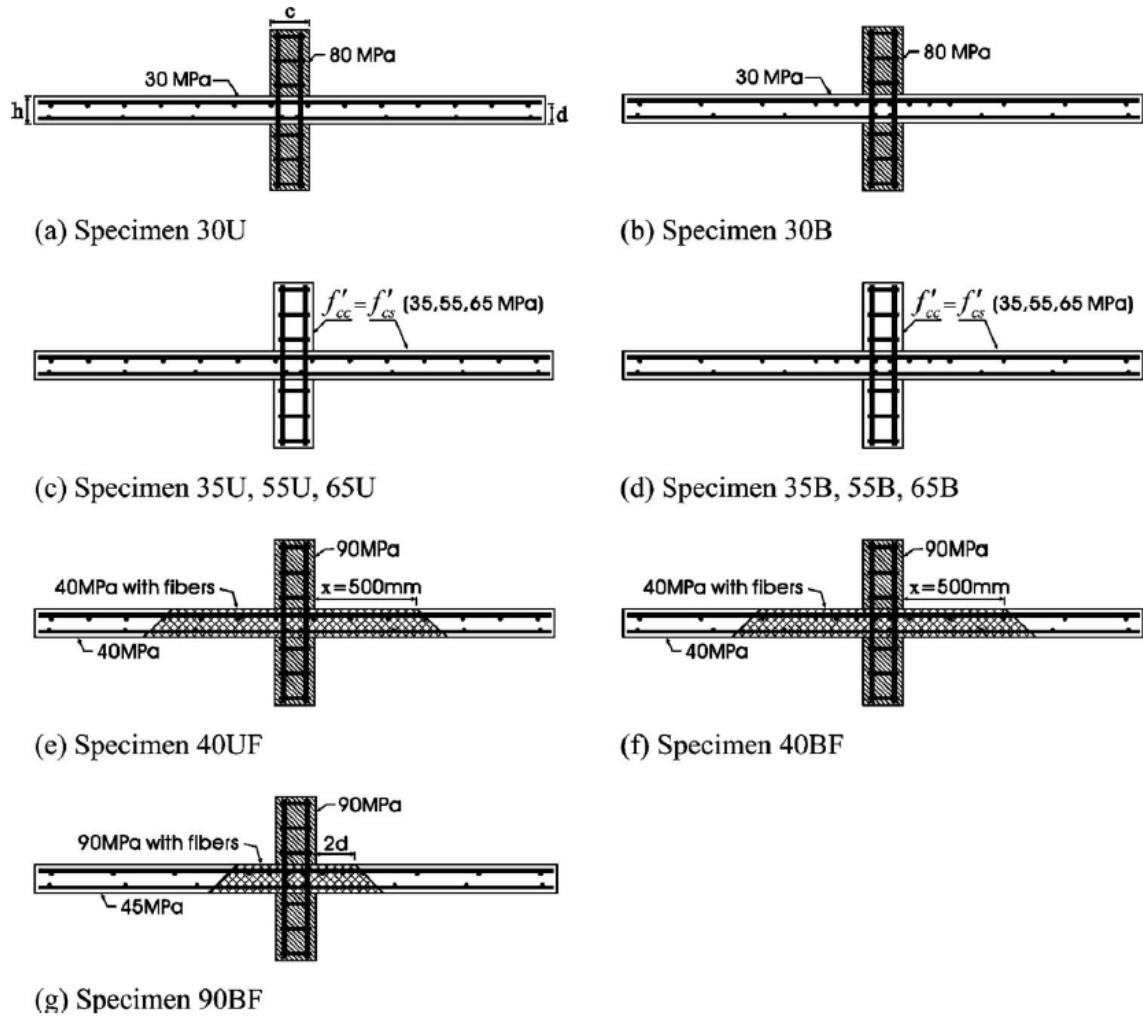


Figure 3-3: Lee slab specimens [20].

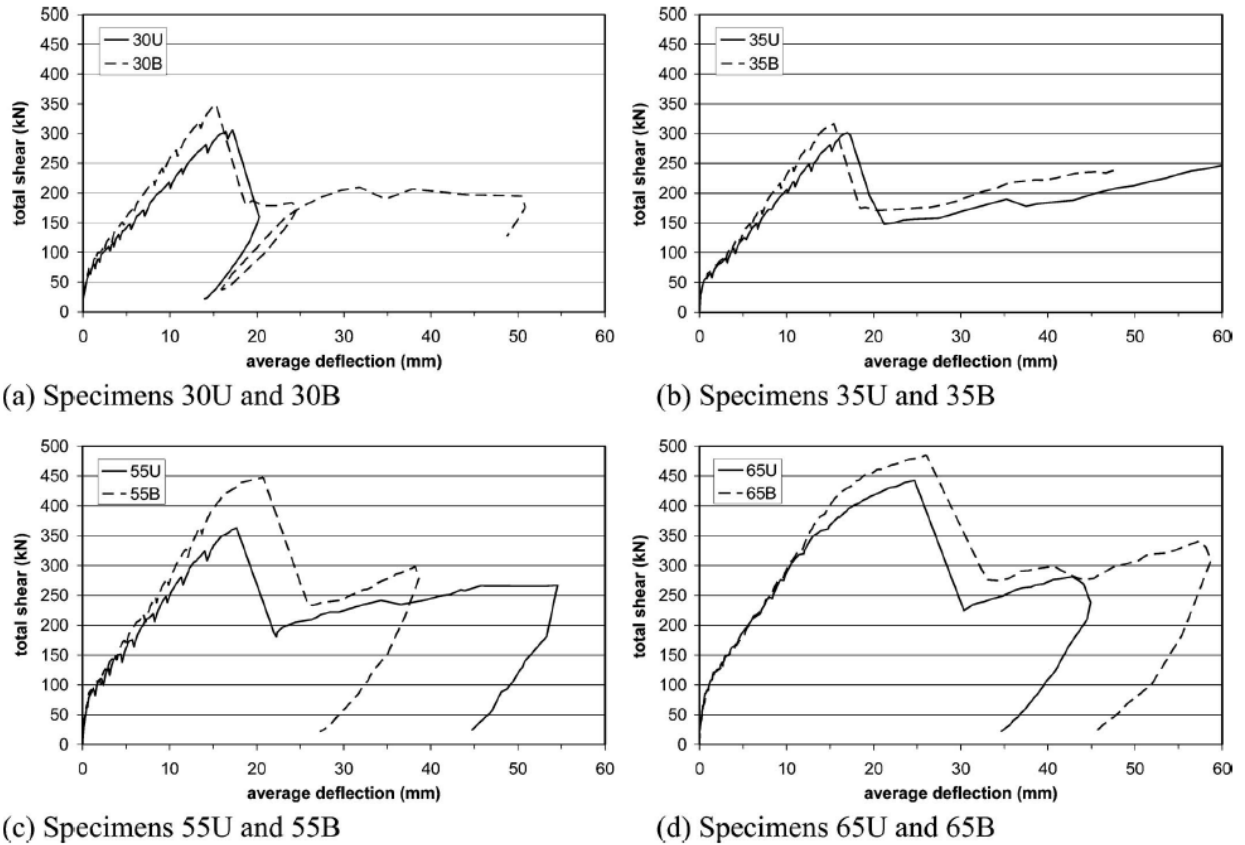


Figure 3-4: Lee load – deflection results [20].

### 3.3 Yang et al [18]

Yang et al [18] used the same experimental set-up as Lee et al [20] and McHarg et al [19]. The focus of their study was on the punching shear behavior of slabs reinforced with high-strength flexural reinforcement. They also studied the effect of concentrating the flexural reinforcement in the column vicinity and using SFRC on punching shear. Yang et al [18] used the same control slab specimens as McHarg et al [19] (NU & NB) as a reference for punching shear behavior with uniformly distributed conventional steel bars (NU denoted S1-U in their report) and with banded conventional steel bars (NB denoted S1-B in their report). They then introduced specimen MU1 and MB1 which had the same reinforcement layout as S1-U and S1-

B, respectively, but used high strength bars (ASTM A1035). Specimen MU2 was reinforced with high strength bars with an amount of flexural reinforcement such that the slab had the same flexural strength as specimen S1-U. To test the combined effect of high strength steel and SFRC, Yang et al [18] tested MBF2 which was similar in reinforcement to MB2 but featured SFRC in the slab within the immediate column region. The slab specimens are summarized in Figure 3-5. From their test results (Figure 3-6), Yang et al [18] concluded that the direct replacement of conventional steel bars with high strength bars, having the same area, resulted in a 27% increase in punching shear strength. The use of high strength bars and close reinforcement spacing did cause the test for specimen MB2 to fail prematurely due to bond distress. The addition of steel fibers into specimen MBF2 eliminated this bond failure and achieved a 51% punching shear increase from specimen MB2.

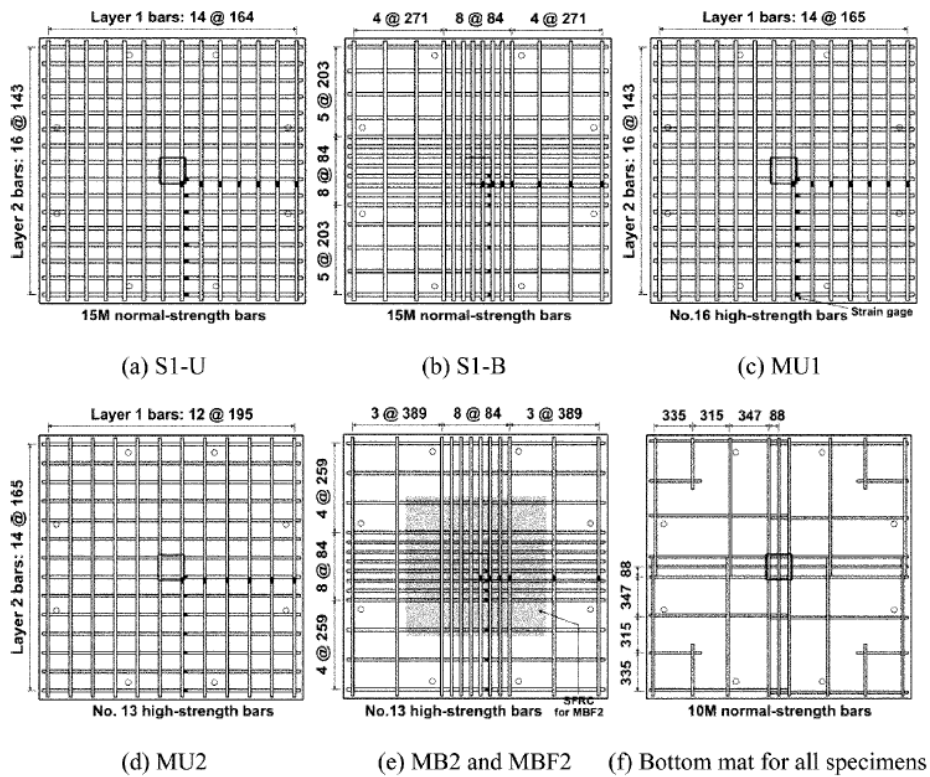


Figure 3-5: Yang slab specimens [18].

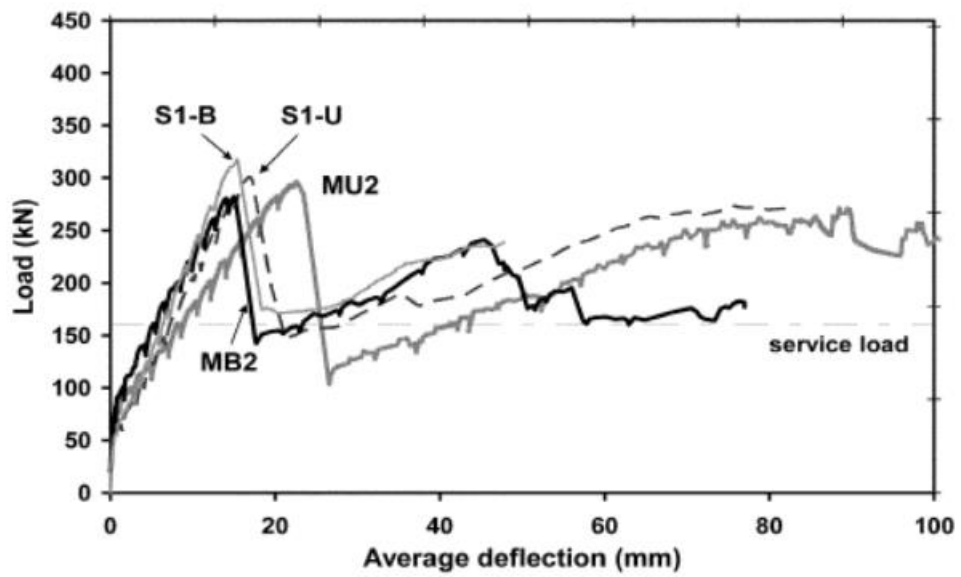
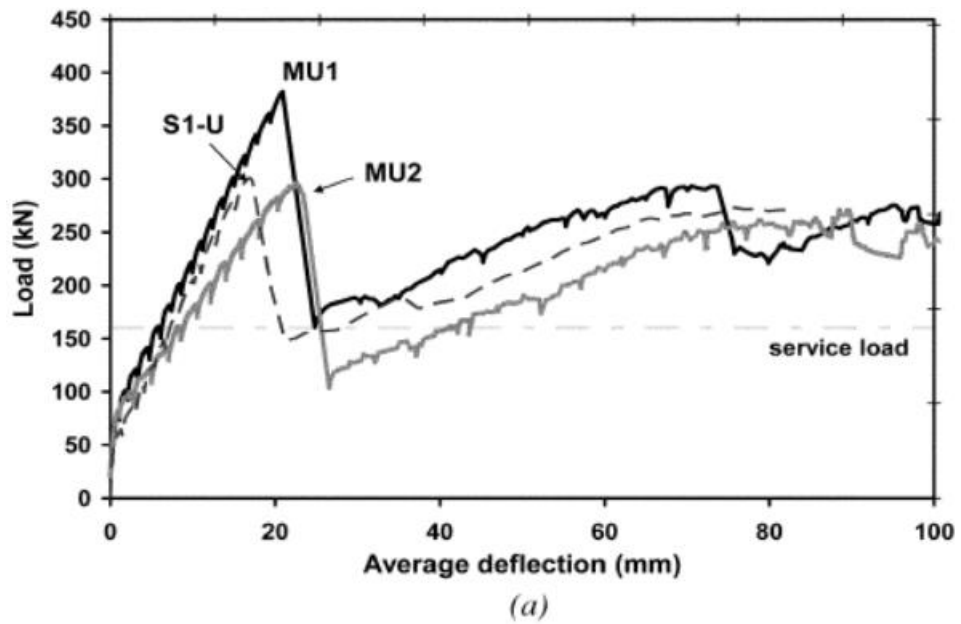


Figure 3-6: Yang load – deflection response [18].

### 3.4 Pourezza [63]

Pourezza [63] conducted an experimental investigation to examine the structural behavior of hybrid-fiber-reinforced concrete (HFRC) of two way slabs at Memorial University. He tested eight full scale interior slab-column connections with thicknesses 200 mm and 250 mm. The slabs measured 1900 mm × 1900 mm with a 250 mm × 250 mm column stub and were simply supported around the edges. Four slabs were tested with steel fiber volume fractions of: 0%, 0.68%, 0.8%, and 0.96%. Each SFRC slab also contained 0.2% macro-synthetic fibers. The compressive strength varied between 60-70 MPa and each slab contained a flexural reinforcement ratio of 1.3%. Pourezza's results showed an increase in punching shear capacity with an increase in steel volume fiber content (Figure 3-7). This increase was more noticeable in the 200 mm thick slabs than the 250 mm thick slabs. The slabs with higher steel volume content showed enhanced stiffness, ductility and energy absorption capacity.

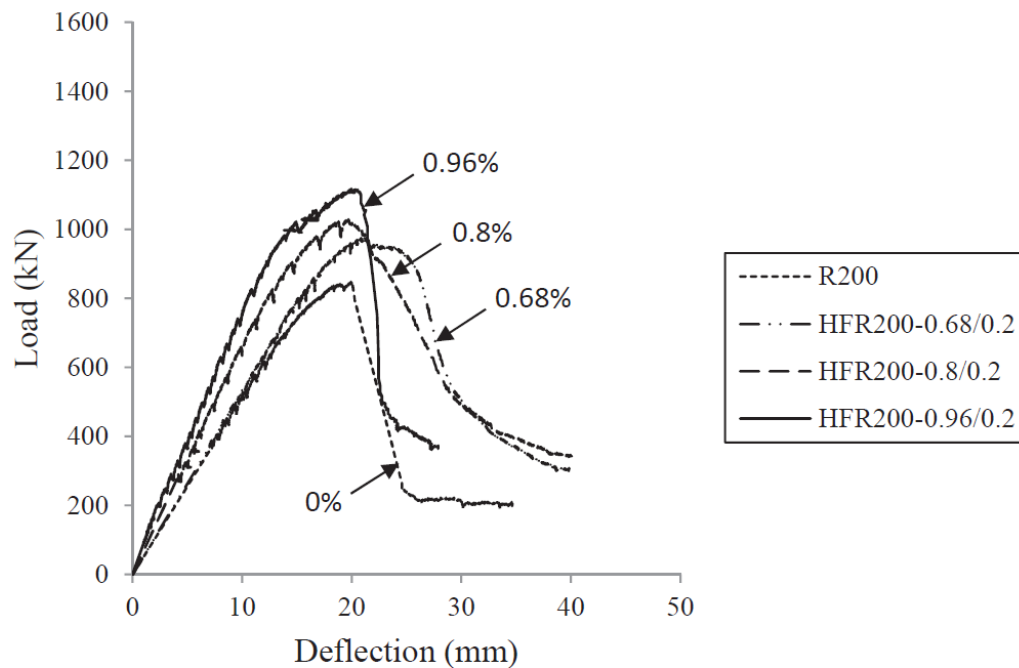


Figure 3-7: Pourezza load vs deflection curves [63].

### 3.5 Summary of Experimental Data

A summary of the slab specimens and properties is presented in Table 3.1.

Table 3.1: Summary of slab specimen properties

| Researcher      | Specimen | $P_{\max}$<br>[kN] | $f'_c$ [MPa] |      | $f_y$<br>[MPa] | $\rho$ |
|-----------------|----------|--------------------|--------------|------|----------------|--------|
|                 |          |                    | Slab         | SFRC |                |        |
| McHarg [19]     | NU       | 306                | 30           | -    | 434            | 0.0111 |
|                 | NB       | 349                | 30           | -    | 434            | 0.0215 |
|                 | FSU      | 422                | 39           | 41.5 | 434            | 0.0111 |
|                 | FSB      | 438                | 39           | 41.5 | 434            | 0.0215 |
|                 | FCU      | 329                | 37.5         | 33.4 | 434            | 0.0111 |
|                 | FCB      | 361                | 37.5         | 33.4 | 434            | 0.0215 |
| Lee [29]        | 35U      | 301                | 37.2         | -    | 445            | 0.0118 |
|                 | 35B      | 317                | 37.2         | -    | 445            | 0.0215 |
|                 | 55U      | 363                | 57.1         | -    | 445            | 0.0118 |
|                 | 55B      | 447                | 57.1         | -    | 445            | 0.0215 |
|                 | 65U      | 443                | 67.1         | -    | 445            | 0.0118 |
|                 | 65B      | 485                | 67.1         | -    | 445            | 0.0215 |
|                 | 90BF     | 386                | 46.9         | 92.1 | 449            | 0.0263 |
| Yang [18]       | MU1      | 382                | 35.3         | -    | 800            | 0.0118 |
|                 | MU2      | 296                | 35.3         | -    | 800            | 0.0118 |
|                 | MB2      | 282                | 35.3         | -    | 800            | 0.0136 |
|                 | MBF2     | 426                | 35.3         | 30.8 | 800            | 0.0136 |
| Pourezza [63]   | R200     | 848                | 70           | -    | 400            | 0.0130 |
| Genikomsou [56] | SB1      | 253                | 44           | -    | 400            | 0.0110 |

## Chapter 4

# FEA Modelling of Reinforced Concrete

The two principle structural actions of reinforced concrete is compression and tension. Therefore, in order for an FEA model to simulate the behavior of a reinforced concrete structure, the model must accurately describe how it behaves in compression and tension. The characteristics of this behavior is combined into a constitutive model. The concrete and reinforcement is represented with the proper type and size of finite elements. The boundary conditions and load application have to be accurately represented and the failure criteria must be defined. The following sections will describe the constitutive model used in this current thesis and its parametric definitions along with the other modelling techniques required to create a FEA model.

### 4.1 Concrete Constitutive Model

A constitutive model is a series of equations and idealizations that are used to numerically approximate the behavior and response of a material. Numerous concrete constitutive models exist in the literature. Each finite element computer program adopts a specific constitutive model. The commercial FEA program ANSYS implements the Darwin and Pecknold [64] inelastic concrete model whereas the FEA program ABAQUS offers three different concrete models: brittle cracking model, smeared crack model, and the concrete damaged plasticity model. Each constitutive model offers advantages depending on the analysis being conducted. For example, the brittle cracking model is intended for applications in which concrete behavior is dominated by tensile cracking and compressive failure is not important and

is treated as linear elastic. The concrete damaged plasticity (CDP) model is intended for the analysis of concrete under monotonic, cyclic, and/or dynamic loading. It features tension cracking and compression failure modes and represents the complete inelastic behavior of concrete in tension and compression. The unique feature of CDP model is that it takes into account the degradation of the elastic stiffness induced by plastic straining in both tension and compression. Punching shear failure is most accurately modeled using the elasto-plastic damage model [53] due to the non-associated potential flow model that is aimed at providing a more realistic simulation of the concrete material under punching shear [52]. A summary of the CDP model and the definition of its numerical and material parameters to be used in the FEA model of this current study are described in the following sections.

The CDP model is a modification of the Drucker-Prager yield criterion which is one of the strength hypothesis most often applied to concrete. The CDP model was developed by Lubliner et al [65] and latter refined by Lee & Fenves [66]. It is a pressure dependent model for determining whether a material has failed or undergone plastic yielding. Details of the mathematical formulation of the CDP model are provided in [65] and [66].

The CDP model requires defining five parameters to solve the Drucker-Prager plastic flow function and the yield function proposed by Lubliner [65]. These parameters include: shape factor, eccentricity, bi-axial compressive stress ratio, dilation angle, and viscosity. The shape of the state of stress utilized in the CDP model is represented as a three dimensional cone. The states of stress corresponding to material failure are located on the surface of the cone and the states of stress corresponding to safe material behavior are located inside the cone. The Drucker-Prager strength hypothesis assumed that the cross section of the failure cone is a circle (Figure

4-1). However, to fully describe the actual behavior of concrete, Lubliner et al [65] found that the cross-section of the cone was not an actual circle but rather defined by a shape factor,  $K_C$  (Figure 4-2). The  $K_C$  factor is the ratio of the distances between the hydrostatic axis and the compression meridian and the tension meridian. This factor expresses the shape of the yield surface in the deviatory plane. Lubliner et al [65] recommends to assume the value of  $K_C$  as  $2/3$ . The shape of the compression and tension meridians is not constant but rather assumes the form of a hyperbola. The rate of change of these meridians to its asymptote is known as the eccentricity. Lubliner et al [65] defines the value of eccentricity as 0.1 which is also an approximation of the ratio of the uniaxial concrete compressive strength to its tensile strength. To fully define the Drucker-Prager yield function the ratio of biaxial compressive stress to uniaxial compressive stress needs to be expressed. For normal strength reinforced concrete this ratio is defined by Kupfer's [67] biaxial concrete stress-strain curve as 1.16 (Figure 4-3).

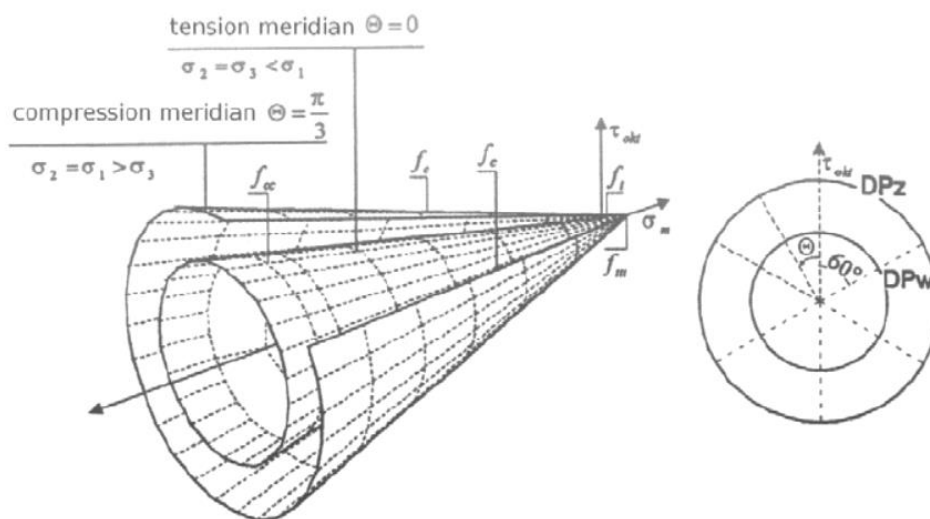


Figure 4-1: Drucker-Prager boundary surface [68].

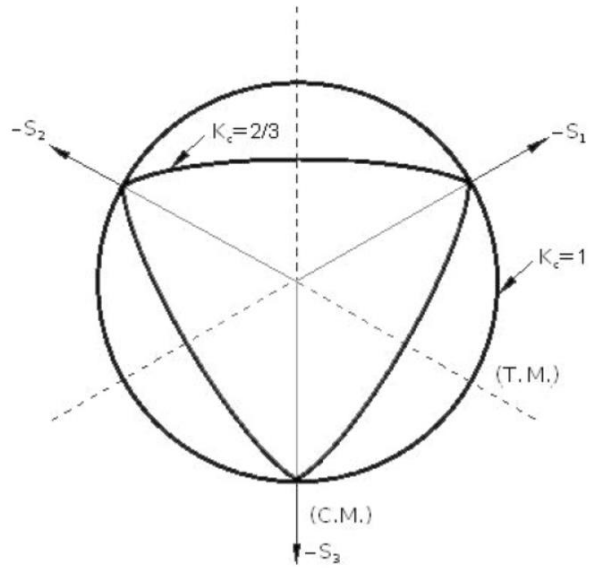


Figure 4-2: Deviatoric cross-section of failure surface in CDP model [69].

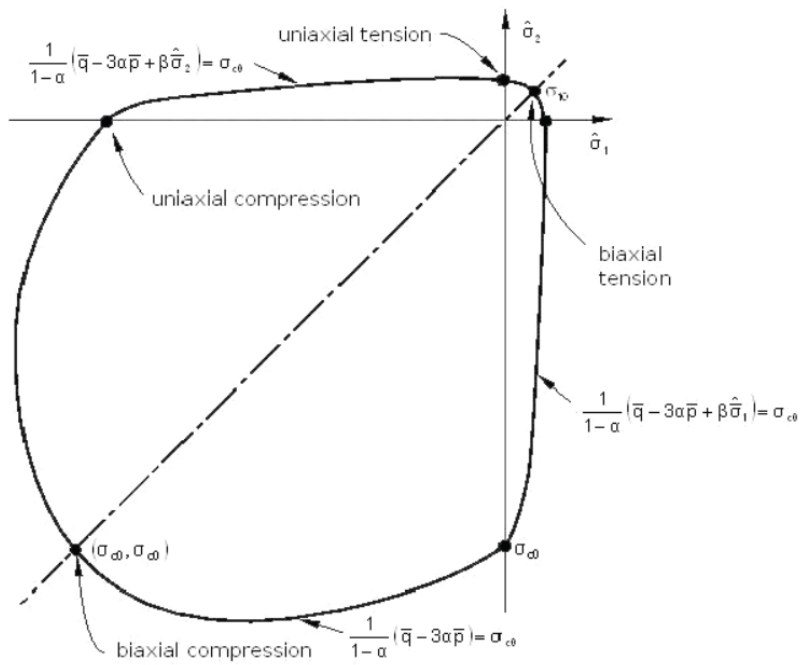


Figure 4-3: Concrete biaxial stress-strain curve [69].

Another parameter of the CDP model is the definition of the angle of inclination of the failure surface towards the hydrostatic axis measured in the meridional plane (Figure 4-4). This

angle is referred to as the dilation angle,  $\psi$ . It is interpreted physically as the ratio of volume change to shear strain caused by the large inelastic strains that occur when nonlinear materials like concrete are deformed due to stress. The dilation angle can be considered as a concrete internal friction angle and is usually between  $36^\circ - 40^\circ$  [68].

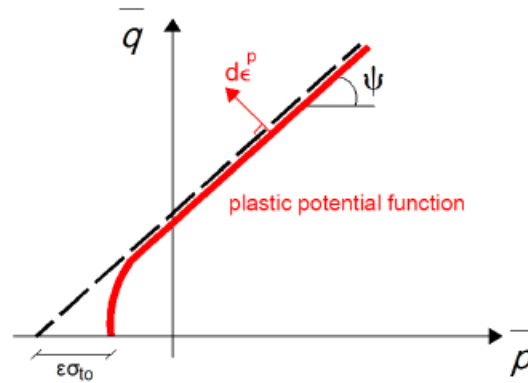


Figure 4-4: Dilation angle in meridian plane

A sensitivity analysis was conducted to define the value for this parameter and to analyze the effect this parameter has on the punching shear behavior. Slab specimen NU [19], which was described in Chapter 2, was modeled and examined for dilation angles ranging from  $20^\circ$  to  $50^\circ$  while all other parameters remained constant. Figure 4-5 illustrates the change in load-deflection response due to the changes in the dilation angle. It is observed that the punching shear response increases with an increase in dilation angle. At high dilation angle values, as shown when  $\psi$  equaled  $50^\circ$ , the slab response becomes very ductile and does not converge to a failure load. At low dilation angle values, as shown when  $\psi$  equaled  $20^\circ$ , the slab response becomes very brittle and the slab fails prematurely compared to the experimental punching shear load. The dilation angle of  $40^\circ$  provides a good agreement with the test results of the load-deflection diagram. A second sensitivity analysis on the dilation angle was conducted using slab specimen SB1 from

Genikomsou & Polak [56]. The results again show that a dilation angle of  $40^\circ$  best fit the experimental value (Figure 4-6). Nana et al. [61] used the same dilation angle value in their FEA modelling research.

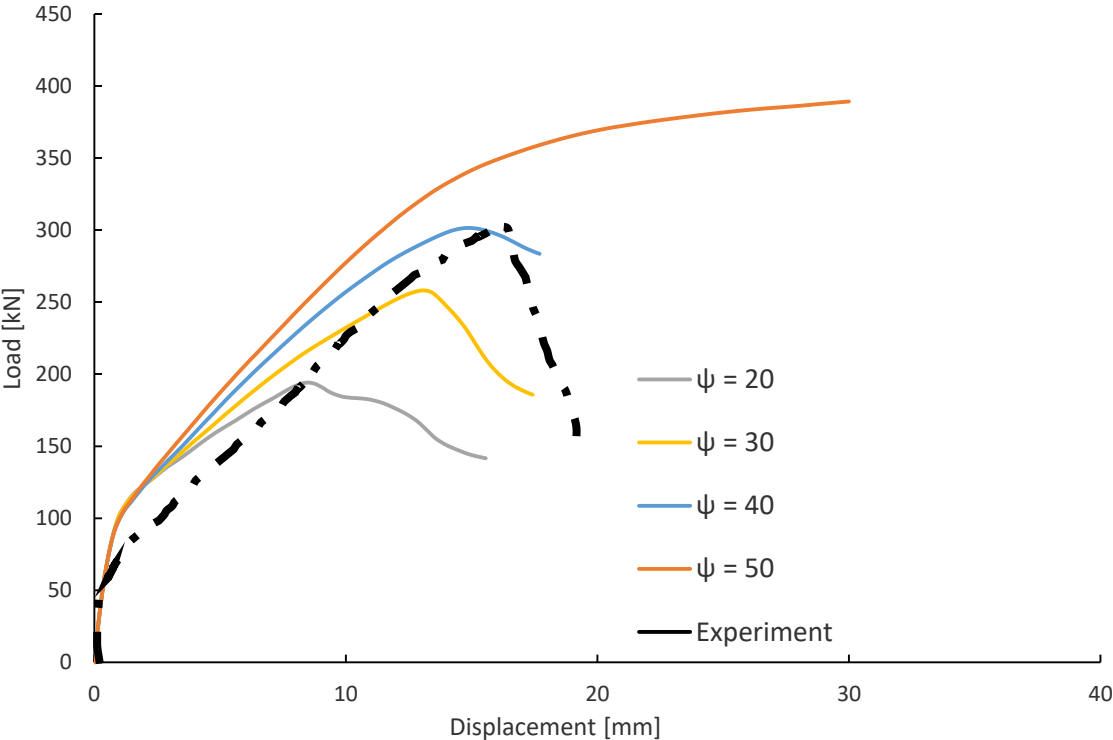


Figure 4-5: Parametric study – dilation angle specimen NU.

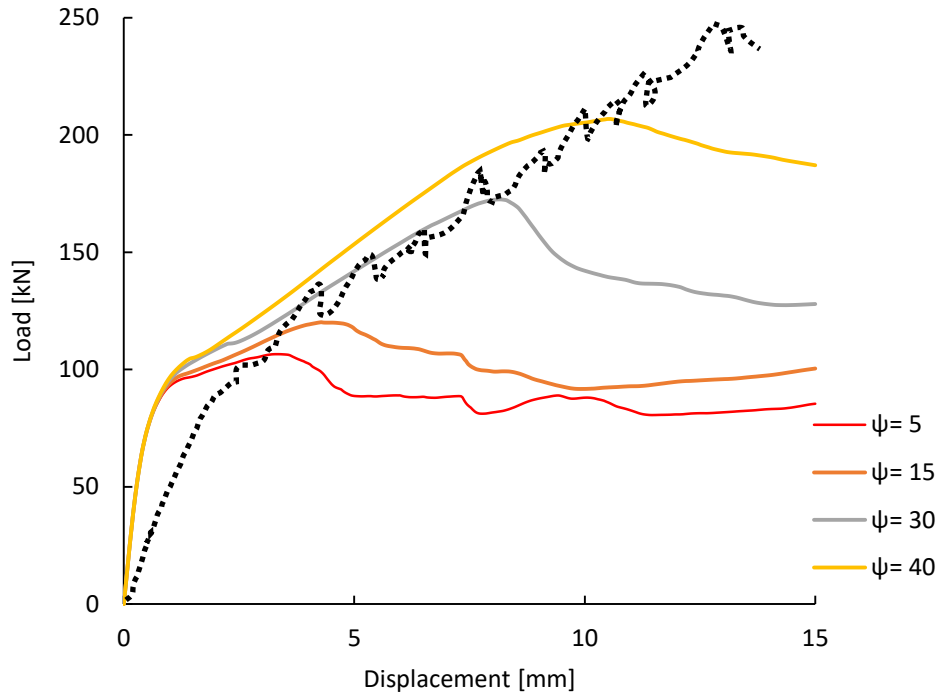


Figure 4-6: Parametric Study – dilation angle specimen SB1.

The viscosity parameter,  $\mu$  is introduced into the CDP model to avoid convergence problems when running a static analysis. Viscosity is required to prevent a convergence problem in the model which occurs in FEA when modelling non-linear brittle materials like concrete. The viscosity allows the plastic potential surface area to be exceeded in certain sufficiently small steps. Lee & Fenves [66] recommend setting  $\mu$  to 15% of the time increment step. Due to the high non-linearity of a punching shear finite element simulation, the time increment step could not be fixed. The time increment step was set to ‘automatic’ with an initial step size of 0.0003. This was done so the program could increase or reduce the time increment to find a stable solution in the Newton-Raphson solver.

The value of  $\mu$  to be used in the model of this current study was determined from a FEA parametric study using slab specimen NU [19]. Values of  $\mu$  tested ranged from 0.00001 to 0.01.

The results in Figure 4-7 show that when the viscosity parameter approaches zero, the slab behaves very brittle and fractures prematurely. As viscosity is increased, the material becomes increasingly stiffer and the load-deflection curves approaches the response observed in the experiment. For large viscosity values, the material behaves too stiff and does not represent the true load-deflection curve. The viscosity value of 0.0001 appears to be the best fit with the experimental data. Genikomsou & Polak [56] used a very similar value for  $\mu$  of 0.000085 when they modeled their slab specimen in a static analysis.

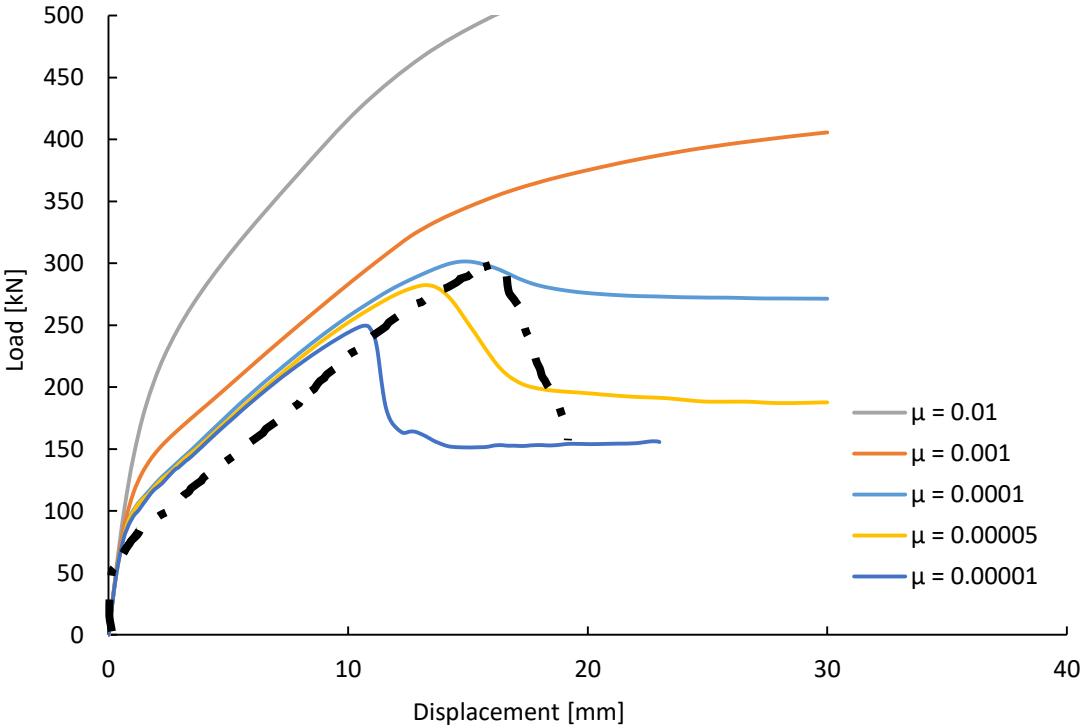


Figure 4-7: Viscosity parametric study using slab

The CDP model features tensile cracking and compressive failure modes. To describe these failure modes the CDP model requires the definition of the compressive and tensile stress-strain behavior. The following sections describe how these two material parameters are defined

in the CDP model. The equation for describing the full range of the concrete compressive stress-strain behavior is adopted from the literature. The equation for the tensile stress-strain behavior is also adopted from the literature. However, the literature review did not reveal a model that accounted for all the parameters that affect tension-stiffening. Hence, an equation will be adapted, modified, and calibrated in the next chapter to produce an expression that includes variables for that account for concrete strength, flexural reinforcement ratio, steel fibers and the strength of the reinforcement.

#### 4.1.1 Numerical Model for Concrete Compressive Behavior

The CDP model defines the compressive behavior of concrete through a yield stress versus inelastic strain relationship. The following discussion is illustrated in the stress-strain curve provided in Figure 4-8. The total strain,  $\varepsilon_c^T$ , is composed of an elastic portion,  $\varepsilon_c^{el}$ , and an inelastic one,  $\varepsilon_c^{in}$  :

$$\varepsilon_c^T = \varepsilon_c^{el} + \varepsilon_c^{in} \quad (4-1)$$

Where;  $\varepsilon_c^{el} = \frac{f_c}{E_o}$

The CDP model defines the degradation of concrete in compression through the use of the compressive damage vs inelastic strain curve. The expression for the damaged parameter,  $d_c$  is given as [69]:

$$d_c = 1 - \frac{\sigma E_c^{-1}}{\varepsilon_c^{pl} \left( \frac{1}{b_c} - 1 \right) + \sigma_c E_c^{-1}} \quad (4-2)$$

As described by Birtel & Mark [70] and recommended by Genikomsou & Polak [59], the plastic strain,  $\varepsilon_c^{pl}$ , is proportional to the inelastic strain using the constant factor,  $b_c$ ;

$$\varepsilon_c^{pl} = b_c \varepsilon_c^{in} \quad (4-3)$$

Compressive damage occurs in the inelastic range of the stress-strain curve after the concrete has reached its ultimate stress and can no longer carry any more stress. The inelastic strains are not recoverable which cause permanent deformation and the concrete not to return to its original stress-strain state upon unloading. In compression, concrete is assumed to be elastic until it deviates from linearity at a stress level of  $0.4f_c'$ . Hence, concrete is defined to behave in the elastic region with an elastic modulus,  $E_c$ . For the proposed model  $E_c$ , was chosen for normal concrete based on CSA A23.3-14 [10] as expressed in Equation (4-4). For SFRC,  $E_c$  is assumed as proposed by Lee et al [29] in Equation (2-8):

$$E_c = 3300\sqrt{f_c'} + 6900 \quad (4-4)$$

The elastic modulus of the concrete,  $E_c^{in}$ , will be degraded when the specimen is re-loaded and will not be as stiff as the initial elastic modulus,  $E_c$ . The relationship between the degraded modulus,  $E_c^{in}$ , and the original modulus,  $E_c$ , is provided by the following expression:

$$E_c^{in} = E_c(1 - d_c). \quad (4-5)$$

This effect is significant in cyclic loading where the load is removed and re-applied a number of times. However, in the current investigation, the load is applied monotonically and hence the effect of ‘damage’ can be ignored.

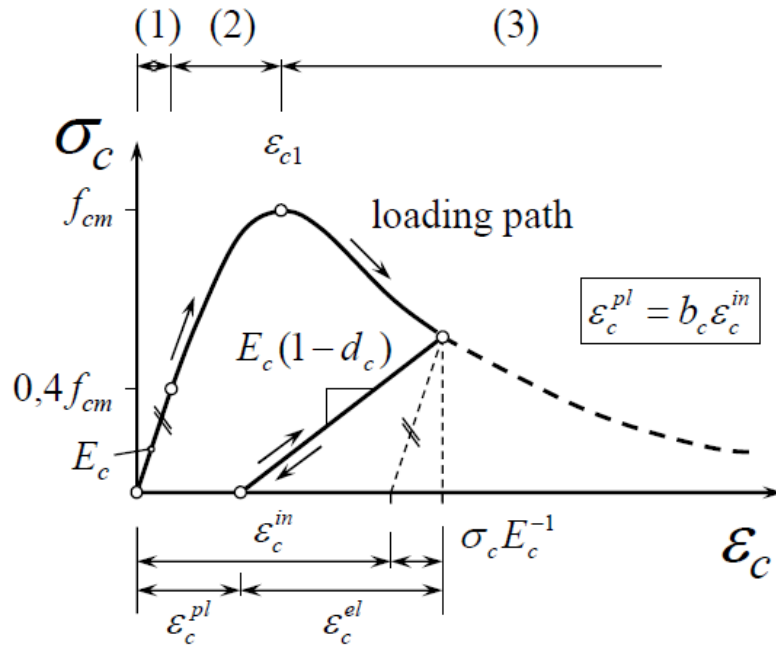


Figure 4-8: Compressive stress vs strain curve [69].

The model proposed in this thesis adopts the compressive stress-strain expression by Collins & Mitchell [25] for reinforced concrete without steel fibers and by Lee et al [29] for SFRC. The average ultimate compressive strain for normal concrete is assumed to be 0.0035 as defined in CSA A23.3 [10]. There is no generally accepted value for the ultimate compressive strain for SFRC. The proposed model for SFRC will reference the work by Wang [30] and set limits on ultimate compressive strain as:  $\epsilon_u = 0.005$  for  $V_f \leq 0.5\%$  and  $\epsilon_u = 0.02$  for  $V_f > 0.5\%$ .

#### 4.1.2 Numerical Model for Concrete Tensile Behavior

Punching shear failure is highly dependent on the tensile response of concrete since punching shear failure is initiated by tensile cracking [2]. Therefore, the modelling of the tensile stress-strain behavior of a reinforced concrete slab will be a main focus of this study. From the literature review it was noted that the punching shear strength is influenced by the concrete

strength, flexural reinforcement ratio, strength of the reinforcing steel, and the presence of steel fibers. Numerous forms of the tension-stiffening model were presented in the literature review but none of the models had the versatility to account for changes in the values of all of the parameters that influence punching shear. The objective of this thesis is to create a robust model that can be employed across a wide range of specimens. Therefore, this tension stiffening curve will account for concrete strength, flexural reinforcement ratio, strength of reinforcing steel, and the presence of steel fibers.

The CDP model enables the simulation of the degradation of tensile behavior by specifying the tensile damage versus average cracking strain (Figure 4-9). The expression for the damaged parameter,  $d_t$  is given as [69]:

$$d_t = 1 - \frac{\sigma E_c^{-1}}{\varepsilon_t^{pl} \left( \frac{1}{b_t} - 1 \right) + \sigma_c E_c^{-1}} \quad (4-6)$$

The plastic strain,  $\varepsilon_t^{pl}$ , is proportional to the inelastic strain using the constant factor  $b_t = 0.1$  as recommended by [70] where;

$$\varepsilon_t^{pl} = b_t \varepsilon_c^{in} \quad (4-7)$$

The first pair of data for the tensile damage/cracking strain curve must correspond with the onset of plasticity at point  $\varepsilon_{cr}$ . The strain in the first pair is taken as zero (i.e.  $\varepsilon_1 = \varepsilon_{cr} - \varepsilon_{cr}$ ), the second pair as  $\varepsilon_2 = \varepsilon_1 - \varepsilon_{cr}$ , and the third pair as  $\varepsilon_3 = \varepsilon_u - \varepsilon_{cr}$ .

As explained in the concrete compressive damage section, accounting for damage is only significant for cyclic loaded structures and may be ignored for this model.

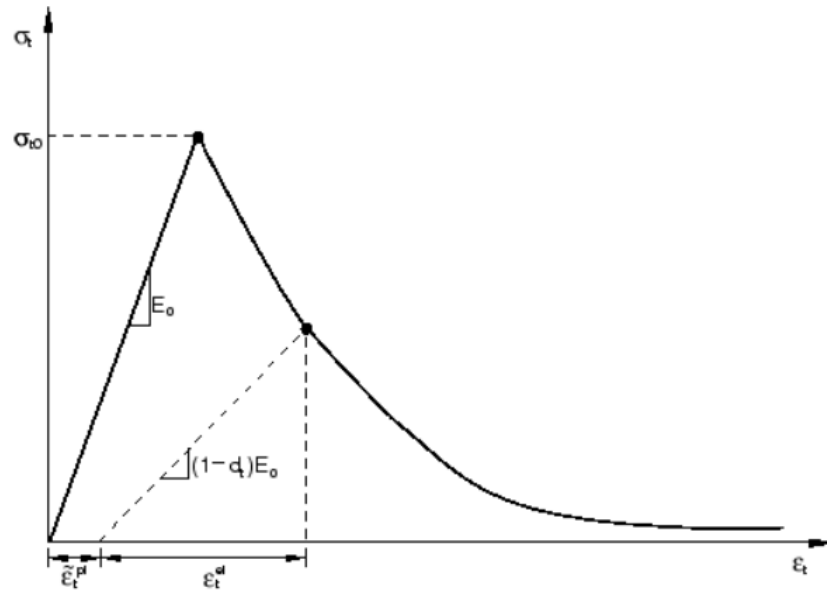


Figure 4-9: Tension stiffening curve with tensile damage [69].

The exponential decay model developed by Hsu & Mo [44] is selected to represent the tensile behavior of concrete for the present study as it is easily adaptable to account for the tension stiffening parameters under consideration and is suitable for use with the CDP model. The expression was also used in the finite element simulation of punching shear by Youm et al [54] described in Chapter 2 and good results were obtained. The first stage of the tensile behavior is assumed linear up to the point of cracking.

For SFRC, the use of steel fibers in the concrete mix does not appear to affect the response up to and including first cracking [50]. Even though Abrishami & Mitchell [45] reported an increase in cracking stress at fiber volume contents above 1%, an increase in cracking strength is not expected to be substantial for the range of fiber volumes encountered in the slab specimens in the present study and in those that would be practically used in construction. Hence, the same expression for the uniaxial tensile strength for non-fibrous concrete will also be used in this material model for SFRC.

Hsu & Mo [44] provided a tension stress-strain equation which has been adapted for this proposed model. The model is expanded to define a weakening function,  $n$ , and ultimate strain factor,  $Y$ , as functions of compressive strength, flexural reinforcement ratio, steel fiber content, and reinforcement yield strength. The expression will consider the tension stiffening and local bond effects to produce a homogenized stress-strain relationship capable of simulating the post-cracking behavior. The ultimate tensile strain will be determined and calibrated using the experimental load – deflection curves and expressed as a function of the cracking strain. Tension stiffening for the concrete damaged plasticity model is specified by defining the tensile stress versus cracking strain curve for the post-failure stress/strain relation. The adopted tension stiffening stress-strain relation is:

$$\sigma_t = E_c \varepsilon_t \quad \text{where } \varepsilon_t \leq \varepsilon_{cr} \quad (4-8)$$

$$\sigma_t = f_t \left( \frac{\varepsilon_{cr}}{\varepsilon_t} \right)^n \quad \text{where } \varepsilon_U > \varepsilon_t > \varepsilon_{cr}$$

Where;  $f_t = 0.33\sqrt{f'_c}$

Cracking strain,  $\varepsilon_{cr} = \frac{f_t}{E_c}$

Weakening function,  $n = f(f'_c, \rho, V_f, f_y)$

Ultimate strain,  $\varepsilon_U = Y \varepsilon_{cr}$

Ultimate strain factor,  $Y = f(f'_c, \rho, V_f, f_y)$

## 4.2 Reinforcement Modelling

Steel reinforcement can be modeled using either smeared reinforcement in the concrete, as discrete one-dimensional elements, or as solid 3D elements. The smeared reinforcement technique creates a composite layer of steel by spreading or smearing the reinforcement out over

the concrete surface. The use of smeared reinforcement is generally acceptable for simulating the global response of a structure but it is not capable of analyzing local response of the reinforcement. For this, it is more realistic to model reinforcement as discrete 2D truss or beam elements. Since the reinforcement acts in a uni-axial direction, it is reasonable to model it as two-node linear truss elements (T3D2). The diameter and spacing of the bars are modeled to match the diameter and spacing of the physical model. The ‘embedded’ method was used to simulate the bond between the concrete and the reinforcement. The embedded technique allows the placement of reinforcement anywhere within the concrete specimen and is not restricted by the concrete mesh location. The embedded constraint ties the nodes of the reinforcement to the nodes of the concrete without having to share the same node as shown in Figure 4-10. Although this technique assumes a perfect bond interaction of the reinforcement with the concrete, the effects of bond slip is taken into account in the tension-stiffening model. The steel reinforcement was assigned as a linear elastic material with a Young’s modulus of 200,000 N/mm<sup>2</sup> and Poisson ratio 0.3. The yield strength and plastic material properties were based on the information provided in the test data.

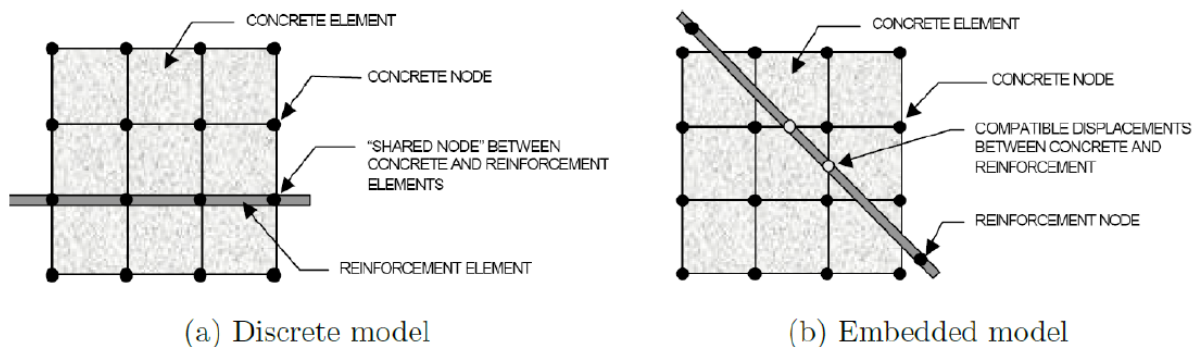


Figure 4-10: Modelling of reinforcement and its interface with concrete [71].

### **4.3 Finite Element Type**

Areas of the slab-column interface within the punching failure zone are under a complex tri-axial stress state. Complex stress states should be presented in a three-dimensional stress space in order to describe the tri-axial stress state [68]. Three-dimensional solid continuum elements are used for this purpose to discretize the concrete elements. The idealization of representing concrete with 3D solid first order elements can cause the numerical problem of shear locking where the element behaves too stiff in bending applications. This is caused from artificial shear stresses being introduced in the element as the element bends and cannot maintain a curved shape. Shear locking can result in incorrect displacements and stresses. To avoid this phenomenon, eight-noded hexahedral (brick) elements were used with reduced integration (C3D8R) to model the concrete.

### **4.4 Finite Element Discretization**

Due to the cracking in reinforced concrete elements, the response of the member becomes dependent on the size of the mesh. Such behavior is known as mesh sensitivity whereby meshes of varying sizes do not exhibit the same load – deflection response [72]. In reinforced concrete, the properties of a discretized element may differ between element sizes and from element to element. Some elements may contain steel reinforcement while others do not and the cracking failure pattern in a slab is not evenly or symmetrically distributed throughout all elements. Coarse meshes tend to lead to an increase in the post crack energy absorption capacity and do not converge on a unique solution [72]. The mesh dependency is more affected by the inelastic tensile response rather than the compressive behavior [73].

Mesh sensitivity is usually overcome by using a stress – displacement approach instead of a post failure stress – strain relation [59]. It is customary for models that do not contain reinforcement in significant areas to use a stress – displacement curve because a stress – average strain relationship will introduce unreasonable mesh sensitivity [69]. The literature review presented several FEA models that were defined by a stress – displacement response and used the fracture energy of concrete as a material property. However, since fracture energy is a property of plain concrete, these models neglected to account for the interaction of the reinforcement and the concrete. Concrete slabs used in practice often have a concentration of flexural reinforcement over the columns due to the high concentration of tensile-stress and to safeguard against punching shear. A robust FEA material model should be able to account for the steel-concrete interaction for a range of reinforcing ratios. A post failure stress-average strain relation was used in this thesis because it is easily adapted to account for tension stiffening. Representing concrete with a tensile stress-strain relation introduces mesh sensitivity into the FEA model.

A mesh sensitivity study was performed on slab specimen NU [19] using four different mesh sizes: 15 mm, 20 mm, 25 mm, and 30 mm to investigate the effect of varying the mesh size on the load-deflection response of the slab. The FEA model set-up with a mesh size of 20 mm is illustrated in Figure 4-11. The load – deflection response of the slabs with varying mesh size is shown in Figure 4-12. The intent is to establish a relationship between the mesh size and the tension stiffening curve. The mesh size of 15 mm is a fine mesh with 10 elements through the slab thickness. This mesh size required a considerable amount of computation effort and showed a higher punching shear load (326 kN). It also displayed a clearly defined descending branch of the load-deflection curve after the peak load. The coarse mesh sizes of 30 mm and 25 mm

underestimated the peak load and did not provide a clearly defined post peak descending branch of the load-deflection curve. The curves showed a slight depression after the peak load but the load-deflection response rapidly started to descend again. This is indicative of the high energy absorption capacity of coarse meshes discussed earlier. The mesh size of 20 mm provided a sufficient number of elements to accurately predict the punching shear behavior of the slab.

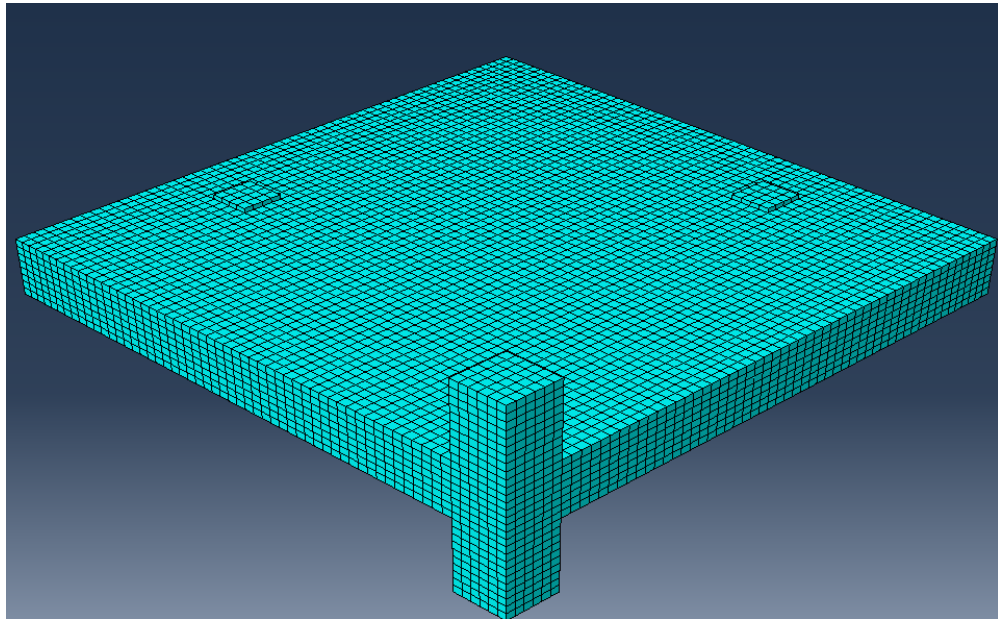


Figure 4-11: Sample mesh size of 20 mm

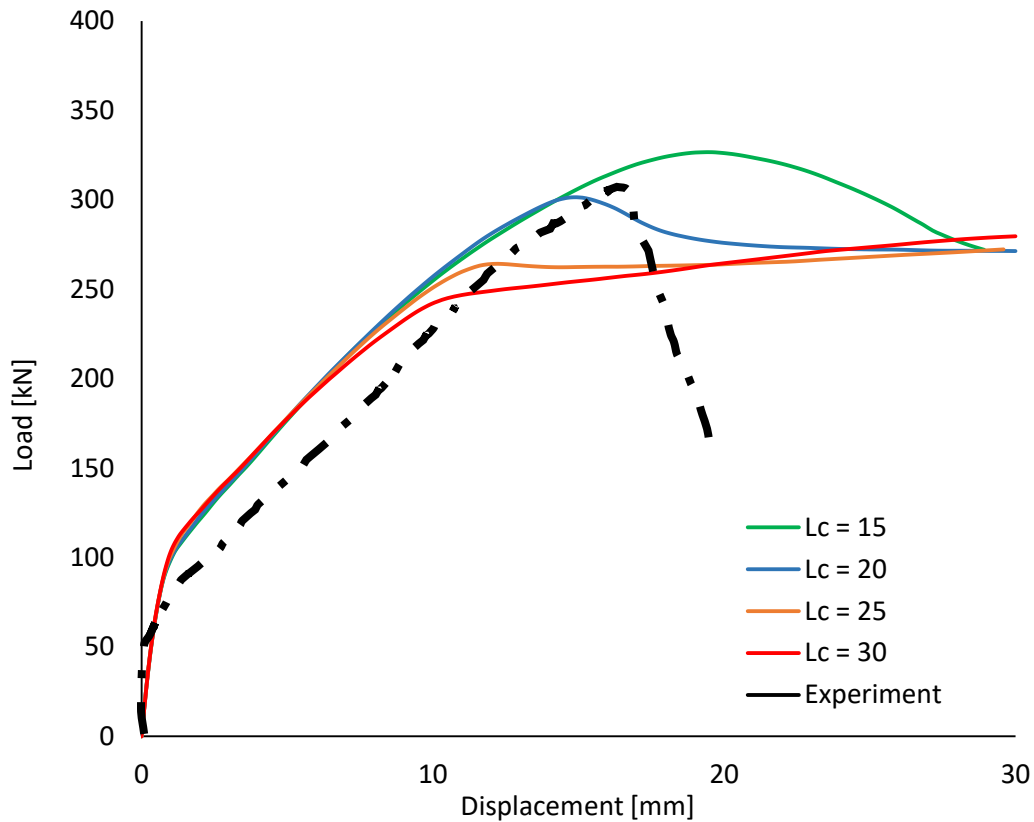


Figure 4-12: Parametric Study – mesh size.

The tension-stiffening response of the concrete will need to be adjusted in order to develop a relationship to correlate the mesh size with the load-deflection response of a concrete element. The Hsu & Mo [44] expression (Equation (4-8)) used an exponential function,  $n$ , to adjust the degree of tension stiffening in the slab. For fine mesh sizes, which over-estimate the capacity of the slab,  $n$  would have to be increased in order to increase the punching shear strength. Likewise, for coarse mesh sizes, which underestimate the capacity of the slab,  $n$  would have to be decreased. To achieve mesh size independence the weakening function,  $n$ , was calibrated with the experimental load-deflection response for mesh sizes 30 mm, 25 mm, and 15 mm (see Figure 4-13 to 4.29). The ‘best-fit’ values of  $n$  for each mesh size,  $L_c$ , is shown in Figure 4-16 and the relationship between both is given as;

$$n = 0.665 - 0.014L_C$$

(4-9)

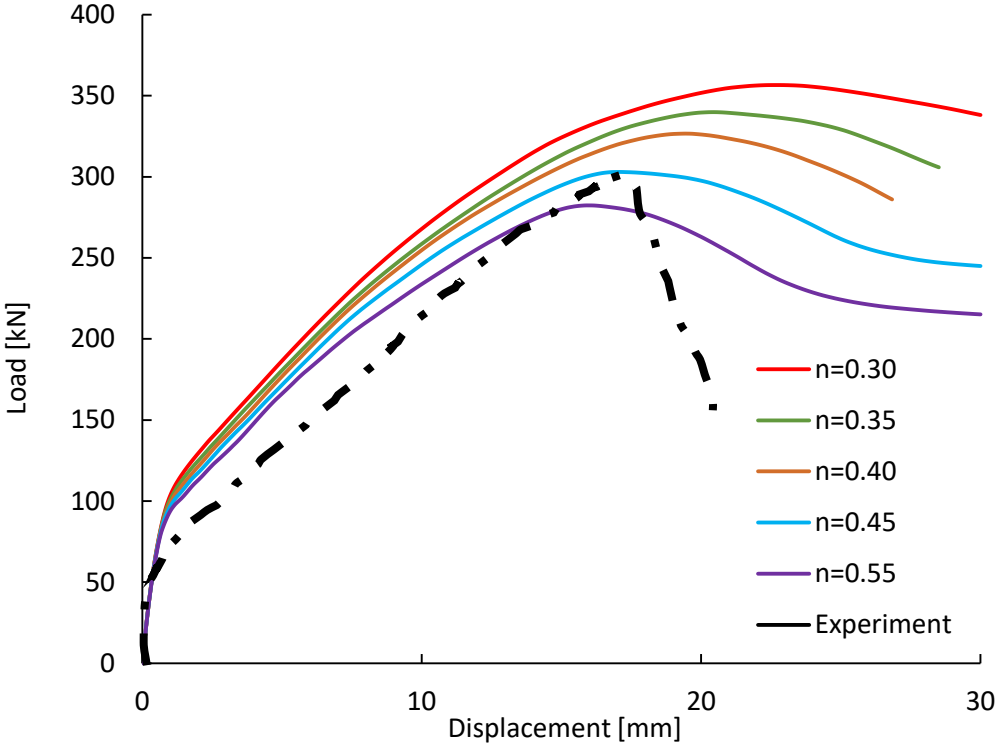


Figure 4-13: Mesh size calibration for 15 mm mesh.

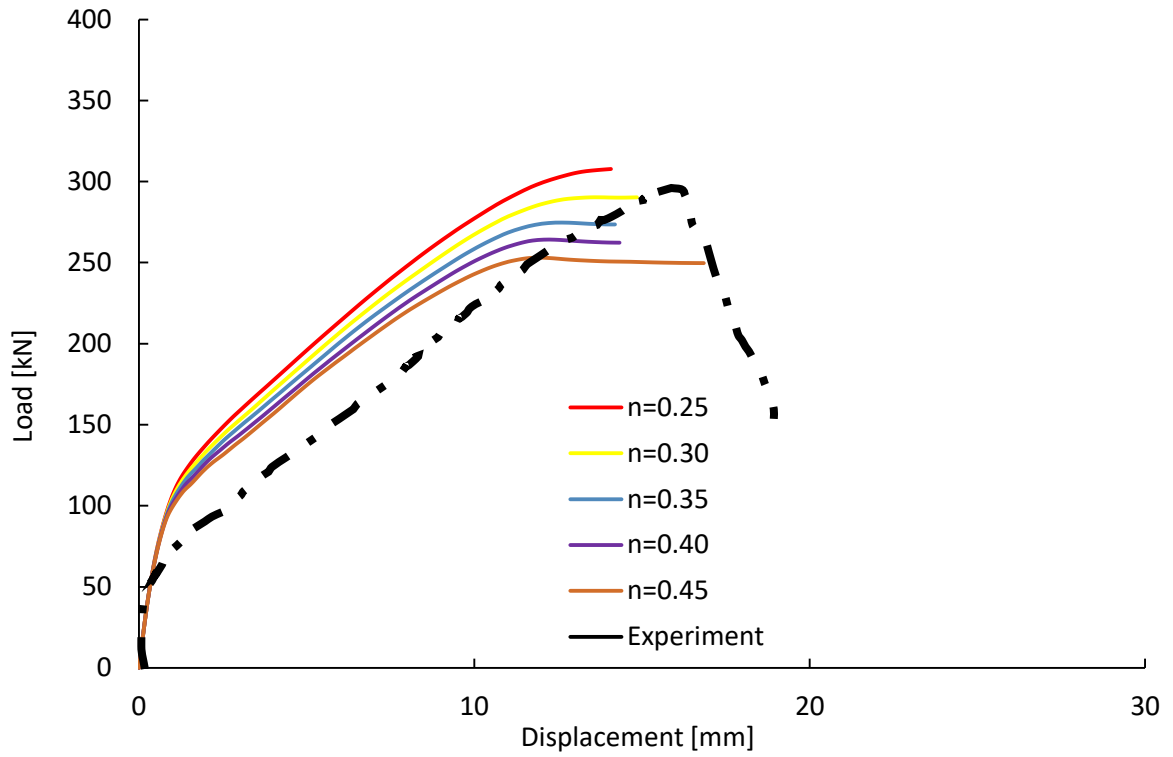


Figure 4-14: Mesh size calibration for 25 mm mesh.

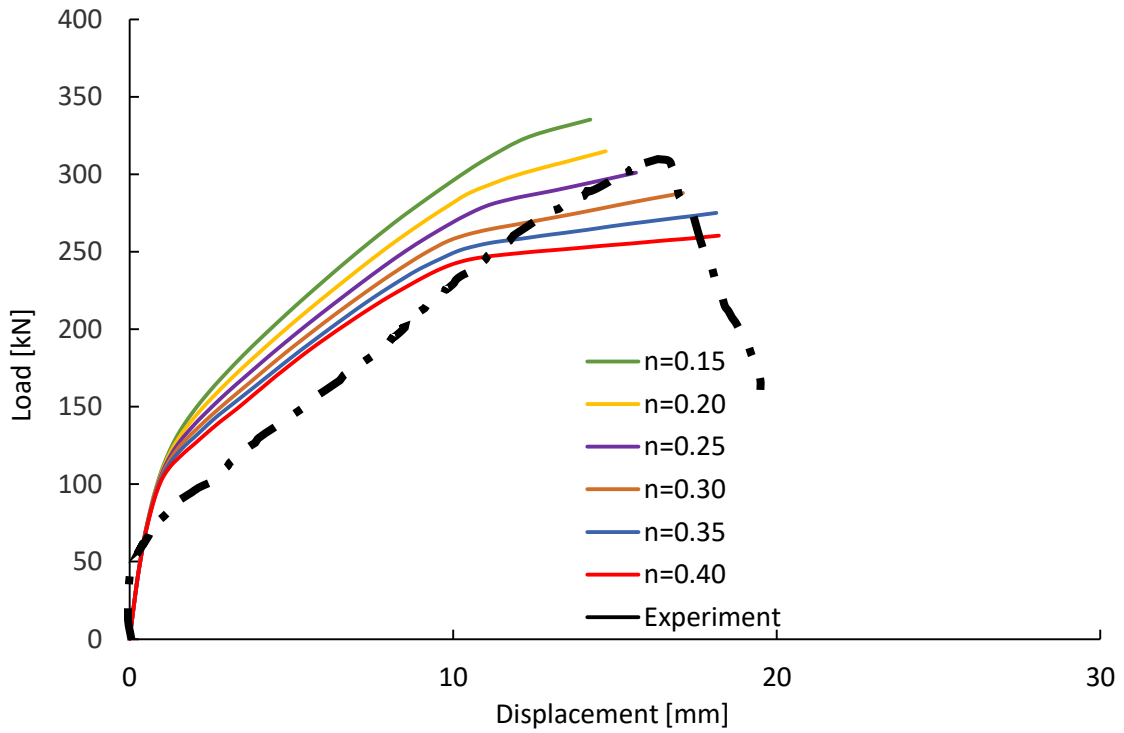


Figure 4-15: Mesh size calibration for 30 mm mesh.

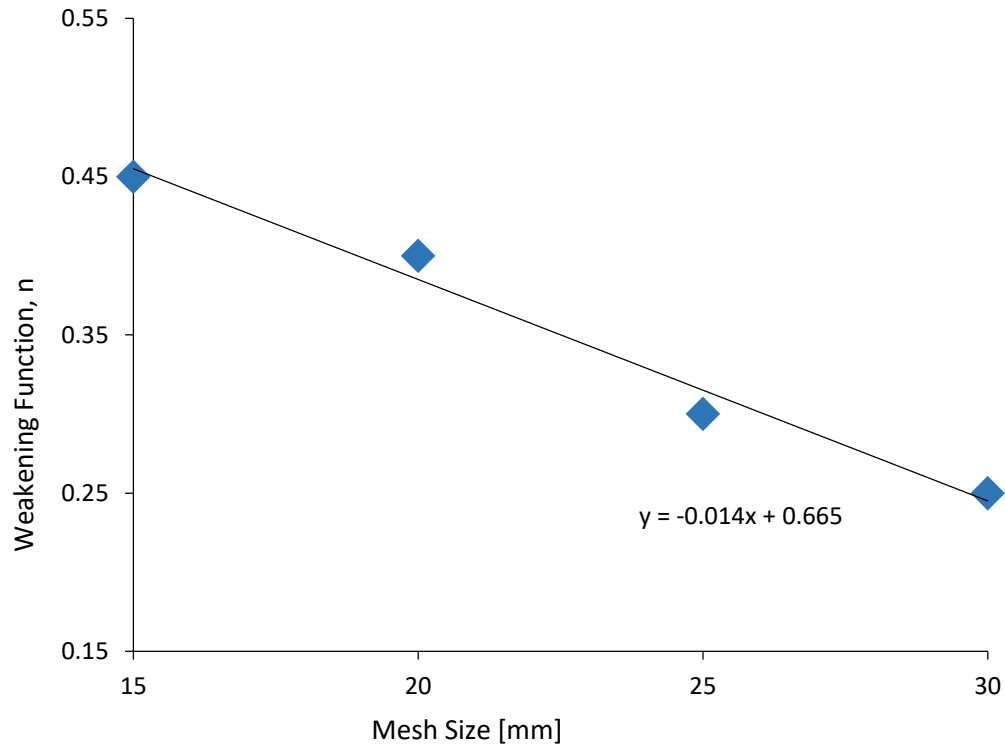


Figure 4-16: Weakening function vs mesh size.

## 4.5 Boundary Conditions and Load Application

A schematic of the experimental set-up used in the experimental program for the slab specimens chosen to calibrate the model is shown in Figure 4-17. The slab was supported by a central column stub (225 mm square) that rested on a steel plate at the bottom and was loaded by eight concentrated points pulled in tension around the perimeter of the slab until the column stub punched through the slab. To model this set-up in FEA it is recognized that the slab specimen behaves symmetrically about its two planar axes. To mitigate computation time during the analysis, only a quarter of the slab will need to be modeled (Figure 4-18). For structural stability, horizontal restraints are specified on the symmetry planes and a vertical restraint was applied on the bottom of the column stub to simulate the simply-supported condition of the test. The slab

was loaded using a displacement that was applied on the steel plates on the top surface of the slab to simulate the loading that was applied in the experiment.

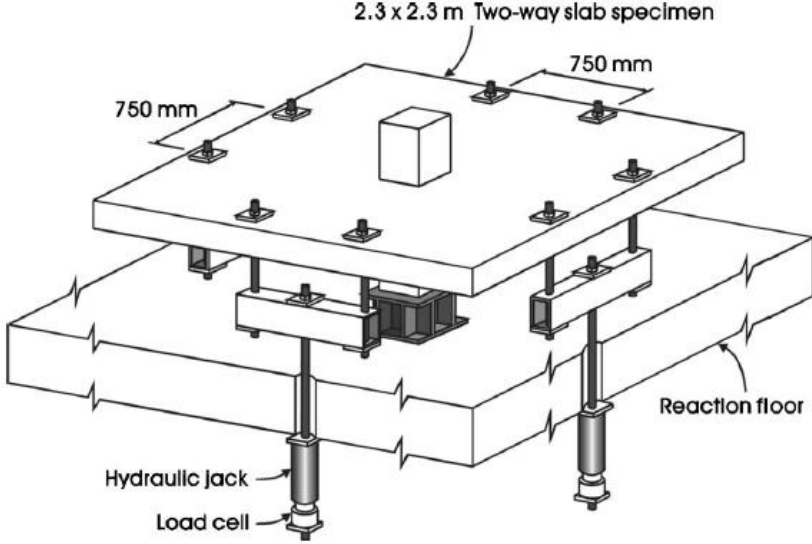


Figure 4-17: Test set-up [19].

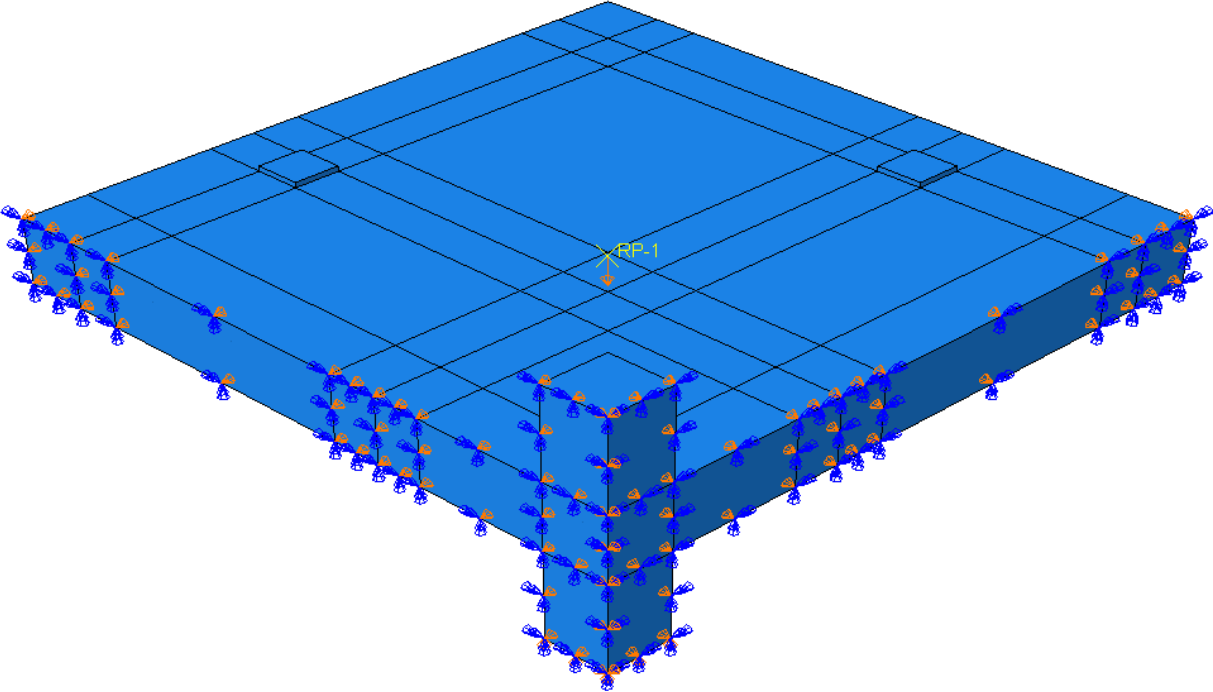


Figure 4-18: Abaqus quarter slab model.

## 4.6 Failure Criteria

The failure criteria used in the development of this model was defined by the shape of the load – deflection response of the slab. The load – deflection curve provides a good indication of the behavior of a reinforced concrete slab specimen because it shows the three stages of slab behavior:

1. Un-cracked stage where the slab behaves in the linear elastic mode;
2. Cracked stage where the behavior becomes increasingly nonlinear up to the point of peak load;
3. Post – failure stage where the residual strength and ductility of the slab can be observed in the descending branch.

The gradient of the load – deflection curve is indicative of the type of failure experienced in the slab. The gradient of the curve prior to failure is steep for slabs experiencing punching shear and more gradual for slabs failing in a flexural mode.

A limitation of the CDP model is the inability to model the post peak response of the load – deflection curve. The load-deflection data yielded from a plasticity model using visco-plastic regularization does not terminate at the point of punching shear failure. It was observed during this study that the response does show a characteristic peak followed by a descending branch which levels off or gradually begins to incline again. This is characteristic of a plasticity-based model where the plastic potential surface is crossed and the material increases in strain with little to no change in stress, also known as ideal plasticity. Ideal plasticity is not a realistic physical state of the actual behavior of concrete. Hence, the termination of the load – deflection data was

taken at the end of the descending branch before the inflection point where the curve flattens out and the concrete behaves 'plastic'. The ultimate punching shear load is defined as the peak of the load – deflection curve.

## Chapter 5

# Proposed Finite Element Model

The FEA model will be calibrated to the work by [18], [19], and [20]. The model will examine and develop a tension stiffening expression to account for the effect of the following parameters on the response of concrete slabs in punching shear:

1. Concrete compressive strength
2. Flexural reinforcement ratio
3. Inclusion of steel fibers
4. Flexural reinforcement yield strength

### 5.1 Concrete Compressive Strength Parameter

The literature review showed that an increase in shear resistance is proportional to an increase in concrete compressive strength. This section will focus on developing a tension stress – strain expression to be used in a FEA model to represent the influence of compressive strength on punching shear behavior. The model will be calibrated with the experimental study conducted by Lee et al [20]. The details of their test specimens is provided in Chapter 3 of this thesis.

The relationship between punching shear capacity and concrete compressive strength from the experimental data in Lee et al [20] is illustrated in Figure 5-1. As expected, the graph trends upward showing that the punching load increases with increasing concrete strength. There appears to be an anomaly where the maximum load for the 35 MPa slab is less than that for the

30 MPa specimen. Nonetheless the discrepancy is not very large. The following procedure will detail the methodology used to calibrate the 30U slab specimen model and then used to calibrate model specimens 35U, 55U, and 65U.

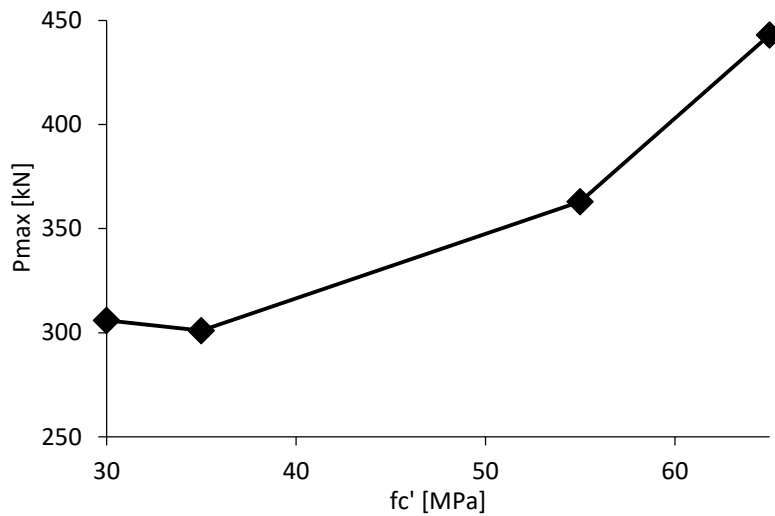


Figure 5-1: Experimental results for uniform slabs [20].

### 5.1.1 Modeling Concrete Behavior in Compression

As mentioned earlier, the concrete compressive strain relationship is adopted from Collins and Mitchell [25]. The compressive stress – strain curve for slab specimen 30U is illustrated in Figure 5-2.

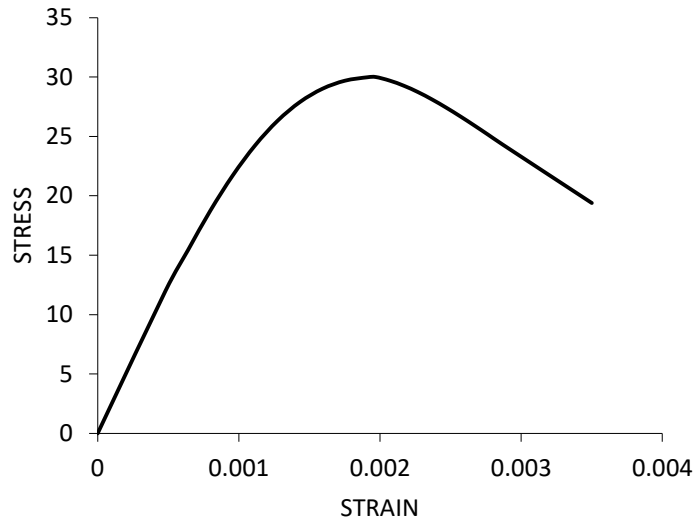


Figure 5-2: Specimen 30U FEA model compressive stress-strain diagram.

### 5.1.2 Modeling Concrete Behavior in Tension

The tension stiffening stress-strain relation is adopted and modified from Hsu and Mo [44] and given in Equation (2-10). The weakening function,  $n$ , given in the expression and the magnitude of the ultimate strain,  $\epsilon_u$ , are major contributing factors in the load-deflection response. As a starting point for both variables, Hsu & Mo [44] recommended to set  $n$  as 0.4 and Genikomsou & Polak [56] used a value for the ultimate strain to be approximately one-hundred times that of the cracking strain. The relationship between the ultimate strain and cracking strain will be represented in this thesis by an ultimate strain factor,  $\Upsilon$ . The corresponding tension stiffening curve is illustrated in Figure 5-3.

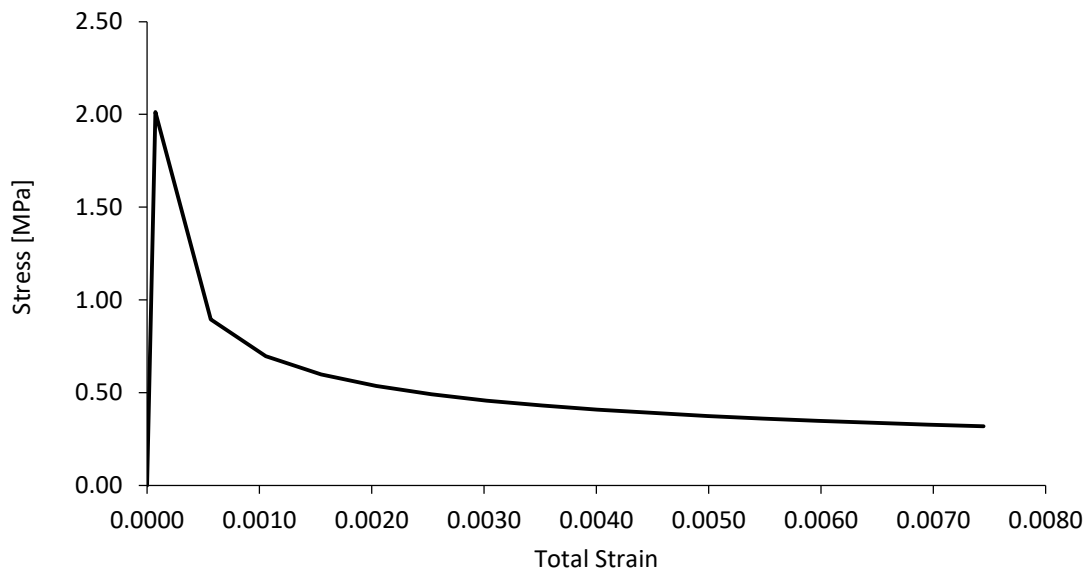


Figure 5-3: Reference slab 30U tension stress-strain diagram.

### 5.1.3 Results and Calibration

A range of values for  $n$  and  $\gamma$  were examined to study the influence of each variable on the load-displacement response. It is observed from Figure 5-4 that decreasing  $n$  causes an increase in the punching shear resistance. This is because a decrease in  $n$  increases the area under the stress-strain curve. The area under the stress strain curve represents the energy required to fail the concrete. An increase in area provides more energy absorption capacity so the slab can resist more punching shear stress. Similarly, Figure 5-5 shows that increasing  $\gamma$  also increases the punching shear resistance because it also increases the area under the stress-strain curve. Figure 5-6 shows that the curve with  $n$  equal to 0.4 and  $\gamma$  equal to 100 agree best with the experimental results. The ultimate punching shear load from the FEA simulation is 302 kN which is very close to the experimental load of 306kN. The initial stiffness, which is the slope of the ascending branch, also closely matched the experimental response. The initial elastic stiffness up to the

point of cracking, which is represented by the first inflection point on the descending portion of the curve, is slightly stiffer in the FEA model. This causes a slight uniform offset in the ascending branch which is typical of FEA simulation results. A plot of the stress contours of the slab specimen 30U FEA model show a distinct punching shear cone at the column support as would be expected (Figure 5-7).

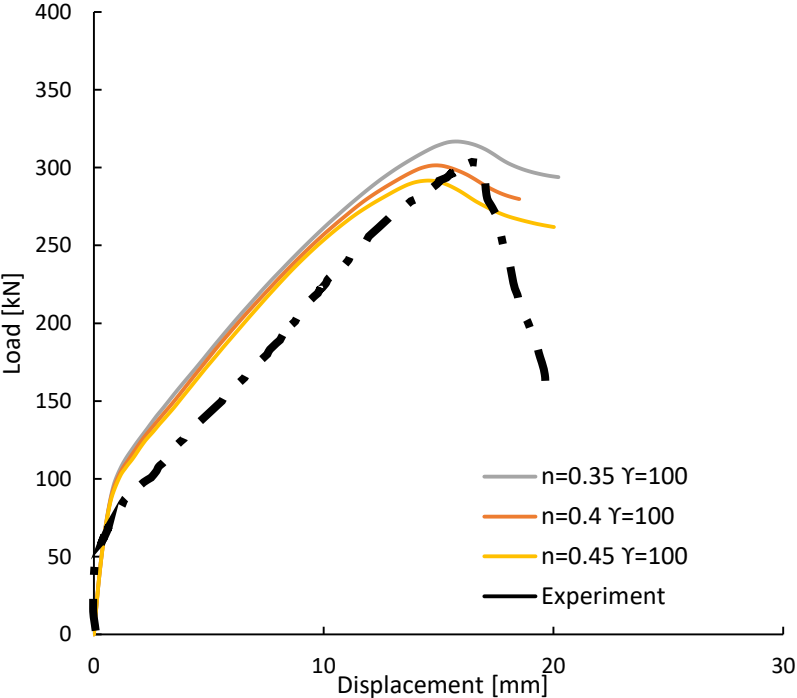


Figure 5-4: Load vs displacement for 30U – varying  $n$ .

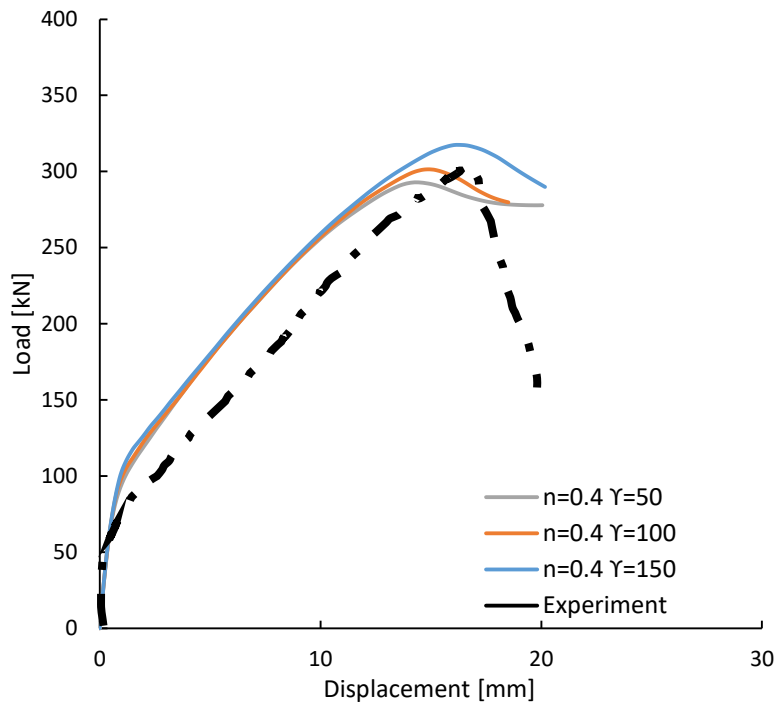


Figure 5-5: Load vs displacement for 30U – varying  $\gamma$ .

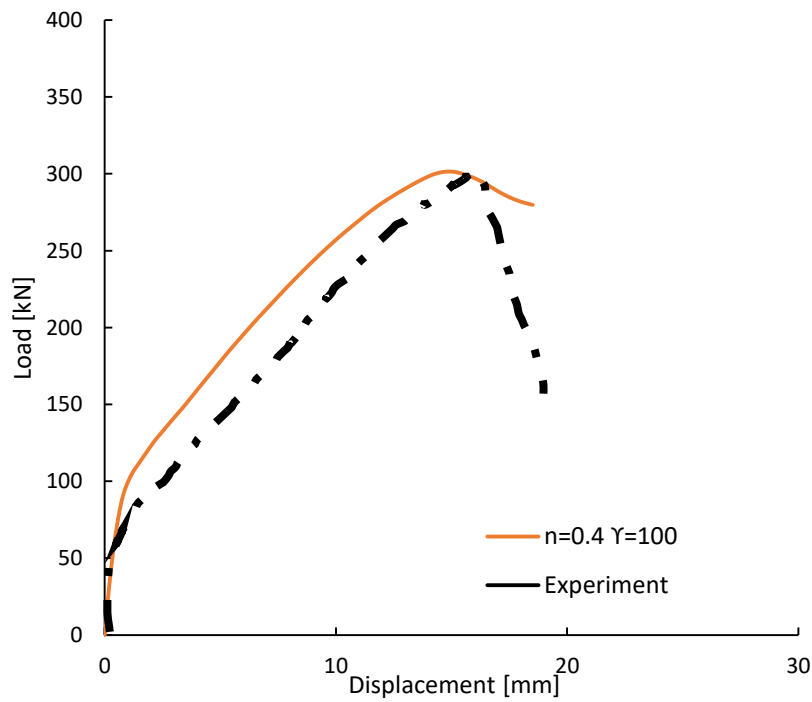


Figure 5-6: Calibrated load vs displacement for 30U.

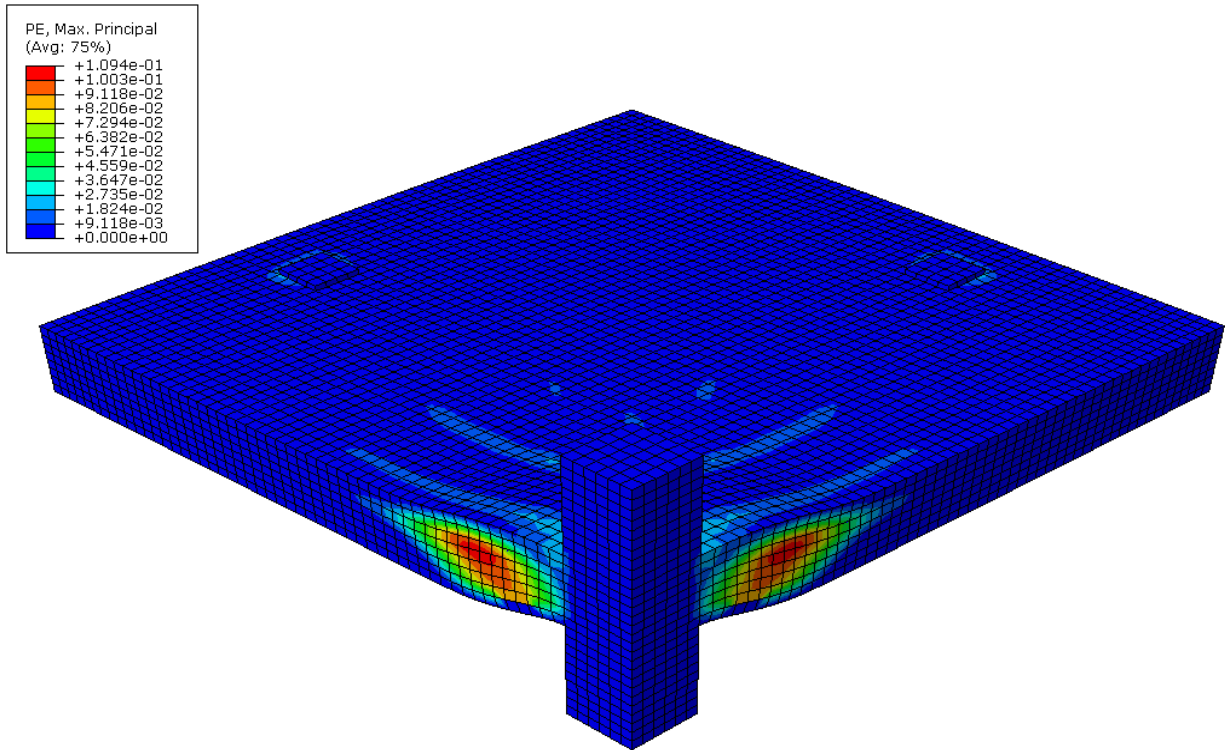


Figure 5-7: FEA stress contours for 30U.

Slab specimens 35U, 55U, and 65U were modeled using the same methodology as 30U described above. The weakening function and ultimate strain factor were varied until a matching pair converged to an acceptable solution. The load-displacement curves in Figure 5-8 to 5.10 correlate reasonably well with the experimental data. The slope of the ascending branches is similar to the experimental load-deflection curves and the peak loads are similar. A discrepancy is noted with specimen 35U where it was mentioned earlier that there could be an inconsistency in the experimental data. The comparison of the maximum load versus concrete strength from the FEA analysis and the experimental values are shown in Figure 5-11. The curve from the FEA results for 35U is more in line with the convention that punching shear increases as concrete strength increases.

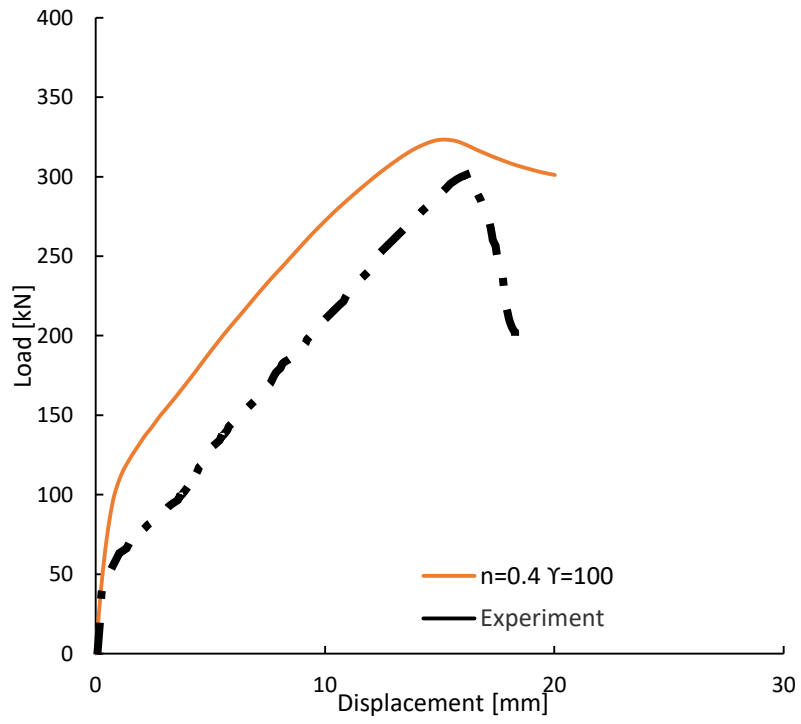


Figure 5-8: Load vs displacement for 35U.

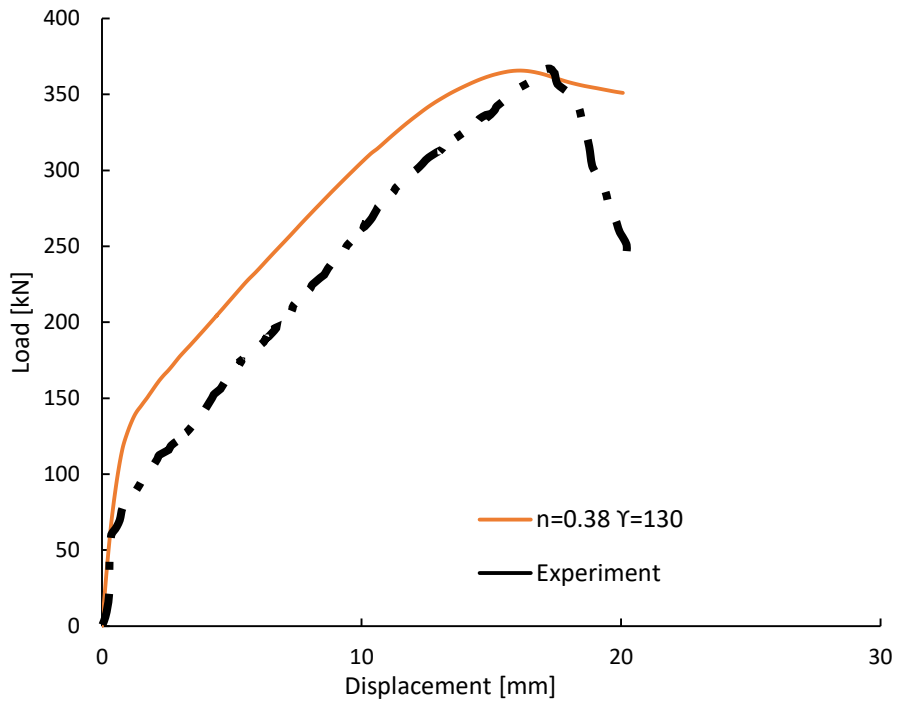


Figure 5-9: Load vs displacement for 55U.

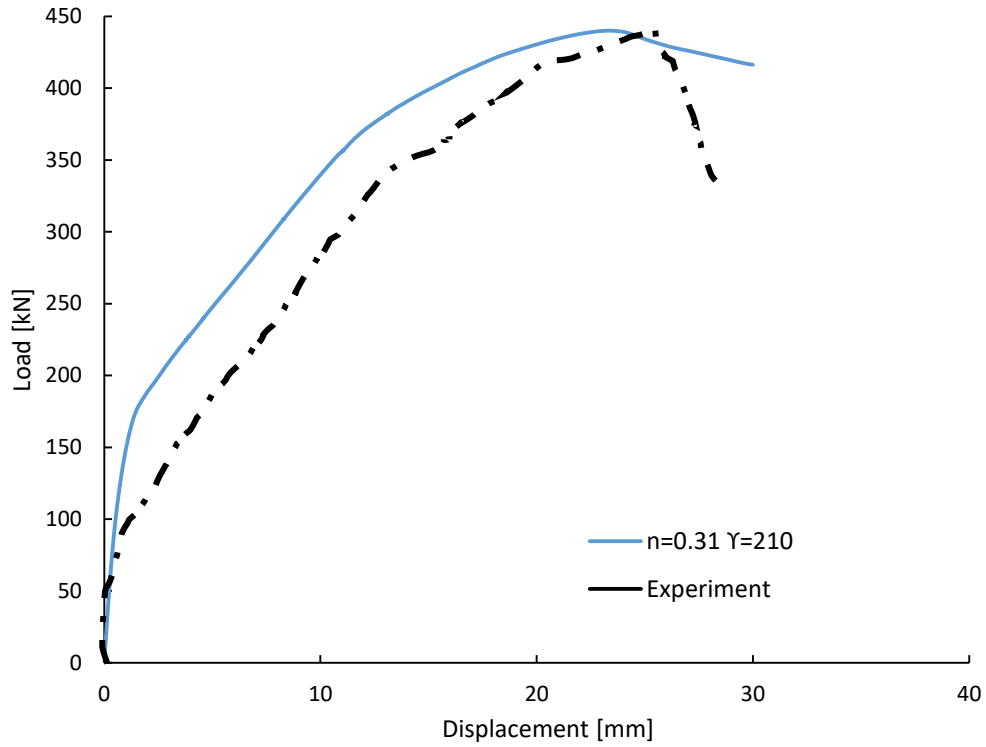


Figure 5-10: Load vs displacement for 65U.

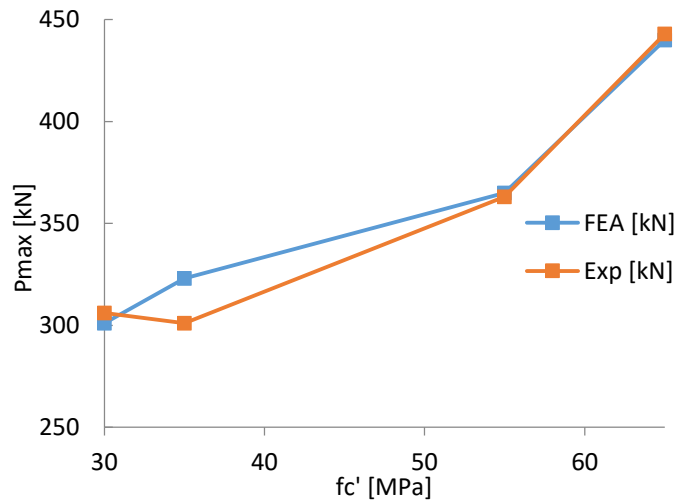


Figure 5-11: Comparison of FEA models vs experimental data for U-series slabs.

The values for  $n$  and  $Y$ , used in defining the tension stiffening curve for each model, when plotted together, reveal a relationship for both parameters as a function of the concrete

compressive strength. The decrease in  $n$  as a function of  $f'_c$  can be approximated by a linear regression line (Figure 5-12).

The ultimate strain factor,  $\gamma$ , remains constant up to a concrete strength of approximately 40 MPa. After that point,  $\gamma$  increases rapidly with respect to  $f'_c$ . This relationship is better approximated by a polynomial expression after 40 MPa to reflect the steeper increase in strain with higher strength concrete (Figure 5-13). The following functions can be used to define a tension stiffening curve to be used in a finite element analysis for punching shear when only considering variations in concrete compressive strength.

Weakening function,  $n$ :

$$n = A_n \quad (5-1)$$

Where;

$$A_n = 0.48 - 0.0023f'_c \quad (5-2)$$

Ultimate Strain Factor,  $\gamma$ :

$$\gamma = A_\gamma \quad (5-3)$$

Where;

$$A_\gamma = 100 \quad \text{if } f'_c \leq 40 \text{ MPa} \quad (5-4)$$

$$A_\gamma = (0.24f'_c{}^2 - 20.8f'_c + 548) \quad \text{if } f'_c > 40 \text{ MPa}$$

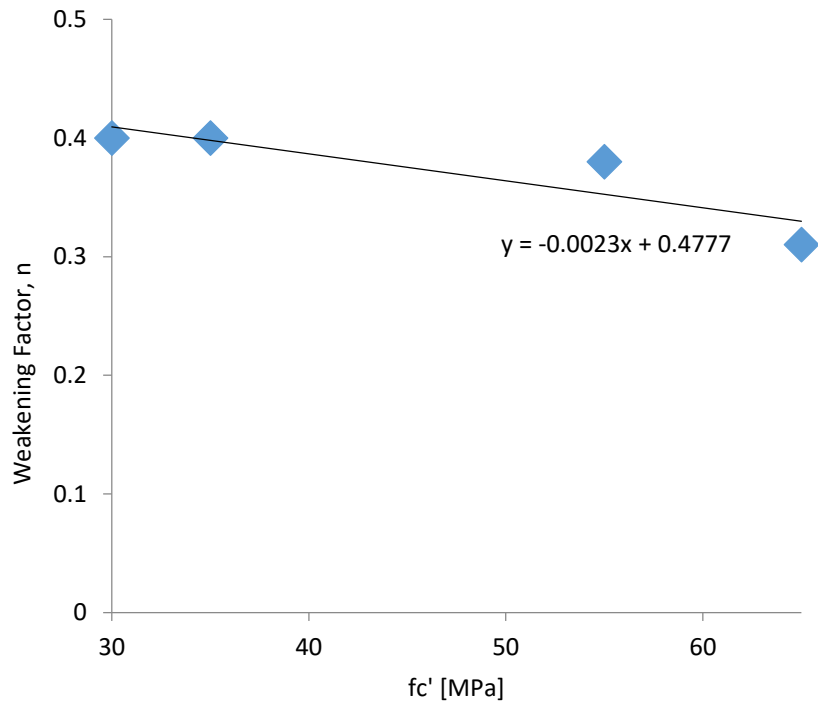


Figure 5-12: Weakening function,  $n$  vs concrete strength,  $f'_c$ .

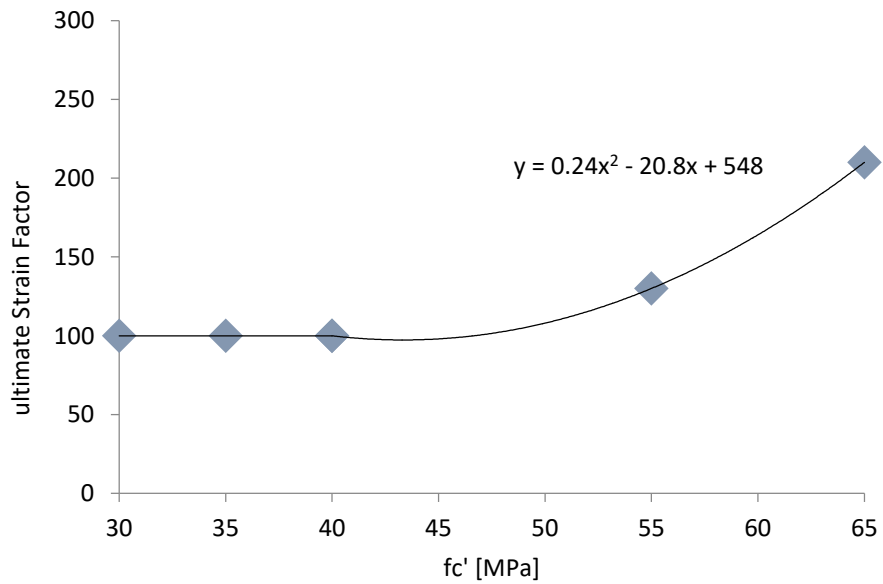


Figure 5-13: Ultimate strain factor vs concrete strength.

## 5.2 Flexural Reinforcement Ratio Parameter

The expressions for  $n$  and  $\gamma$  describing the tension-stiffening curve has so far been calibrated to only one value of flexural reinforcement ratio of 1.2% that was used in specimens 30U, 35U, 55U and 65U. The expressions in Equations (5-1) and (5-3) have to be expanded to account for the enhanced tension stiffening generated from the concentration of flexural reinforcement around the column zone. McHarg et al [19] and Lee et al [20] had demonstrated that doubling the flexural reinforcing ratio by concentrating the top mat of steel over the column zone resulted in a higher punching shear resistance and a higher post-cracking stiffness. It will be demonstrated that in an FEA model it is not sufficient to just increase the number of 2D steel reinforcing bars, but rather, it is also very important that the interaction of the steel and concrete be modeled as well. This interaction is simulated by adjusting the tensile stress-strain values to account for the tension-stiffening effect. To reinforce this point, Figure 5-14 shows the effect of applying the same tension stiffening properties used to model specimen 30U, in the previous section, to model slab specimen 30B [20] which has double the flexural reinforcing ratio. The resulting load-deflection curve, using  $n = 0.4$  and  $\gamma = 100$ , did not add enough tension stiffening to the slab and as a result the load-deflection response was well below the targeted curve from the experimental data of 30B. This shows that the Equations (5-1) and (5-3) must be re-calibrated for  $n$  and  $\gamma$  to reflect the change in the flexural reinforcement ratio parameter.

A range of values for  $n$  and  $\gamma$  were examined for slab specimen 30B and are displayed in Figure 5-15 and Figure 5-16. The calibration process yielded that in order for the FEA model to match the experimental results,  $n$  had to decrease to 0.3 and  $\gamma$  had to increase to 200. A similar process was conducted for slab specimens 35B, 55B, and 65B. The load-deflection curves for

these slabs, based on the calibrated values for  $n$  and  $\gamma$ , are given in Figure 5-17 to Figure 5-20. A comparison between the FEA and experimental punching shear loads are given in Figure 5-21. Similar to the uniform slab specimen 30U, there is an anomaly in the experimental results of specimen 35B. The punching shear loads for 55B and 65B are very similar to the experimental results. Again, as experienced in the U-series slabs, the initial ascending portion of the load-deflection curve performed stiffer in the FEA model than in the experimental results. This effect is typical for FEA analysis and experienced by other FEA researchers as well [56].

The relationship for the weakening function,  $n$ , between the banded reinforced slabs (B-series) and the uniform reinforced slabs (U-series) are related as a function of the reinforcement ratio as shown in Figure 5-22. The variable  $B_n$ , is chosen to represent the change in  $n$  with respect to a change in  $\rho$ .

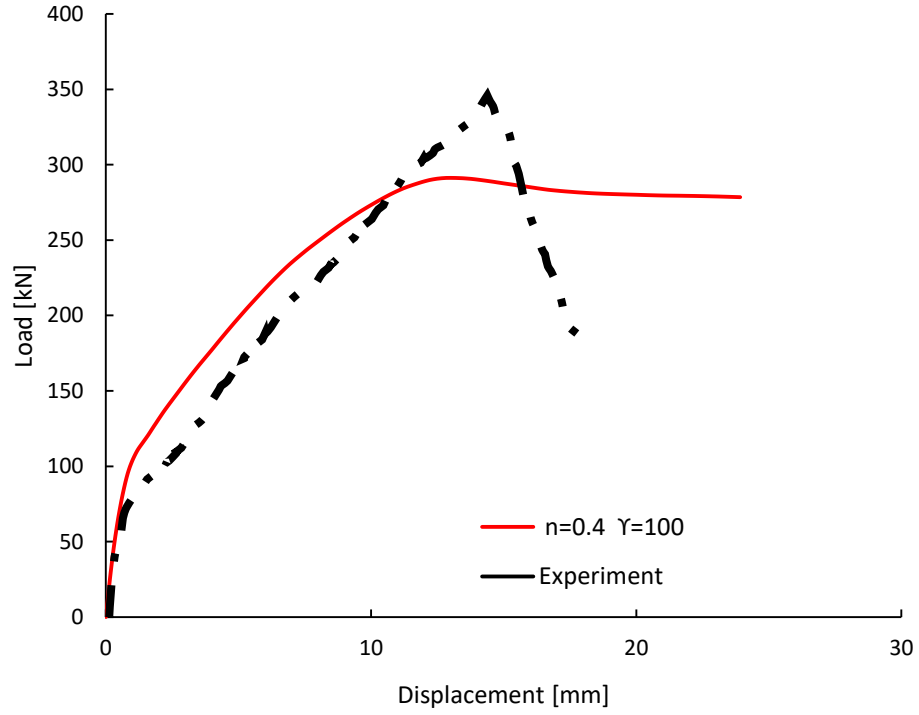


Figure 5-14: Load vs displacement for 30B using 30U parameters.

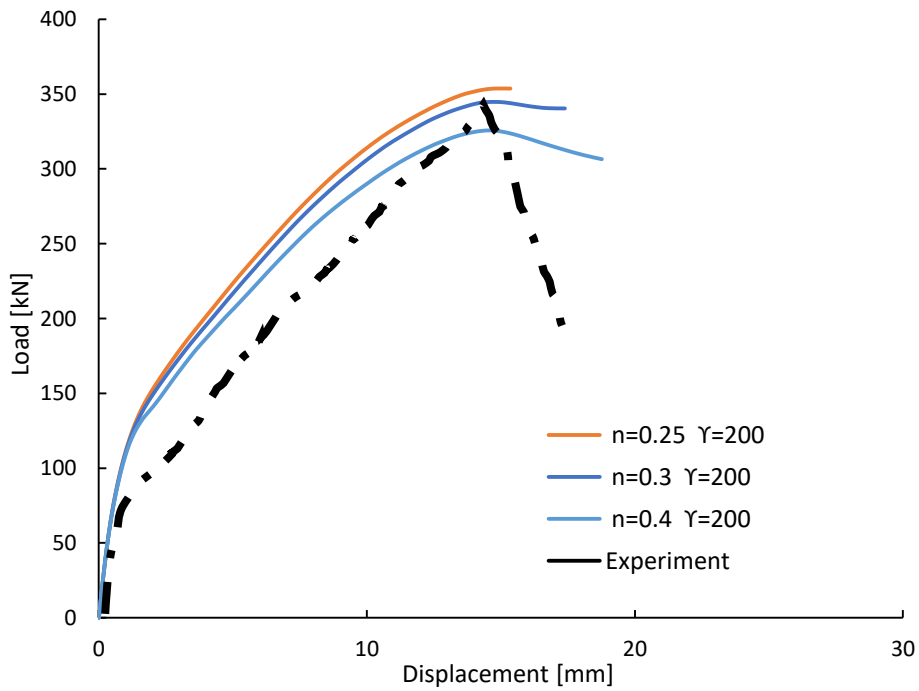


Figure 5-15: Load vs displacement for 30B – varying n.

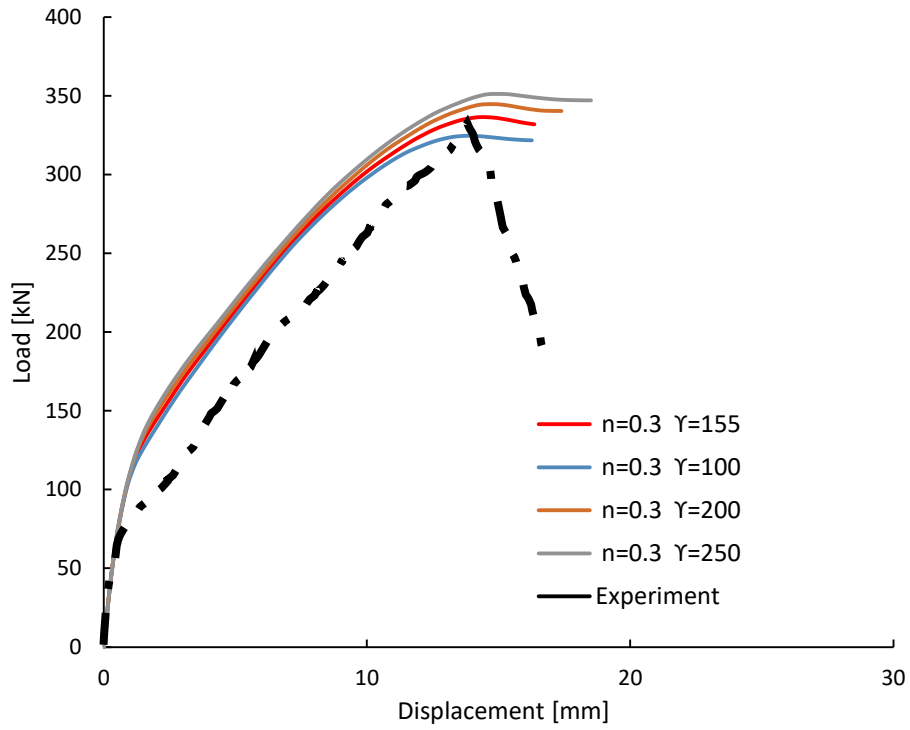


Figure 5-16: Load vs displacement for 30B – varying  $\gamma$ .

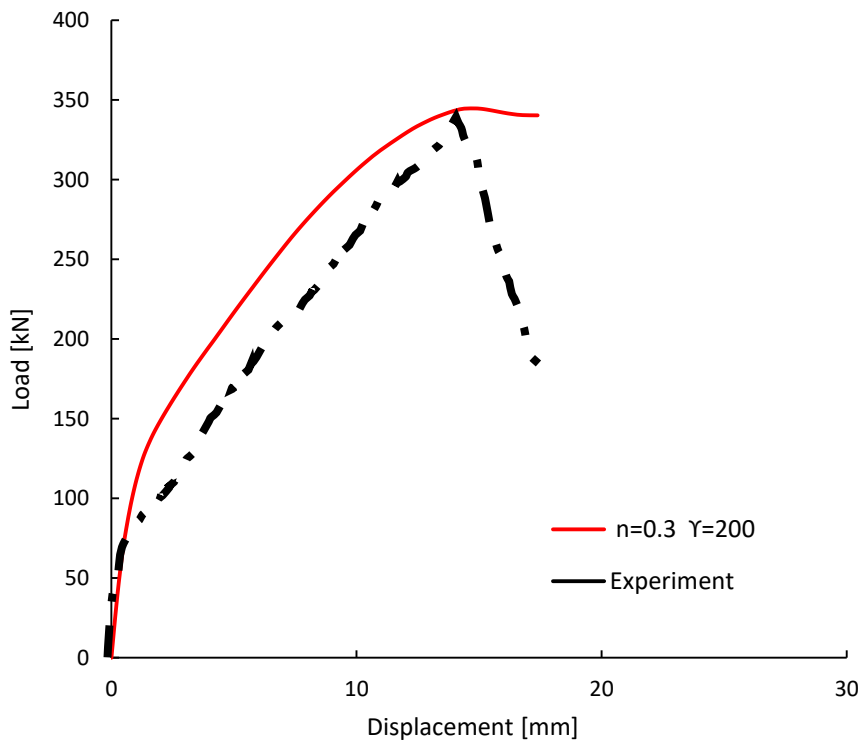


Figure 5-17: Load vs displacement for 30B.

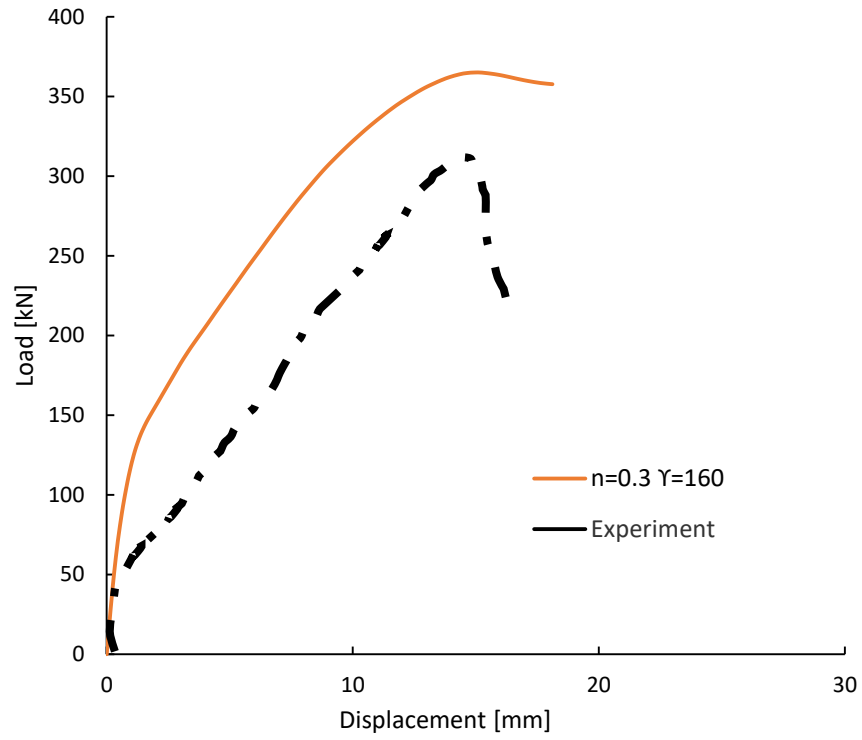


Figure 5-18: load vs displacement for 35B.

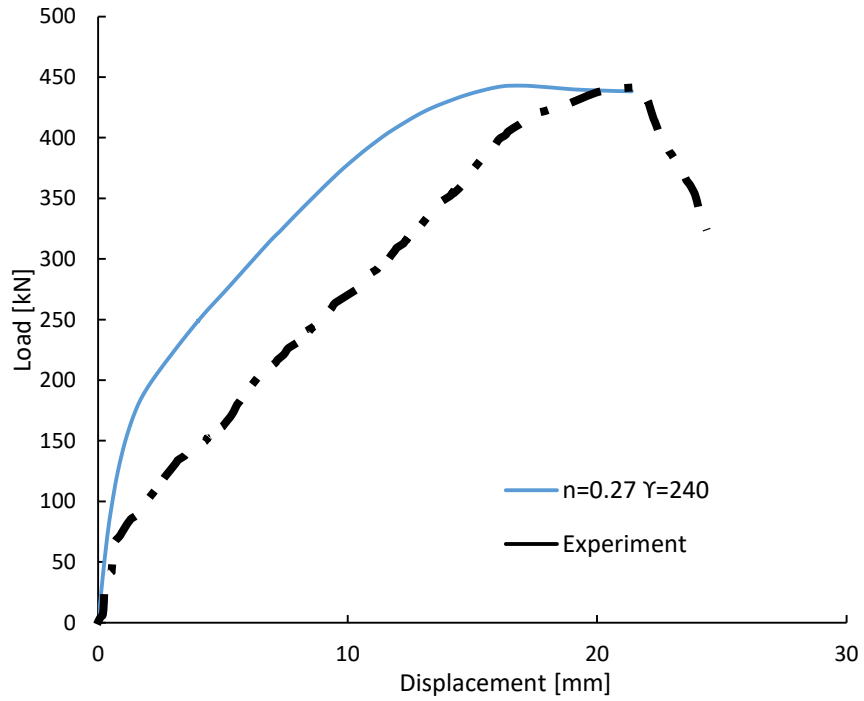


Figure 5-19: Load vs displacement for 55B.

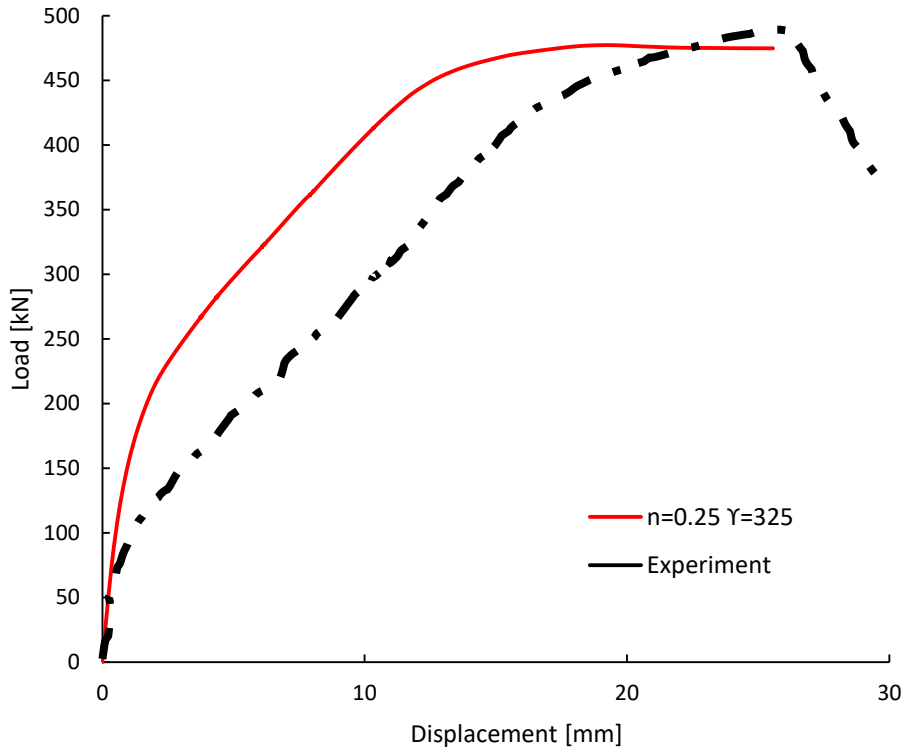


Figure 5-20: Load vs displacement for 65B.

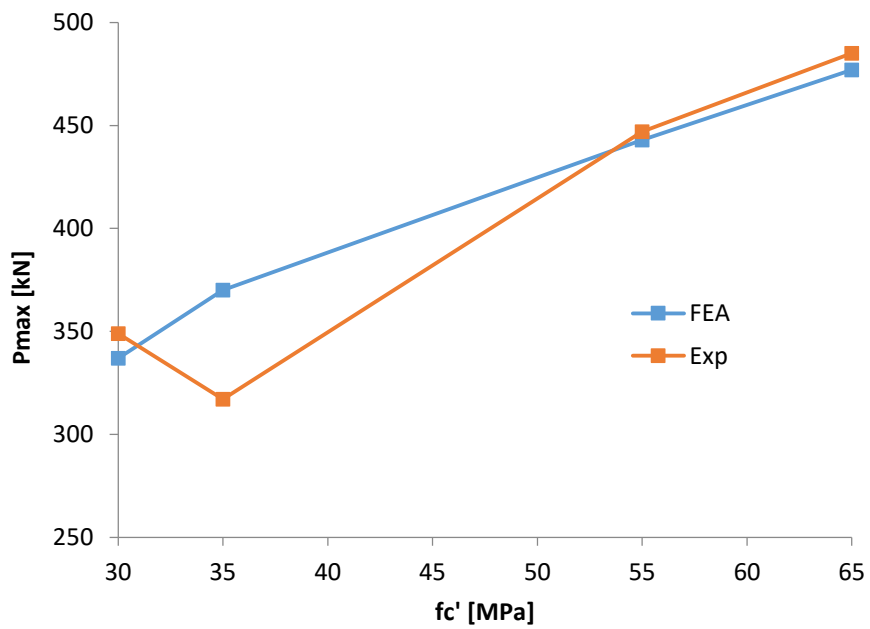


Figure 5-21: Comparison of FEA model vs experimental data for B-series slabs.

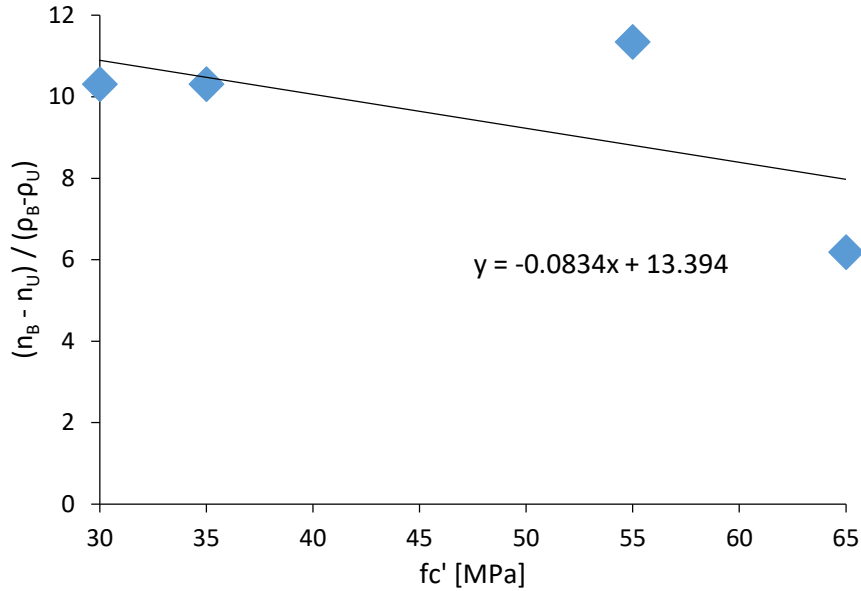


Figure 5-22: Relationship for 'n'.

The contribution of the reinforcement ratio to the weakening function is given as:

$$B_n = -[13.4 - 0.0834f'_c](\rho - 0.012) \quad (5-5)$$

Combining equation (5-5) with equation (5-1) for the contribution of the concrete strength yields the following expression for the weakening function:

$$n = A_n - B_n \quad (5-6)$$

Similarly, the relationship for the ultimate strain factor,  $\Upsilon$ , between the banded reinforced slabs (B-series) and the uniform reinforced slabs (U-series) are also related as a function of reinforcing ratio as shown in Figure 5-23. The variable  $B_\Upsilon$ , is chosen to represent the change in  $\Upsilon$  with respect to a change in  $\rho$ .

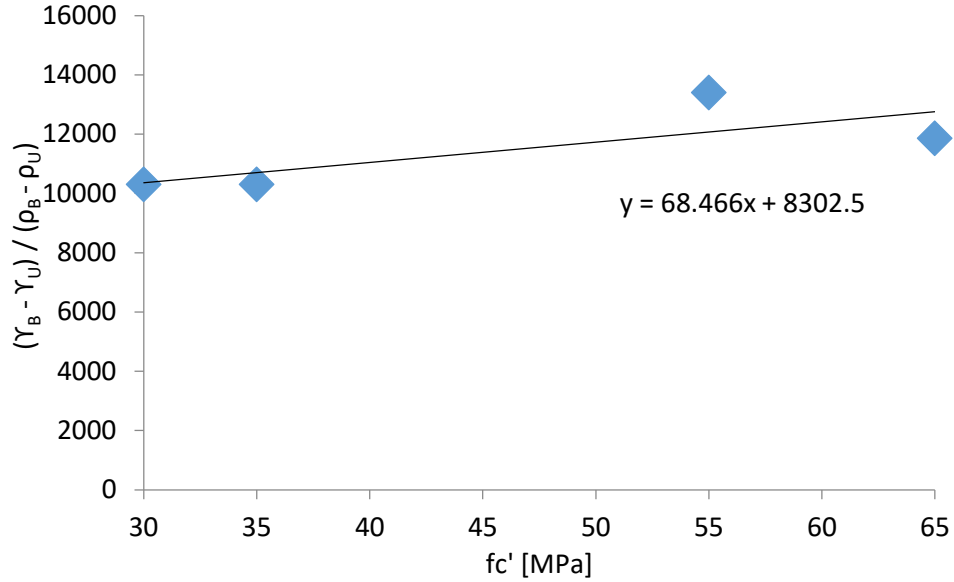


Figure 5-23: Relationship for ‘Y’.

The contribution of the reinforcement ratio to the ultimate strain factor is given as:

$$B_Y = [68f'_c + 8300](\rho - 0.012) \quad (5-7)$$

Combining the above formula with equation (5-3) for the contribution of the concrete strength yields the following expression for the ultimate strain factor:

$$\gamma = A_Y + B_Y \quad (5-8)$$

### 5.3 SFRC Fiber Volume Parameter

The enhanced tension stiffening properties of the concrete matrix in SFRC cause the shape of the load-displacement curve to differ from normal concrete as outlined in the literature review of this thesis. The tension-stiffening parameters  $n$  and  $\gamma$  should reflect the higher ductility and punching shear resistance caused by the addition of the steel fibers. A material model for

SFRC concentrated around the slab-column interface is proposed and calibrated using the work published by McHarg et al [19] for slab specimen FSU. A summary of the experimental program was presented in Chapter 3 of this thesis. The following sections will detail the procedure used to develop the tension-stiffening parameter for SFRC.

### 5.3.1 Modeling SFRC Behavior in Compression

For the normal reinforced concrete outside of the 500mm column zone, the concrete compressive strain relationship provided by Collins & Mitchell [25] was used. For SFRC, the compressive stress-strain curve as defined by Lee, Oh, & Cho [29] was adopted. The compressive stress-strain curves for both materials is presented in Figure 5-24.

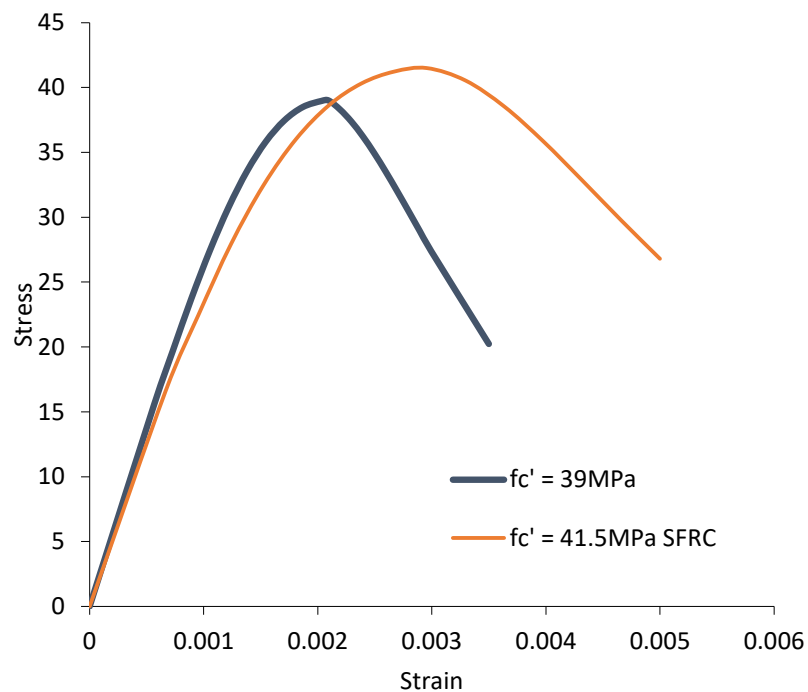


Figure 5-24: FEA slab FSU compressive stress-strain diagram.

### 5.3.2 Modeling SFRC Behavior in Tension

Equations (5-6) and (5-8) were used to determine the values for  $n$  and  $\gamma$  to be used in the tension stiffening expression. For the normal concrete portion of the slab  $n$  was calculated as 0.4 and  $\gamma$  was calculated as 100. The values of  $n$  and  $\gamma$  for the SFRC portion were determined through calibration with the experimental data of specimen FSU. The tensile stress-strain curve is given in Figure 5-25.

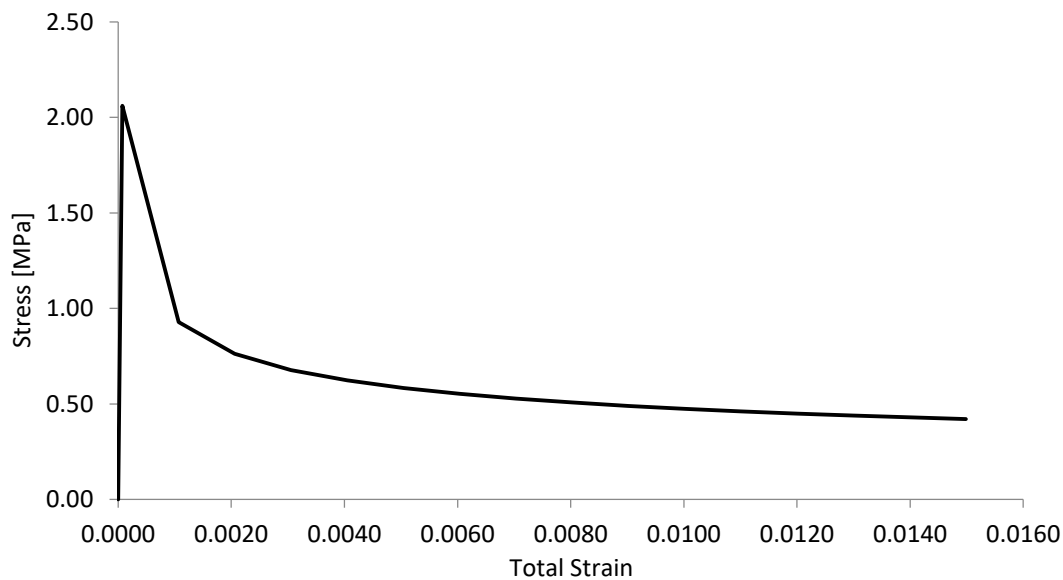


Figure 5-25: FEA slab FSU tension stress-strain diagram.

### 5.3.3 Results and Calibration

The load – deflection response using different values of  $n$  and  $\gamma$  for FSU are shown in Figure 5-26 and Figure 5-27. The combination values of  $n = 0.35$  and  $\gamma = 175$  correlated the best with the experimental results (Figure 5-26). The ultimate punching shear load from the simulation matched the experimental load and the slope of the ascending branch matched closely to the test data. Again, as observed in previous models, the initial elastic stiffness up to the point

of cracking was a bit stiffer in the FEA model causing a slight uniform offset in the ascending branch. The load – deflection curve shows that the FEA model does not exhibit as much ductility as the experimental response. The deflection at the peak load in the FEA model was only 27 mm as compared to 38 mm in the experiment. The iterations of  $n$  less than 0.35 and  $\gamma$  greater than 175, as displayed in the curves of Figure 5-27 and Figure 5-28, show that the FEA model could still not achieve the same ductility as the experiment while maintaining a similar ultimate punching shear resistance. The stress contours from the FEA model shown in Figure 5-29 clearly show the punching shear radiating from the column face and fanning out toward the tensile surface of the slab.

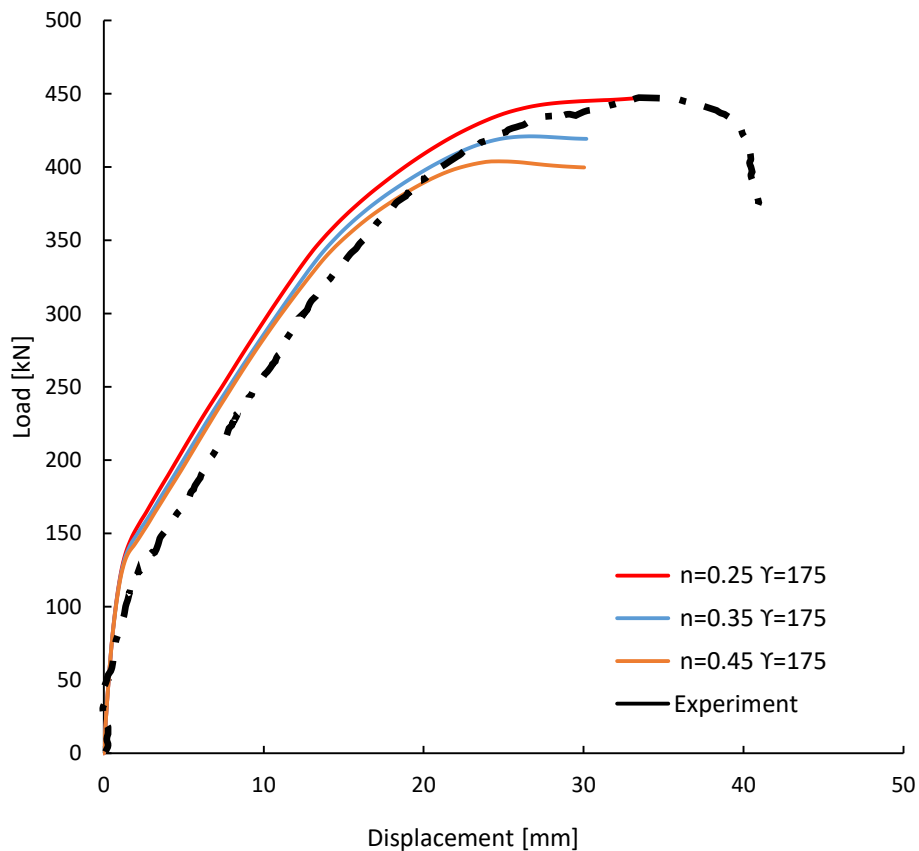


Figure 5-26: FSU Slab load vs displacement calibration for varying  $n$ .

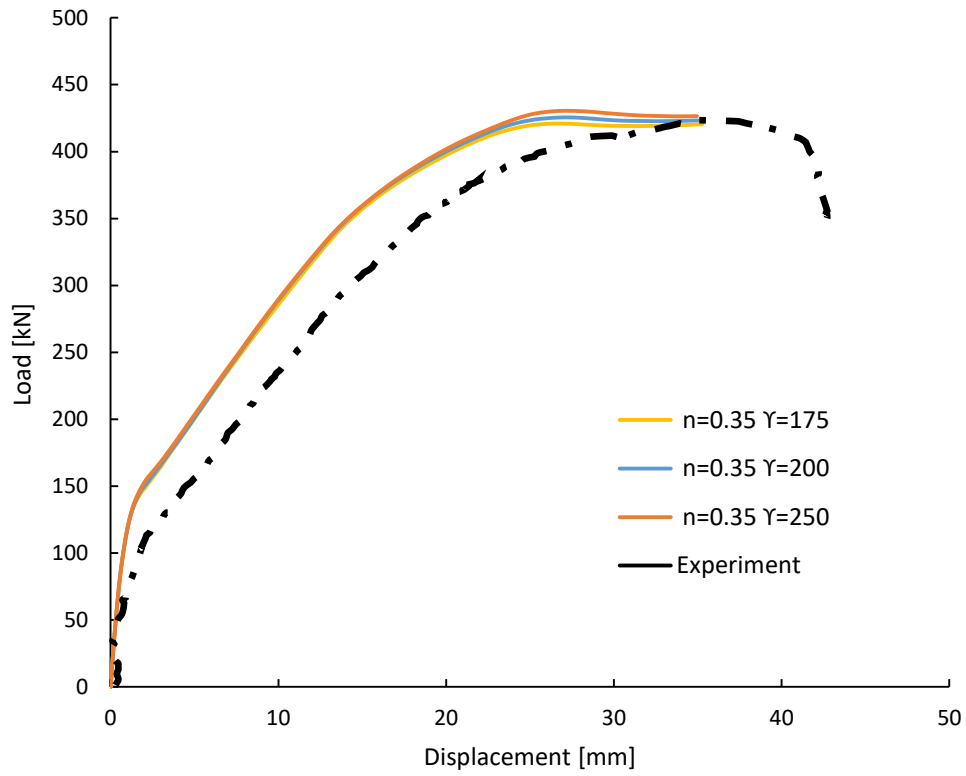


Figure 5-27: FSU load vs displacement calibration for varying  $\gamma$ .

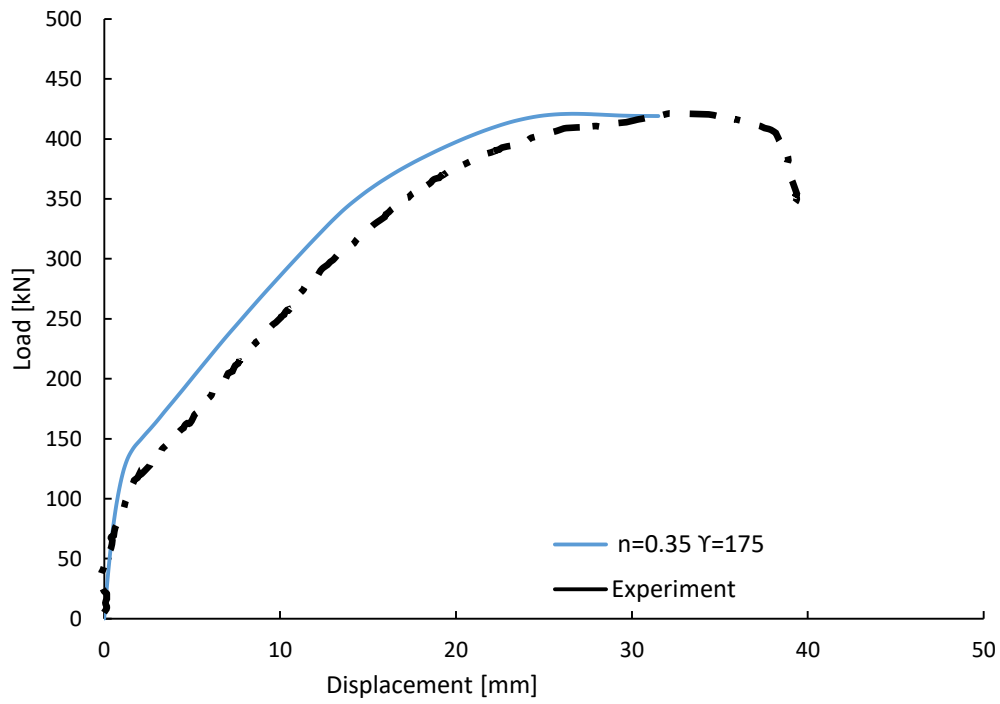


Figure 5-28: FSU load vs displacement.

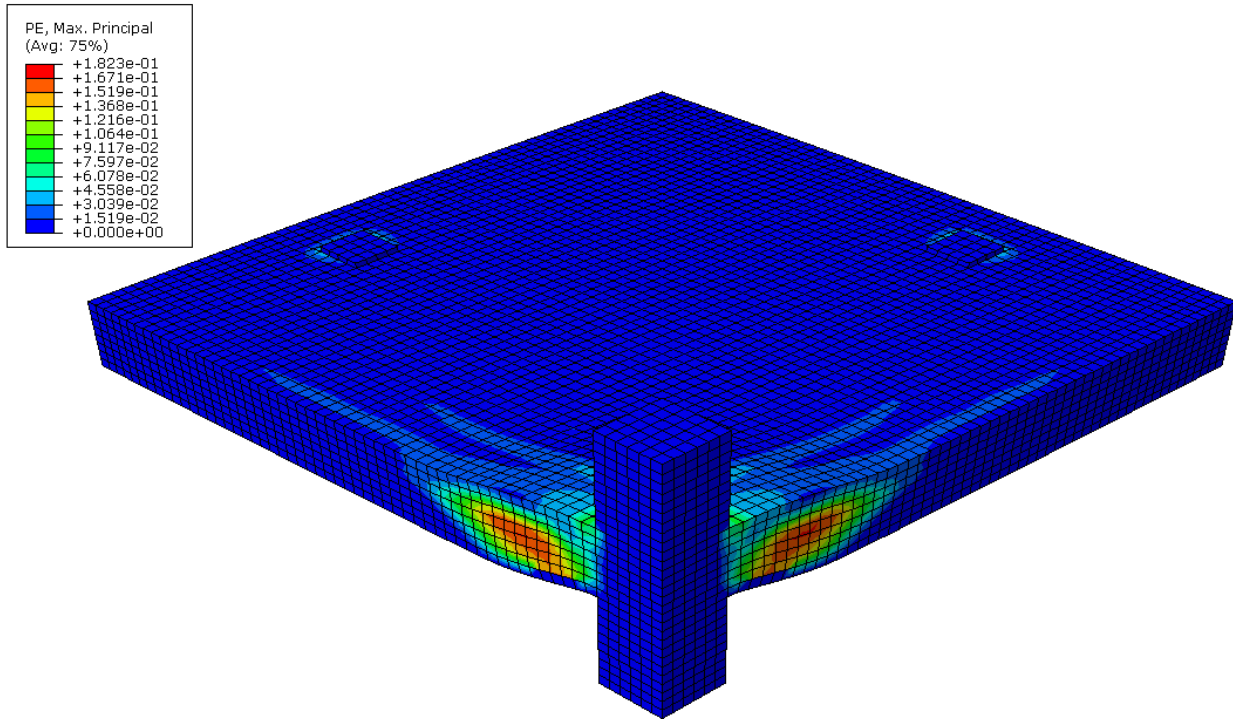


Figure 5-29: FEA stress contours for FSU.

The results from FSU show the enhanced tension stiffening provided by the addition of steel fibers to the concrete matrix. To determine the effect that the steel fibers had on the tension stiffening parameters, the results from FSU will be related to those from the expression developed from the U-series slab.

Using Equation (5-6),  $n$  for normal reinforced concrete with  $f'_c = 41.5$  MPa would be 0.384. The calibration process determined  $n$  for SFRC to be 0.35 which is 90% of the value calculated if  $n$  had been calculated for normal concrete. A new multiplier,  $C_n$  can be added to Equation (5-6) to account for SFRC. This new multiplier will recognize that for a fiber content of 0.5%,  $n$  decreased by a factor of 0.9. The new weakening function expression including the variable for SFRC will be:

$$n = (A_n - B_n)C_n \quad (5-9)$$

Where;

$$C_n = 1 - \frac{V_f}{5} \quad (5-10)$$

Where;  $V_f$  = fiber volume content (%)

Using Equation (5-8)  $\gamma$  for plain reinforced concrete with  $f'_c = 41.5$  MPa would be 100.

The calibration process determined  $\gamma$  for SFRC to be 175 which is 1.75 times the value calculated if  $\gamma$  had been calculated for normal concrete. A new multiplier,  $C_\gamma$  can be added to Equation (5-8) to account for SFRC. This new multiplier will recognize that for a fiber content of 0.5%  $\gamma$  increased by a factor of 1.75. The new ultimate tensile strain factor expression including the variable for SFRC will be:

$$\gamma = (A_\gamma + B_\gamma)C_\gamma \quad (5-11)$$

where;

$$C_\gamma = 1 + 1.5V_f \quad (5-12)$$

where;  $V_f$  = fiber volume content (%)

## 5.4 Flexural Reinforcement Yield Strength Parameter

Next, the tension stiffening parameters will be modified to include a factor to account for the flexural reinforcement yield strength. The model created so far was developed from slab specimens that all use the same conventional reinforcing steel that had a tested yield strength of approximately 455 MPa. The functions for  $n$  and  $\gamma$  expressing the tension stiffening behavior do

not have any provisions to account for the effect of punching shear resulting from a change in the strength of the steel bars. To incorporate this variable, a model for the punching shear behavior of slabs reinforced with high strength steel was calibrated to the work of Yang et al [18]. The test set-up was the same as all the previously analyzed slabs but the reinforcing used had a yield stress of approximately 800 MPa. The slab geometry, reinforcement, and load – deflection curves for [18] were presented in Chapter 3. The calibration of slab specimen MU1 will be used to modify the expressions previously derived for  $n$  and  $\gamma$  to account for the yield strength of reinforcing.

Slab MU1 had the same geometry, concrete material properties, and reinforcing layout as the previously tested slab 35U [29]. The only exception was that high strength reinforcing bars were used in lieu of conventional reinforcement. Testing of this slab revealed an ultimate punching shear load of 382 kN which was 18% greater than that for slab 35U demonstrating the increase in punching shear due to high strength bars. The reinforcement was modeled with the increased yield stress and the tension stiffening was adjusted through the weakening function and ultimate strain factor that were determined through calibration until the load – deflection curves correlated with the experimental data.

The previously developed expressions (5-9) and (5-11) for  $n$  and  $\gamma$  for the properties of specimen 35U [29] were used as a first trial to model specimen MU1 without including a term for the yield strength,  $f_y$ . The only difference in this run of the FEA model from that of specimen 35U was that the reinforcing was modeled with a higher yield strength (800 MPa). It is important to note that for this first trial the input for the concrete tensile properties did not acknowledge any effect of  $f_y$ . The purpose of this exercise is to study the effect on just modifying the rebar

elements in the model. The tension stiffening curve still maintained a value of  $n = 0.4$  and  $\gamma' = 100$  as used previously for 35U. The resulting FEA load-deflection curve for this trial of MU1 was well below the experimental data curve of MU1. As noted by Yang et al [18], the higher strength steel used in the experiment had produced a much higher punching shear response than 35U. However, since this first trial neglected any direct increase to the tension stiffening in the model the FEA response for MU1 was only consistent with that of 35U (Figure 5-30) and never displayed the increase in capacity as Yang et al [18] had experienced. Therefore in order model MU1 accurately, it is not sufficient to just increase the yield strength of the reinforcement in the model without increasing the amount of tensile stiffening. To realize the influence that higher strength steel has on punching shear, the tension stiffening model should be adjusted accordingly. To study this effect a little more in depth, the model was run using a low reinforcing steel yield strength of 200 MPa. At this yield strength, the load – deflection behavior was markedly different from that used for 35U which was 455 MPa and from that used in MU1 which was 800 MPa (Figure 5-31).

The amount of tension stiffening present in a concrete member affects the amount of stress resisted by the reinforcing steel because, as explained in the literature review, a part of the concrete assists in resisting tensile stress. When the specified tension stiffening is low, the stress transferred to the reinforcing also remains low and may not cause the steel reinforcing to yield. From Figure 5-31, the flexural reinforcing in the specimen with the yield strength of 200 MPa yielded and lowered its punching shear capacity.

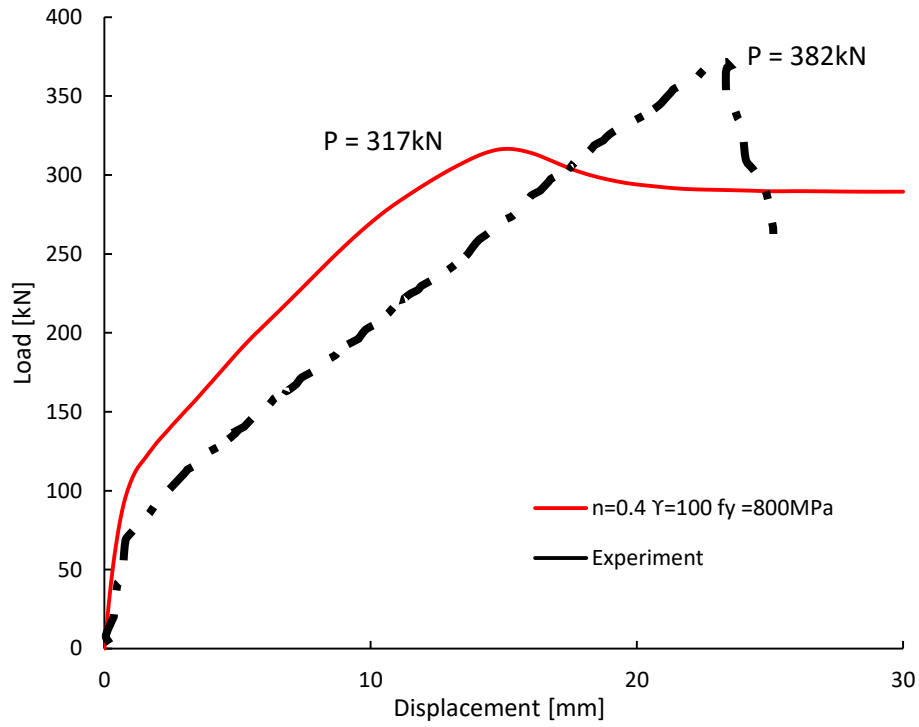


Figure 5-30: MU1 load vs displacement for  $n=0.4$ ,  $Y=100$ .

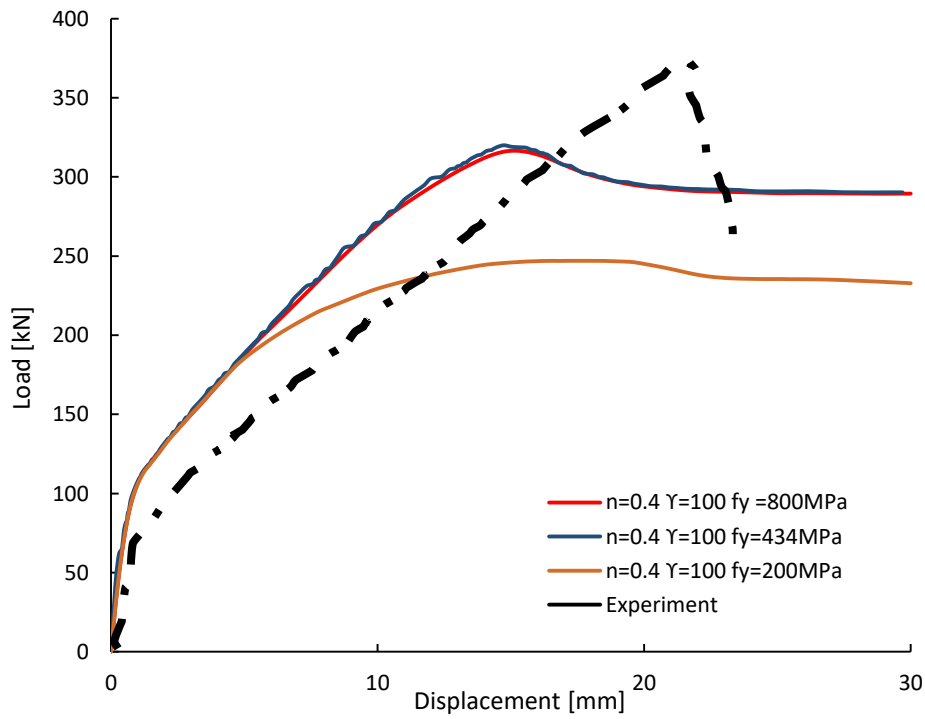


Figure 5-31: Influence on varying  $f_y$ .

To ensure that the yield strength was incorporated into the tension stiffening equation, the parameters,  $n$  and  $\gamma$  were adjusted until they converged on an acceptable fit with the test data. From (Figure 5-32) the values that met this criterion were  $n = 0.3$  and  $\gamma = 300$ . Using these parameters caused the load-deflection behavior for MU1 to be much greater than that for 35U.

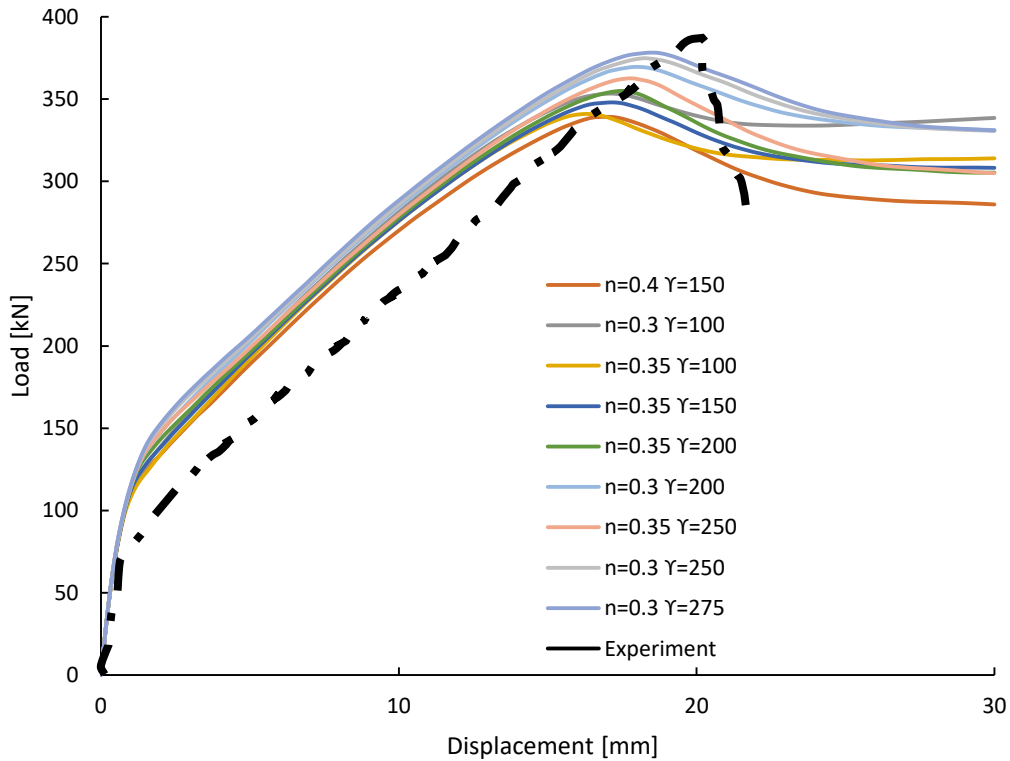


Figure 5-32: FEA MU1 load – deflection calibration.

The tension stiffening formula for the parameter  $n$  can now be modified to include a term,  $D_n$ , to account for the tension stiffening effect from the reinforcing steel yield strength.

The previously derived expression for  $n$ , was developed for a yield strength of 455 MPa. A more conventional yield strength for reinforcing steel is 400 MPa, therefore, the formula will be expressed as a function of a yield strength of 400 MPa. For this  $D_n$  will take the form of:

$$D_n = \varphi \frac{f_y}{400} \quad (5-13)$$

where;  $\varphi$  is a multiplier to account for the increase in tension stiffening with an increase in yield strength. For a reinforcement yield strength value of 455MPa,  $D_n$  would have to equal unity, for  $n$  to equal 0.4 and would for a reinforcement yield strength value of 800MPa,  $D_n$  would have to equal 0.75 for  $n$  to equal 0.3. From Equation (5-13)  $\varphi$  would equal 0.9 for 455 MPa and  $\varphi$  would equal 0.34 for 800 MPa. The following linear relationship is derived for  $\varphi$  as shown in Figure 5-33:

$$\varphi = 1.64 - 0.0016f_y \quad (5-14)$$

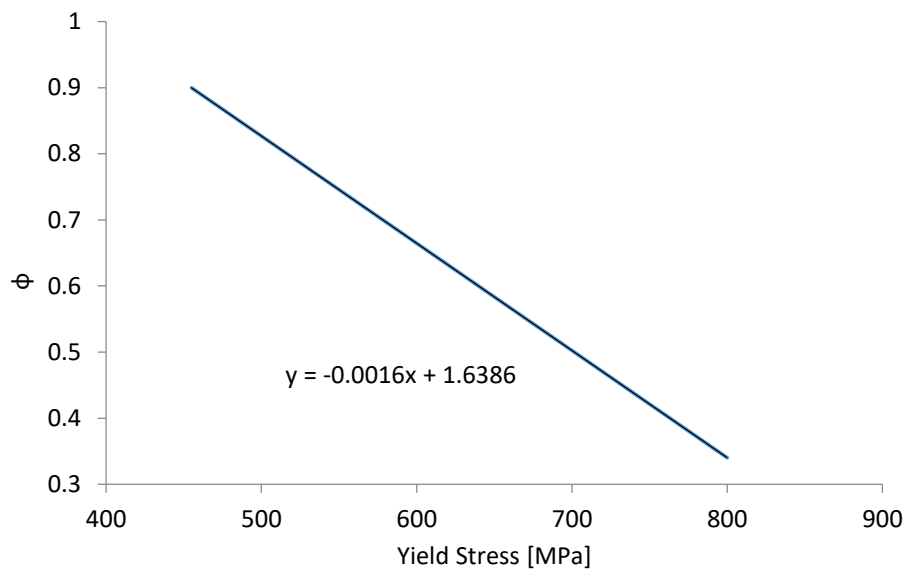


Figure 5-33:  $f_y$  calibration curve for  $n$ .

The calibration process for specimen MU1 saw  $\gamma$  increase by a magnitude of three, going from 100 to 300, when  $f_y$  changed from 455 MPa to 800 MPa. The expression for  $\gamma$  as a function of yield strength will be given by the variable  $D_\gamma$  and will take the form:

$$D_Y = \zeta \frac{f_y}{400} \quad (5-15)$$

Solving  $\phi$  at for yeild stresses 455 MPa and 800 MPa and gives values of 0.9 and 1.67 respectively. A plot of  $\zeta$  versus  $f_y$  in Figure 5-34 gives the following linear relationship:

$$\zeta = 0.0022f_y - 0.12 \quad (5-16)$$

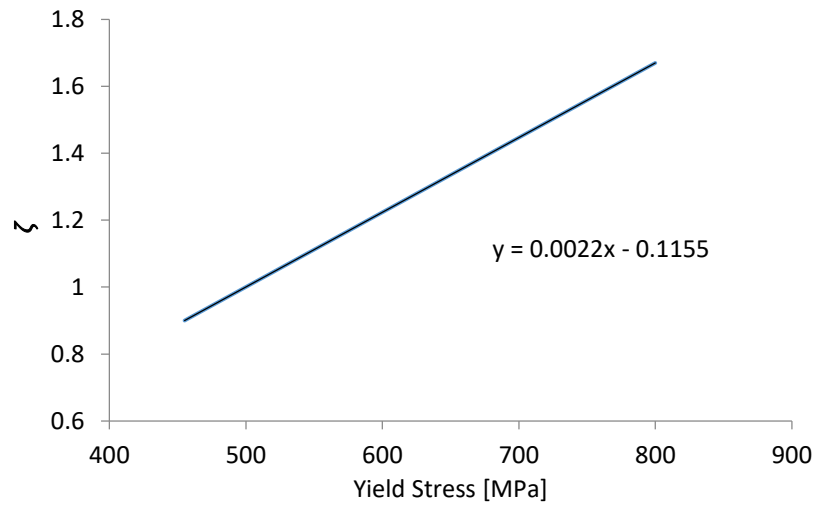


Figure 5-34:  $f_y$  variable calibration curve for  $Y$ .

The tension stiffening model has now been defined to account for a variation in the yield stress of the flexural reinforcement.

## 5.5 Tension-Stiffening Model Summary

The derived tension stiffening stress-strain relation yielded from this study is summarized below:

$$\sigma_t = E_c \varepsilon_t \quad \text{if } \varepsilon_t \leq \varepsilon_{cr} \quad (5-17)$$

$$\sigma_t = f_t \left( \frac{\varepsilon_{cr}}{\varepsilon_t} \right)^n \quad \text{if } \varepsilon_U > \varepsilon_t > \varepsilon_{cr}$$

Where;  $f_t = \text{uni-axial tensile strength} = 0.33\sqrt{f'_c}$

$$\varepsilon_{cr} = \text{cracking strain} = \frac{f_t}{E_c}$$

$$\varepsilon_t = \text{tensile strain}$$

$$\varepsilon_U = \text{ultimate strain} = Y \varepsilon_{cr}$$

$$n = \text{weakening function} = [A_n - B_n] C_n D_n L_n \quad (5-18)$$

$$\text{Where; } A_n = 0.48 - 0.0023f_c'$$

$$B_n = [13.4 - 0.0834f_c'](\rho - 0.012)$$

$$C_n = 1 - \frac{V_f}{5}$$

$$D_n = (1.64 - 0.0016f_y) \frac{f_y}{400}$$

$$L_n = 0.665 - 0.14L_c$$

$$Y = \text{ultimate strain factor} = [A_Y + B_Y] C_Y D_Y \quad (5-19)$$

$$\text{Where; } A_Y = (0.24f_c'^2 - 20.8f_c' + 548) \geq 100$$

$$B_Y = (68f_c' + 8300)(\rho - 0.012)$$

$$C_Y = 1 + 3V_f$$

$$D_Y = (0.0022f_y - 0.12) \frac{f_y}{400}$$

## Chapter 6

# Finite Element Model Verification

The FEA model created in this thesis to describe the general punching shear behavior of flat slabs will be verified by a series of experimental data to confirm its robustness and applicability in modelling slabs with a range of values for the different punching shear parameters.

### 6.1 Specimen FSB

The tension stiffening parameters developed for SFRC will be examined and validated for the punching shear behavior for slab specimen FSB featured in [19]. Specimen FSB will test the model's ability to incorporate the combination of SFRC and a high reinforcement ratio. Using Equation (5-18),  $n$  is calculated as 0.261 and using Equation (5-19),  $\gamma$  is calculated as 361. The load-displacement response of the FSB finite element model is shown in Figure 6-1. The ultimate punching load from the FEA, 440 kN, matching the experimental value of 438 kN. The slope of the ascending branches were in good agreement and in keeping with the stiffer behaviour as observed in all other FEA models. The maximum mid-span deflection of the model was similar to the experimental value. It can be concluded from these results that the material model was successful in demonstrating the load-deflection behaviour of slab specimen FSB.

### 6.2 Specimen FCU

Experimental data for specimen FCU is available in [19]. This slab features the placement of SFRC in the top 40 mm layer of the slab and uses a uniform reinforcing

configuration. The material model was used to calculate the tension stiffening properties for the normal concrete portion of the slab and the SFRC portion. Table 6.1 summarizes the tension-stiffening properties used in the FCU slab. The resulting load-deflection curve correlated well with the experimental curve (Figure 6-2). The ultimate punching shear load and mid span deflection were a close match. The punching shear load was less than 3% less and the peak load deflection was only 3 mm less.

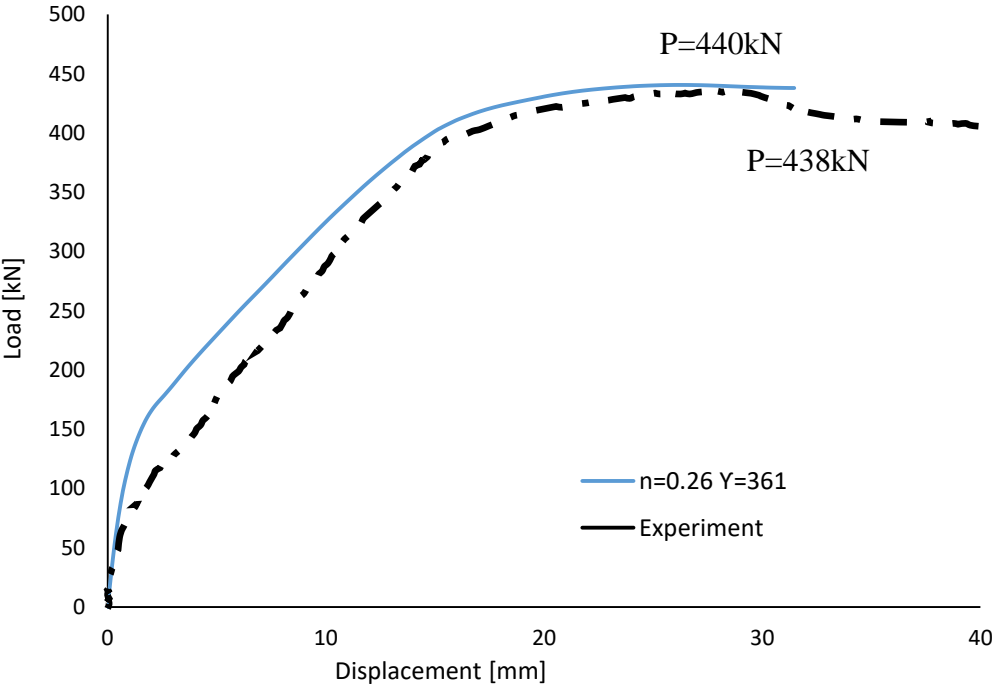


Figure 6-1: FSB load vs displacement validation.

Table 6.1: Tension Stiffening Properties FCU

| Material | n    | Y   |
|----------|------|-----|
| Concrete | 0.4  | 100 |
| SFRC     | 0.36 | 175 |

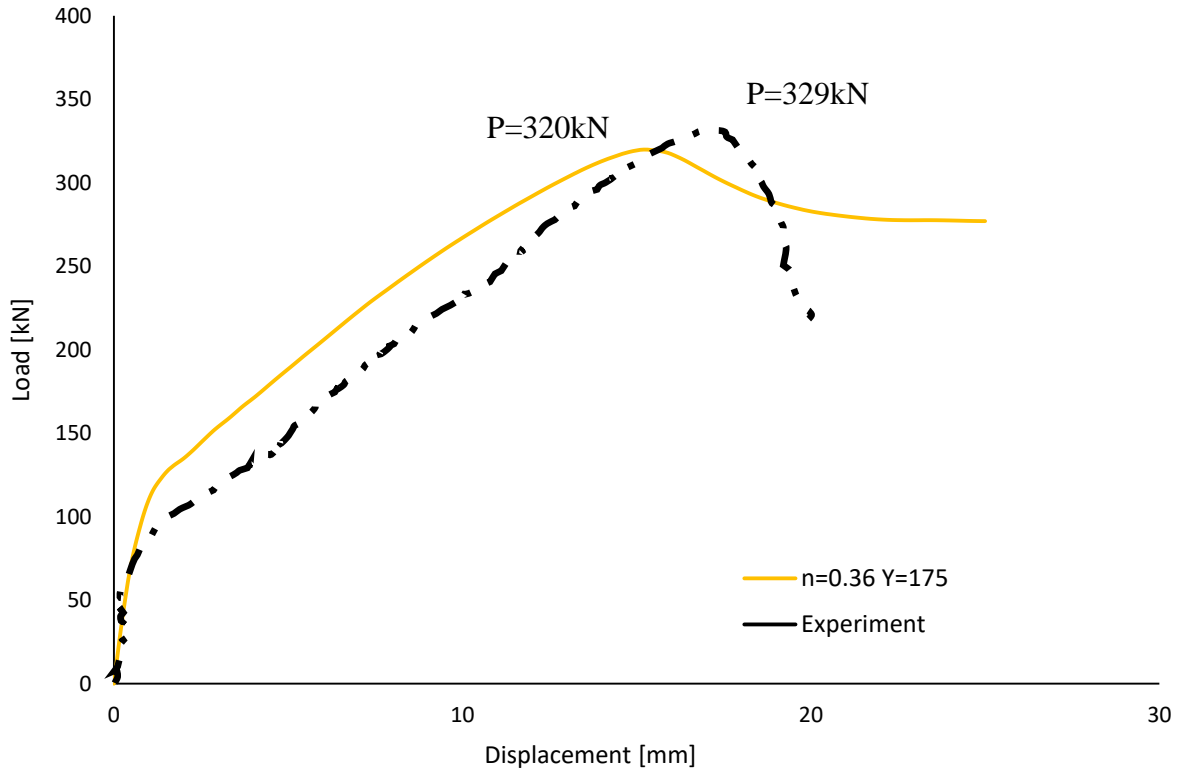


Figure 6-2: FEA Slab FCU load vs displacement.

### 6.3 Specimen FCB

Specimen FCB [19] was similar to FCU but used a higher reinforcement ratio concentrated over the column stub. Equations (5-18) and (5-19) were used to define the tension-stiffening curve. Table 6.2 summarizes the tension-stiffening properties used in the FCB slab. The resulting load-deflection curve again correlated very well with the experimental curve (Figure 6-3). The punching shear loads only differed by 2.8%.

Table 6.2: Tension Stiffening Properties FCB

| Material | n    | Y   |
|----------|------|-----|
| Concrete | 0.29 | 205 |
| SFRC     | 0.27 | 354 |

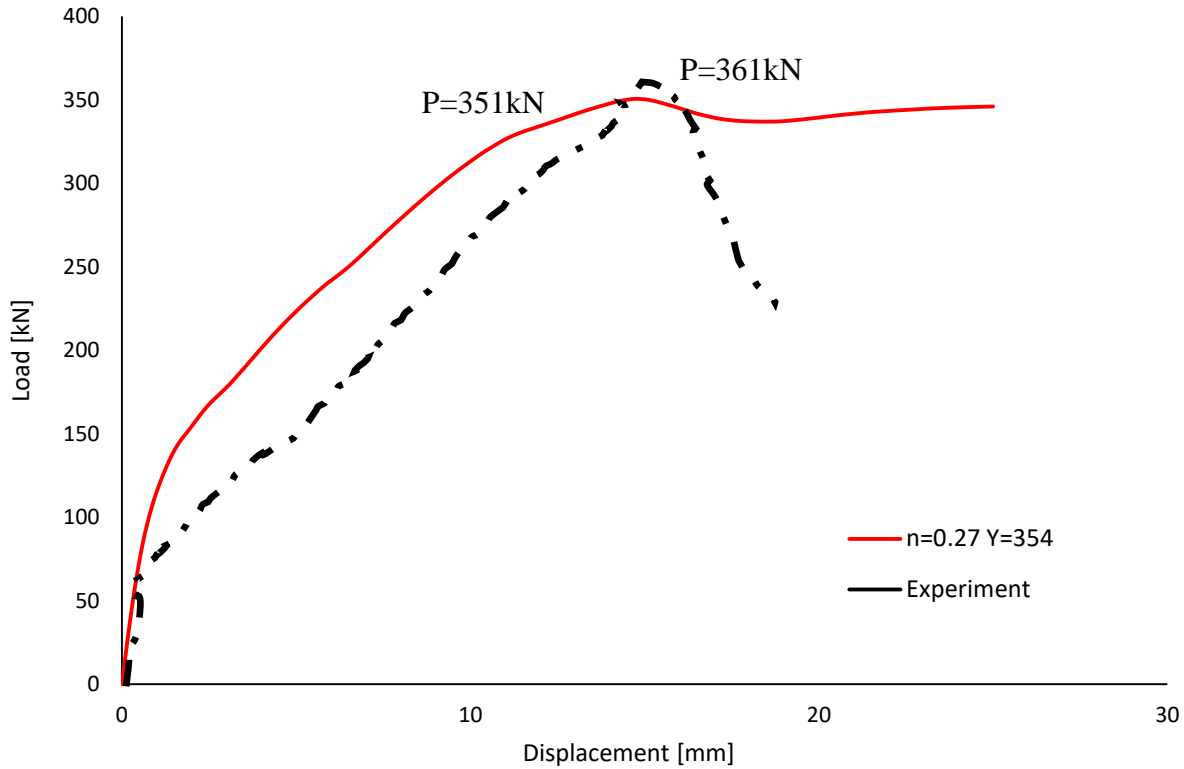


Figure 6-3: FEA Slab FCB load vs displacement.

## 6.4 Specimen 90BF

Experimental data for slab specimen 90BF was produced from the research by Lee et al [20]. Details of slab 90BF are provided in Chapter 3. This test will assess the model's ability to accurately simulate high strength concrete (92.1 MPa) with the inclusion of steel fibers and a high flexural reinforcing ratio. Due to the greater concrete strength and reinforcement ratio, the tension stiffening parameters for the SFRC portion of the slab calculated from Equations (5-18) and (5-19) are:  $n = 0.167$  and  $\gamma = 1536$ .

The load-displacement response of the 90BF model for the above parameters is shown in Figure 6-4. The ultimate punching shear stress and shape of the curve for the FEA model match fairly well with the experimental results. The percentage difference in the punching shear loads

was only 0.3% and the 6% in the peak load deflection. It can be concluded that the material model was successful in predicting the punching shear behavior of this slab.

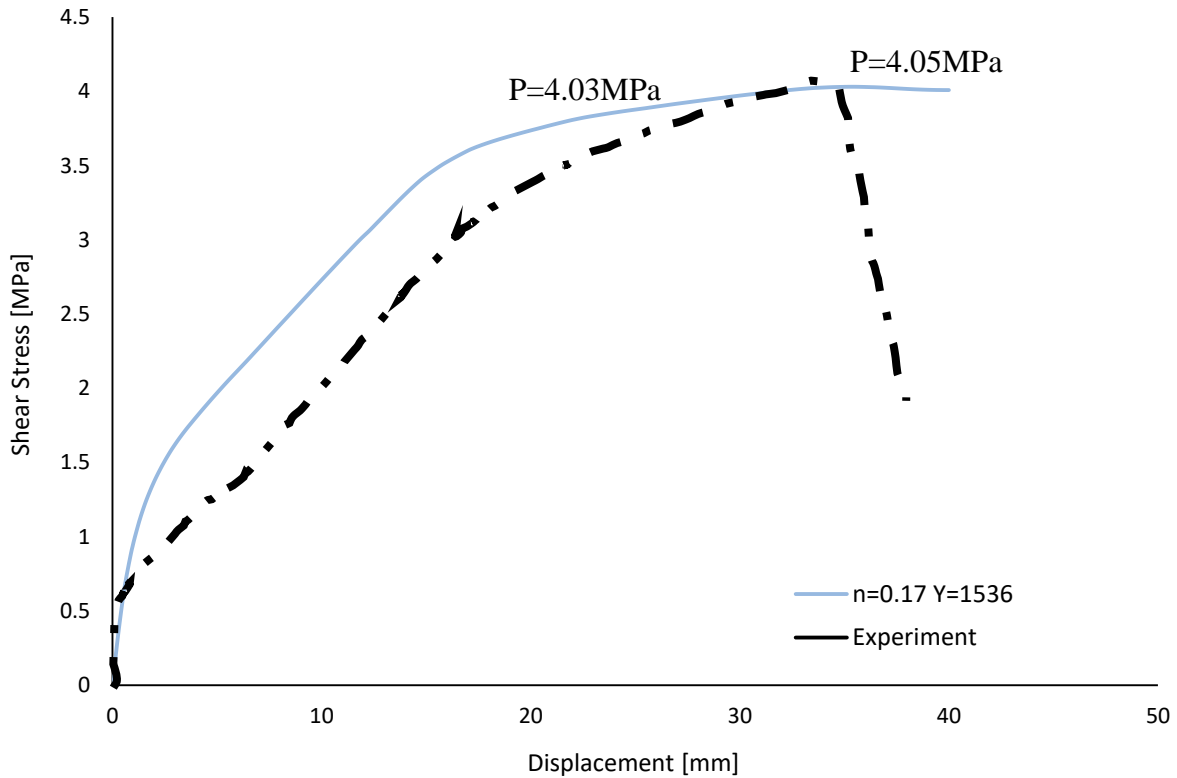


Figure 6-4: FEA Slab 90BF load vs displacement validation.

## 6.5 Specimen MU2

Slab MU2 [18] had all the same properties as specimen MU1 [18], which was used to calibrate the model, except the reinforcing bar size was reduced to No.13 ( $A_s = 129 \text{ mm}^2$ ) with high strength steel. The reinforcing spacing was chosen such that the slab exhibited the same flexural strength as slab specimen 35U [66]. Using  $f'_c = 35.3 \text{ MPa}$ ,  $\rho = 0.0064$ ,  $V_f = 0\%$ , and  $f_y = 800 \text{ MPa}$  the tension stiffening curve parameters from the derived from Equations (5-18) and

(5-19) are:  $n = 0.33$  and  $\gamma = 131$ . The load-deflection is plotted in Figure 6-5. The FEA model was slightly more ductile than the experimental curve but it did produce a similar ultimate punching shear load. In comparison to the FEA results of slab 35U, MU2 displays a smaller stiffness due to the smaller amount of flexural reinforcement. The authors reduced the bar size in MU2 to match the flexural strength of 35U since MU2 used higher strength steel. However, by doing that they greatly decreased the axial stiffness of the reinforcement. The difference in bar area would have reduced the reinforcing axial stiffness by approximately 45% which would cause the bars to stretch more, causing greater rotation of the slab and leading to lower punching shear values. That is why slab MU2 has less punching shear strength than its normal steel strength counterpart, specimen 35U.

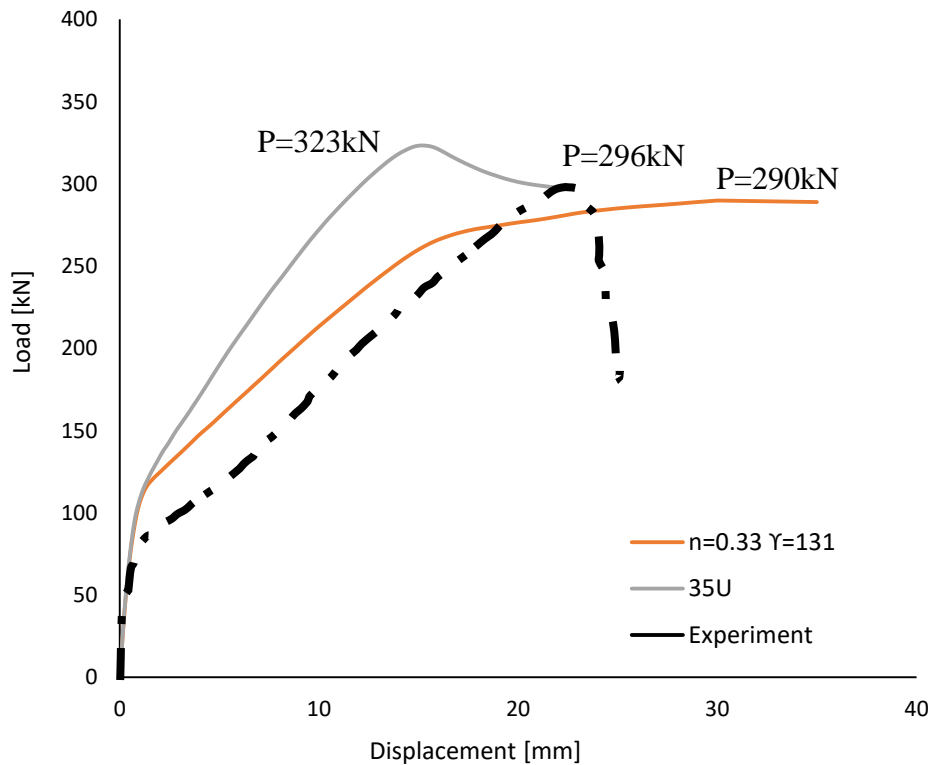


Figure 6-5: FEA Slab MU2 load vs displacement.

## 6.6 Specimen MB2

Specimen MB2 [18] was reinforced with No. 13 high strength bars like specimen MU2 [18] except that the reinforcing bars were banded together near the column. The reinforcement ratio in the band was 1.36% which is similar to MU1 ( $\rho=1.18\%$ ). It had been shown previously that slabs with a banded distribution of reinforcement have a higher punching shear strength than companion slabs with uniform reinforcing. The experimental results though show the opposite; the capacity of MU2 was higher than MB2. The authors contributed this irregularity to bond failure of the bars whereby the combined effect of closely spaced bars and the high strength over-stressed the concrete surrounding the bars and the bars subsequently de-bonded from the concrete. The authors proposed that this failure could be remedied with longer development lengths of the bars. The steel bar to concrete bond interaction is beyond the scope of this FEA model. Rather, this model assumes that the bars are properly detailed for development and assigns a 'perfect' bond between the two elements. Therefore, the results of this model show the load-deflection results that Yang et al. would have experienced if their slab did not fail prematurely from bond distress.

Using the tension stiffening parameter Equations (5-18) and (5-19),  $n = 0.28$  and  $Y = 384$ . The resulting load-deflection curve is shown in Figure 6-6. The FEA result was significantly higher than the experimental data as expected since the experiment failed prematurely due to bond distress. Also, as expected, the ultimate punching load for MB2 was higher than its uniform-reinforced counterpart MU2.

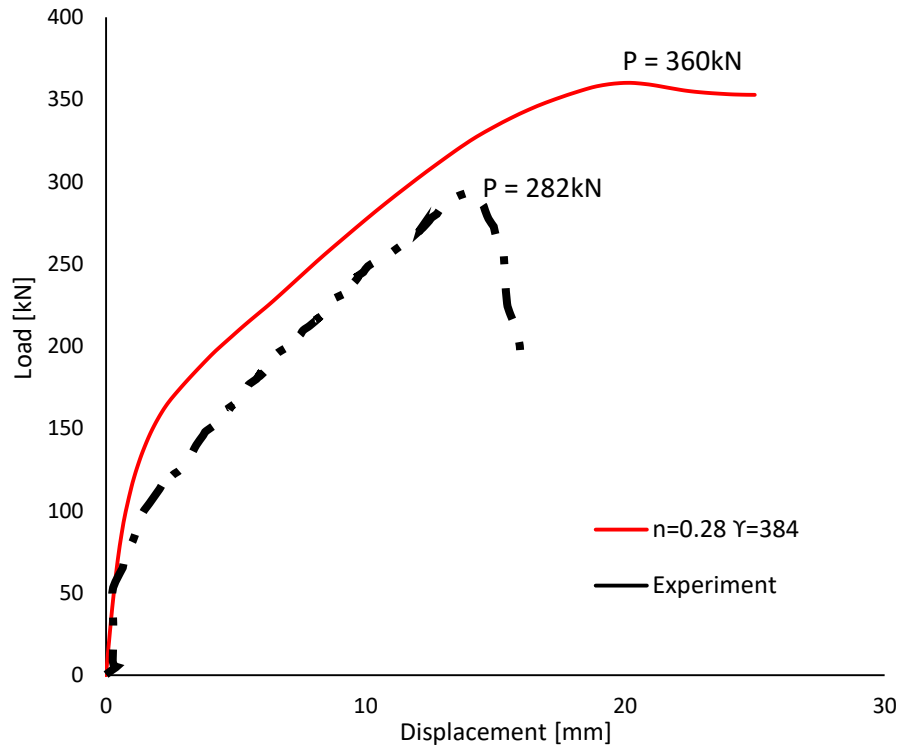


Figure 6-6 FEA Slab MB2 load vs displacement.

## 6.7 Specimen MBF2

Specimen MBF2 [18] was the same as MB2 but there was a concentration of 31 MPa SFRC ( $V_f = 0.5\%$ ) at a distance of 500 mm from the face of the column. In the experiment, the SFRC was successful in raising the punching shear load by 51% from slab MB2.

Using the tension stiffening parameter expressions, the  $n$  and  $Y$  values for the normal reinforced concrete portion were the same as MB2 and the values for the SFRC portion around the column were calculated as  $n = 0.25$  and  $Y = 672$ . The resulting load-deflection curve is shown in Figure 6-7. The ultimate punching shear load and maximum displacement were very close to that of the experiment. The tension stiffening model was accurate in predicting the result

of this slab specimen which included steel fibers, high reinforcing ratio, and high strength steel reinforcement.

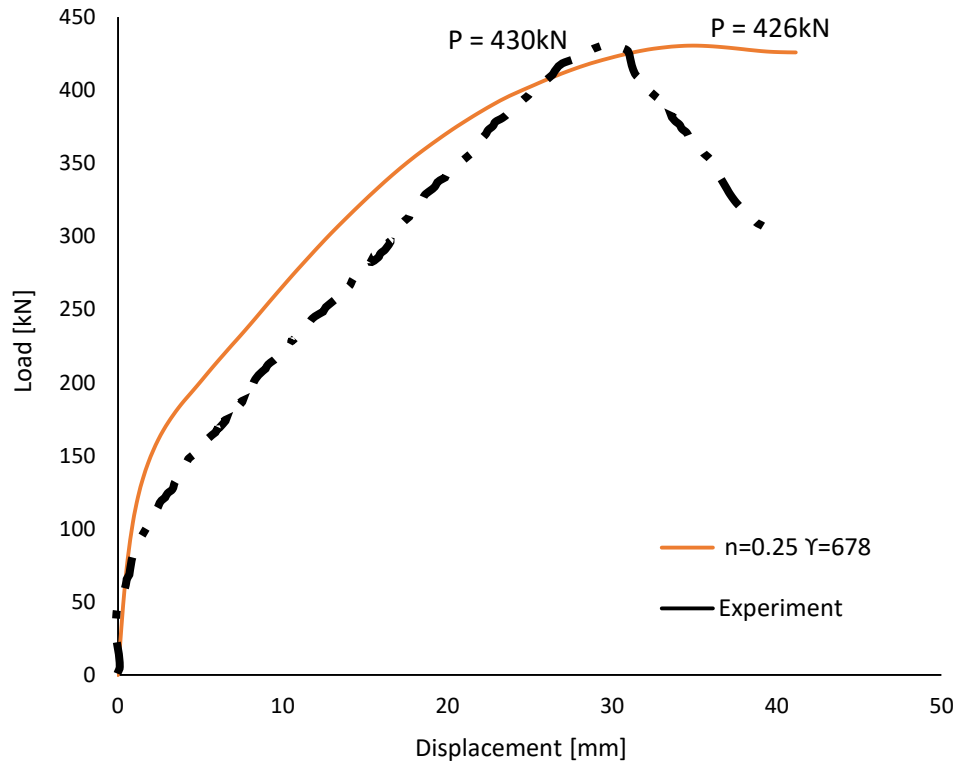


Figure 6-7: FEA Slab MBF2 load vs displacement.

## 6.8 Specimen SB1

Slab specimen SB1 was described in [56] and summarized in the literature review of this thesis. To recap it is 120 mm thick with 44 MPa concrete and a tensile reinforcement ratio of 1.1%. The weakening function,  $n$ , can be calculated from Equation (5-18) to be 0.39. The ultimate strain factor,  $\gamma$ , was calculated from Equation (5-19) to be 91. This slab was chosen for verification because it is outside of the experimental program of the three papers that the model was calibrated to and the experimental set-up for this model is different. All previous slabs featured the same set-up where the slab was supported on the column stub and pulled downward

at concentrated points along the edge. Specimen SB1 is roller supported along the edges and loaded through the column stub.

Specimen SB1 was modeled by Genikomsou & Polak [56]. The authors based their FEA model on a fracture energy approach and converted the crack opening displacements into a tensile strains. The tensile stress versus strain curve developed in this thesis through Equations (5-18) and (5-19) is compared with the curve developed by Genikomsou & Polak [56] (Figure 6-8). The area under the curves is a close match and hence the load-displacement curve yielded from the FEA models are closely aligned. The FEA models produced in this thesis is a fairly close match to the experimental data for SB1. The difference in punching shear loads is less than 10% and the peak load deflection is only 3 mm greater (Figure 6-9).

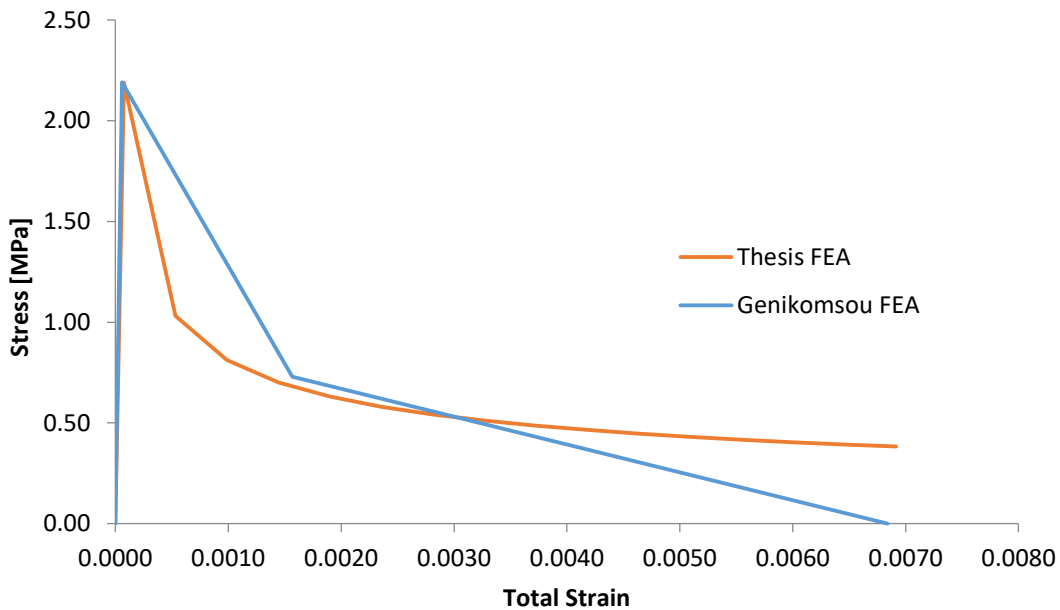


Figure 6-8: Comparison of FEA tension stress-strain curves for SB1.

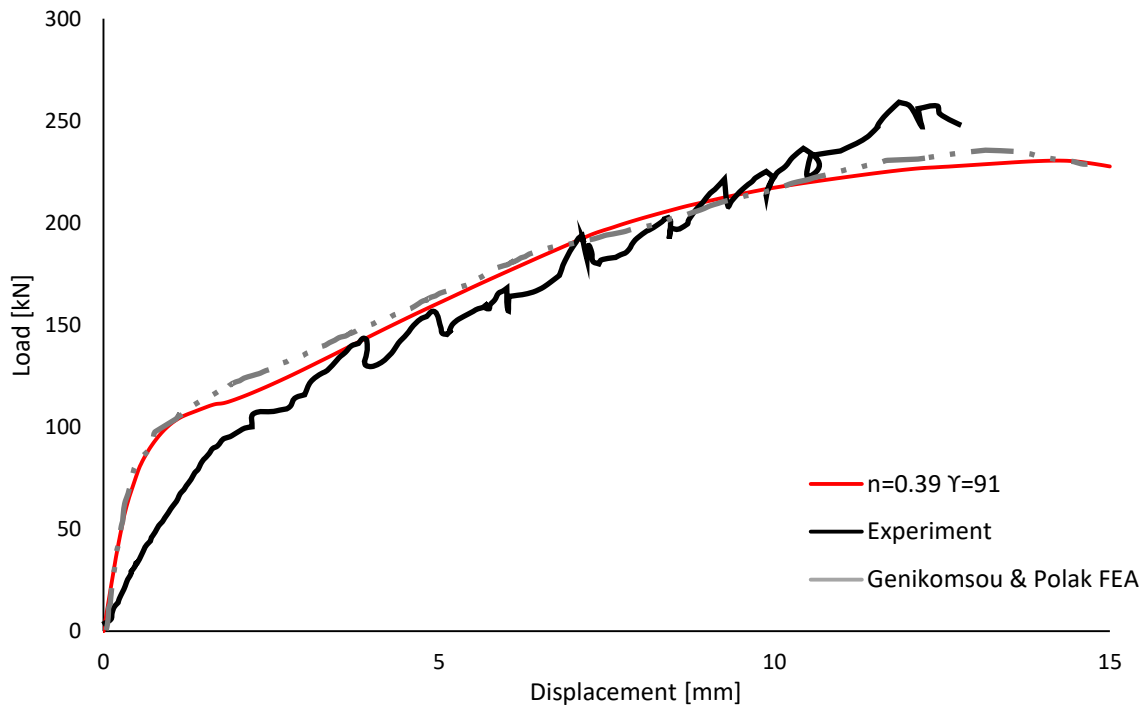


Figure 6-9: FEA SB1 Load vs Displacement verification.

## 6.9 Specimen R200

Data for specimen R200 was part of the experimental program by Pourreza [63]. The details for the slab and results are provided in Chapter 3 of this thesis. The significance of using this slab to verify the material model is that it is outside of the specimens in research papers used to calibrate the model, the experimental set-up is different, it uses high strength concrete, and the slab is thicker than any other slab used in calibration. The weakening function was calculated from Equation (5-18) as  $n = 0.31$  and the ultimate strain factor was calculated from Equation (5-19) as,  $\gamma = 281$ . The resulting load-deflection curve is given in Figure 6-10.

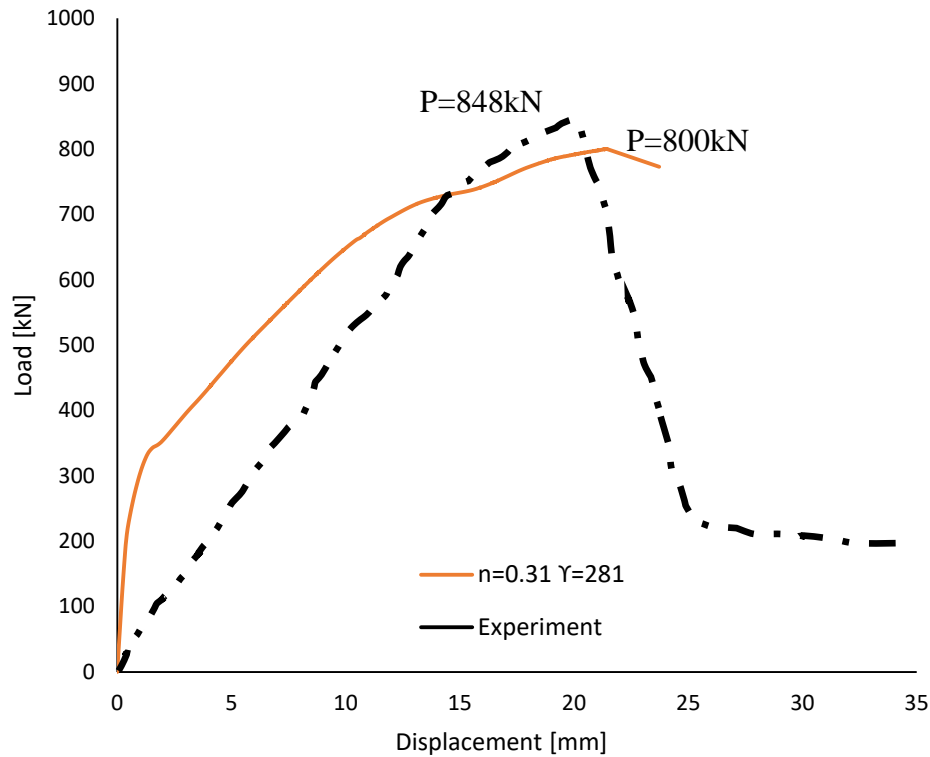


Figure 6-10: FEA R200 load vs displacement verification.

The ultimate punching load from the FEA model was 800 kN which was 6% less than the experimental value. The load-deflection curve from the FEA model was a more realistic representation of concrete up the ultimate punching shear load. It has been shown in previous models that concrete exhibits a high initial stiffness up to the point of cracking then a progressive flattening of the curve up to the point of shear failure. The experimental data for R200 does not capture the initial un-cracked concrete stiffness. Rather the deflection is linear up to the point of cracking. This inconsistency may have been a limitation with the displacement measuring instruments used in the experiment. Even though there are some discrepancies between the FEA and experiment, the FEA model was successful in replicating the punching shear behavior of slab specimen R200.

## 6.10 Summary of Model Verification

A summary of the results obtained from the FEA models is compared to the corresponding experimental data in Table 6.3:

Table 6.3: Summary of FEA vs Experimental Results

| Specimen | Punching Shear Load [kN] |     |        | Peak Load Deflection [mm] |      |        |
|----------|--------------------------|-----|--------|---------------------------|------|--------|
|          | Exp                      | FEA | % Diff | Exp                       | FEA  | % Diff |
| FSB      | 438                      | 440 | -0.5%  | 32.8                      | 26.3 | 22.0%  |
| FCU      | 329                      | 320 | 2.8%   | 18.2                      | 15.2 | 18.0%  |
| FCB      | 361                      | 351 | 2.8%   | 16.3                      | 14.7 | 10.3%  |
| 90BF     | 386                      | 385 | 0.3%   | 33                        | 35   | -5.9%  |
| MU2      | 296                      | 290 | 2.0%   | 22.6                      | 30   | -28.1% |
| MB2*     | 282                      | 360 | -24.3% | 15.1                      | 20   | -27.9% |
| MBF2     | 426                      | 430 | -0.9%  | 28.3                      | 34.7 | -20.3% |
| SB1      | 253                      | 230 | 9.5%   | 12                        | 15   | -22.2% |
| R200     | 848                      | 800 | 5.8%   | 19.9                      | 21.4 | -7.3%  |

\* Experimental results failed in bond and not in punching shear

## Chapter 7

# Conclusions & Recommendations

The literature review demonstrated that the punching shear capacity of reinforced concrete slabs is influenced by the following material properties: concrete compressive strength, flexural reinforcement ratio, inclusion of steel fibers in the concrete mix, and the reinforcing steel yield strength. A review of current finite element analysis (FEA) models revealed that a unified approach to include all of these variables into one coherent and robust model did not exist. The available models were specific to a limited set of criteria and limited verification. As a result, they did not establish a generality that could make them capable in simulating a wide range of concrete slabs.

This thesis successfully developed a finite element model to reasonably predict the punching shear behavior of reinforced concrete slabs over a range of parameters. The model was developed by explicitly defining the two main components used to describe reinforced concrete behavior: the compressive and tensile stress-strain relationships. The compressive stress-strain values were developed from a well-established model by Collins & Mitchell [25] used to describe the full elastic and inelastic range of the compression stress-strain curve of concrete. A general purpose tensile stress-strain relationship is not available in the literature that is capable of representing the tension stiffening effects required to accurately simulate the punching shear behavior of reinforced concrete over a range of parameters. The tension stress-strain model built upon the work from Hus & Mo [44] where they used an exponential decaying function to describe the descending branch of the tensile behavior of reinforced concrete. They provided a

recommendation on the value of the exponential decaying function but never provided a clear analytical expression for quantifying it. The material model presented in this thesis derived an expression for this decaying function, called the ‘weakening function’, as a function of concrete strength, flexural reinforcing ratio, steel fiber volume, and reinforcing yield strength. The model then placed a limit on the horizontal extent of the descending curve by defining the ultimate strain as a factor of the cracking strain. This ‘ultimate strain factor’ was also expressed as a function of concrete strength, flexural reinforcing ratio, steel fiber volume, and reinforcing yield strength.

The Concrete Damaged Plasticity (CDP) model was used to develop the constitutive three-dimensional FEA model. A parametric study was conducted to investigate the numerical parameters inherent in the CDP model and to establish the values to be used in the model development for the dilation angle, viscosity, and mesh size. An expression for the tension stiffening function was developed with respect to the finite element mesh size to avoid any mesh size dependencies in the model.

The model was calibrated from a selection of experimental data from the research of McHarg et al [19], Lee et al [20], and Yang et al [18] and then verified against seven of the remaining slab specimens from those papers and a slab specimen from each of Genikomsou & Polak [56] and Pourezza [63]. The model also predicted the load-deflection response for two slabs where there were possible errors during the physical experiments. The material model showed a strong correlation with all of the experimental data; providing an accurate portrayal of the load-deflection curve including the ultimate punching shear load and the peak deflection.

Recommendations for future work:

1. The material model should be calibrated for a number of limitations that were outside of the range of test specimens used to calibrate and verify the model such as:
  - a. Concrete compressive strengths greater than 90MPa;
  - b. Flexural reinforcing ratios greater than 2.15%
  - c. Steel fiber volumes greater than 0.5%;
  - d. Varying steel fiber aspect ratios;
  - e. Different steel fiber types (i.e. straight, crimped, double hooked, etc.);
  - f. Varying aggregate size and strength.
  - g. Cyclic loading
  - h. FRP reinforcement
2. The material model can be used in conjunction with shear reinforcing to investigate punching shear behavior for shear reinforced slabs.
3. Due to laboratory limitations and financial resources, punching shear tests are usually limited to isolated portions of a slab and a column stub as presented in this paper.  
  
The material model can be employed to model realistic building slabs with multiple columns to study the effects of adjacent geometry and membrane effects.

## Chapter 8

### References

- [1] N. M. Hawkins and M. E. Criswell, "Shear Strength of Slabs Without Shear Reinforcement," *ACI Publication, Shear in Reinforced Concrete*, pp. 677-720, 1974.
- [2] A. Muttoni, "Punching Shear Strength of Reinforced Concrete Slabs without Transverse Reinforcement," *ACI Structural Journal*, vol. 150, no. 4, pp. 440-450, 2008.
- [3] P. E. Regan, "Symmetric Punching of Reinforced Concrete Slabs," *Magazine of Concrete Research*, vol. 38, no. 136, pp. 115-128, 1986.
- [4] Comite Euro-International du Beton, CEB-FIB , "CEB-FIB Model Code 2010," 2010.
- [5] J. Moe, "Shearing Strength of Reinforced Concrete Slabs and Footings Under Concentrated Loads," *Development Department Bulletin D47, Portland Cement Association*, p. 129, 1961.
- [6] O. Graf, "Versuche uber die Widerstandsfahigkeit von Eisenbetonplatten unter konzentrierter Last nahe einem Auflager," *Deutscher Ausschub fur Eisenbeton, Heft 73, Berlin*, p. 16, 1933.
- [7] H. Marzouk and A. Hussein, "Experimental Investigation of the Behavior of High Strength Concrete Slabs," *ACI Structural Journal*, vol. 88, no. 6, pp. 701-713, 1991.
- [8] M. Hallgren, "Punching Shear Capacity of Reinforced High Strength Concrete Slabs," *PhD Thesis, KTH Stockholm, TRITA-BKN*, p. 150, 1996.
- [9] American Concrete Institute, "Building Code Requirements for Structural Concrete (ACI 318-14)," Farmington Hills, MI: American Concrete Institute, 2014.
- [10] CSA Canadian Standards Association , Design of Concrete Structures, Mississauga, On: CSA A23.3-14, 2014.
- [11] European Standard, "Eurocode 2: Design of concrete structures. 1: General rules and rules for buildings," *European Committee for Standardization*, 2004.
- [12] British Standard Institute, "Structural use of concrete," *Standard BS-8110*, 1997.

- [13] R. C. Elstner and E. Hognestad, "Shearing Strength of Reinforced Concrete Slabs," *Journal of the American Concrete Institute*, vol. 53, no. 1, pp. 29-58, 1956.
- [14] S. Alexander and S. Simmonds, "Punching Shear Tests of Concrete Slab-Column Joints Containing Fiber Reinforcement," *ACI Structural Journal*, vol. 89, no. S42, pp. 425-432, 1992.
- [15] S. Kinnunen and H. Nylander, "Punching of Concrete Slabs without Shear Reinforcement," *Transactions of the Royal Institute of Technology*, vol. 158, p. 16, 1960.
- [16] P. E. Regan and M. W. Braestrup, "Punching Shear in Reinforced," *Comite Euro-International du Beton*, vol. 168, p. 232, 1985.
- [17] A. Sherif and W. Dilger, "Punching Failure of a Full Scale High Strength Concrete Flat Slab," *International Workshop on Punching Shear Capacity of RC Slabs*, pp. 235-243, 2000.
- [18] J.-M. Yang, Y.-S. Yoon, W. D. Cook and D. Mitchell, "Punching Shear Behavior of Two-Way Slabs Reinforced with High Strength Steel," *ACI Structural Journal*, vol. 107, no. 4, pp. 468-475, 2010.
- [19] P. McHarg, W. Cook, D. Mitchell and Y. Yoon, "Benefits of Concentrated Slab Reinforcement and Steel Fibers on Performance of Slab-Column Connections," *ACI Structural Journal*, pp. 225-235, 2000.
- [20] J. Lee, Y. Yoon, S. Lee, W. Cook and D. Mitchell, "Enhancing Performance of Slab-Column Connections," *ASCE Journal of Structural Engineering*, vol. 134, no. 3, pp. 448-457, 2008.
- [21] Z. Bazant and Z. Cao, "Size Effect in Punching Shear Failure of Slabs," *ACI Structural Journal*, pp. 44-53, 1987.
- [22] M. H. Harajli, D. Maalouf and H. Khatib, "Effect of Fibers on the Punching Shear Strength of Slab-Column Connections," *Cement & Concrete Composites*, vol. 17, no. 12, pp. 161-170, 1995.
- [23] L. Nguyen-Minh, R. Marian and T. Tran-Quoc, "Punching Shear Capacity of Interior SFRC Slab-Column Connections," *ASCE Journal of Structural Engineering*, vol. 138, no. 5, pp. 613-624, 2012.

- [24] E. Hognestad, "A Study of Combined Bending and Axial Load in Reinforced Concrete," *Bulletin 399, University of Illinois Engineering Experiment Station*, p. 128, 1951.
- [25] M. Collins and D. Mitchell, *Prestressed Concrete Structures*, Englewood Cliffs, NJ: Prentice Hall, 1990, p. 776.
- [26] A. S. Ezeldin and P. N. Balaguru, "Normal and High Strength Fiber Reinforced Concrete Under Compression," *ASCE Journal of Materials in Civil Engineering*, vol. 4, no. 4, 1992.
- [27] L. Hsu and T. Hsu, "Stress-Strain Behaviour of Steel Fiber High Strength Concrete Under Compression," *ACI Structural Journal*, vol. 91, no. 4, pp. 448-457, 1994.
- [28] L. Rizzuti and F. Bencardino, "Effects of Fibre Volume Fraction on the Compressive and Flexural Experimental Behaviour of SFRC," *Contemporary Engineering Sciences*, vol. 7, no. 8, pp. 379-390, 2014.
- [29] S. C. Lee, J. H. Oh and J. Y. Cho, "Compressive Behavior of Fiber-Reinforced Concrete with End-Hooked Steel Fibers," *Materials*, pp. 1442-1458, 2015.
- [30] C. Wang, "Eperimental Investigation of the Behaviorof Steel Fiber Reinforced Concrete," *University of Canterbury (Masters Thesis)*, 2006.
- [31] S.-C. Lee, J.-Y. Cho and F. J. Vecchio, ""Tension-Stiffening Model for Steel Fiber Reinforced Concrete Conctainig Conventional Reinforcement"," *ACI Structural Journal*, pp. 639-648, 2013.
- [32] A. Hillerborg, M. Modeer and P. Petersson, "Analysis of Crack Formation and Crack Growth in Concrete by Means of Fracture Mechanics and Finite Elements," *Cement and Concrete Res*, pp. 773-782, 1976.
- [33] V. E. Saouma, "Lecture Notes," in *Fracture Mechanics*, Boulder, CO, University of Colorado, 2000, pp. Chapter 15 pg 1-13.
- [34] Z. Bazant and B. Oh, "Crack Band Theory for Fracture of Concrete," *Materials and Structures*, pp. 155-177, 1983.
- [35] F. Whittman, K. Rokugo, E. Bruhwiler, H. Mihashi and P. Simonin, "Fracture Energy and Strain Softening of Concrete as Determined by Means of Compact Tension Specimens," *Materials and Structures*, pp. 21-32, 1988.

- [36] J. Barros and J. Cruz, "Fracture Energy of Steel Fiber-Reinforced Concrete," *Mechanics of Composite Materials and Structures*, vol. 8, no. 1, pp. 29-45, 2001.
- [37] M. Teixeira, J. Barros, V. Cunha, B. Moraes-Neto and A. Ventura-Gouveia, "Numerical Simulation of the Punching Shear Behavior of Self-Compacting Fibre Reinforced Flat Slabs", *Construction and Building Materials*, pp. 25-36, 2015.
- [38] G. Tiberti, F. Minelli, G. A. Plizzari and F. J. Vecchio, "Influence of Concrete Strength on Crack Development in SFRC Members", *Cement & Concrete Composites*, pp. 176-185, 2014.
- [39] A. Scanlon and D. Murray, "Time Dependent Deflections of Reinforced Concrete Slab Deflections," *J. Struct. Div.*, pp. 1911-1924, 1974.
- [40] C. Lin and A. Scordelis, "Nonlinear Analysis of RC Shells of General Form," *J. Struct. Div.*, pp. 523-538, 1975.
- [41] R. Nayal and H. Rasheed, "Tension Stiffening Model for Concrete Beams Reinforced with Steel and FRP Bars," *Journal of Materials in Civil Engineering* , pp. 831-841, 2006.
- [42] A. Vebo and A. Ghali, "Moment Curvature Relation of Reinforced Concrete Slabs," *J. Struct. Div.*, pp. 515-531, 1977.
- [43] R. Gilbert and R. Warner, "Tension Stiffening in Reinforced Concrete Slabs," *J. Struct. Div.*, pp. 1885-1900, 1978.
- [44] T. Hsu and Y.-L. Mo, "Unified Theory of Concrete Structures", John Wiley & Sons Inc, 2010.
- [45] H. H. Abrishami and D. Mitchell, "Influence of Steel Fibers on Tension Stiffening", *ACI Structural Journal*, pp. 769-775, 1997.
- [46] A. Naaman and H. Reinhart, "High Performance Fiber Reinforced Cement Composites," *RILEM proceedings Pro 30*, 2003.
- [47] G. I. Rankin, "Punching Failure and Compressive Membrane Action in Reinforced Concrete Slabs," PhD Thesis, 1982.
- [48] G. MacGregor and M. Bartlett, *Reinforced Concrete: Mechanics and Design*, Pearson Canada, 2000.

- [49] B. T. Lim, "Punching Shear Capacity of Flat Slab-Column Junctions," PhD Thesis, 1997.
- [50] P. Bischoff, "Tension Stiffening and Cracking of Steel Fiber-Reinforced Concrete," *Journal of Materials in Civil Engineering*, vol. 15, no. 2, pp. 174-182, 2003.
- [51] D. Ngo and A. C. Scordelis, "Finite Element Analysis of Reinforced Concrete Beams," *ACI Journal*, vol. 64, no. 14, pp. 152-163, 1967.
- [52] CEB-FIB, "Punching of Structural Concrete Slabs," Lausanne, International Federation for Structural Concrete, 2001, pp. 67-109.
- [53] K. Winkler and F. Stangenberg, "'Numerical Analysis of Punching Shear Failure of Reinforced Concrete Slabs'," *2008 Abaqus Users' Conference*, pp. 1-15, 2008.
- [54] K. Youm, J. Kim and J. Moon, "'Punching Shear Failure of Slab with Lightweight Aggregate Concrete (LWAC) and Low Reinforcement Ratio'," *Construction and Building Materials*, pp. 92-102, 2014.
- [55] A. Wosatko, J. Pamin and M. A. Polak, "'Application of Damage-Plasticity Models in Finite Element Analysis of Punching Shear'," *Computers and Structures*, pp. 73-85, 2015.
- [56] A. Genikomsou and M. A. Polak, "'Finite Element Analysis of a Reinforced Concrete Slab-Column Connection using ABAQUS'," in *ASCE Structures Congress*, 2014.
- [57] A. S. Genikomsou and M. A. Polak, "'Finite Element Analysis of Punching Shear of Concrete Slabs Using Damaged Plasticity Model in Abaqus'," *Engineering Structures*, pp. 38-48, 2015a.
- [58] A. Genikomsou and M. A. Polak, "'Damaged Plasticity Modelling of Concrete in Finite Element Analysis of Reinforced Concrete Slabs'," in *9th International Conference on Fracture Mechanics of Concrete and Concrete Structures*, 2015b.
- [59] A. Genikomsou and M. A. Polak, "'Finite Element Analysis of Reinforced Concrete Slabs with Punching Shear Reinforcement'," *ASCE Journal of Structural Engineering*, pp. 1-15, 2016.
- [60] C.-F. Comite Euro-International du Beton, "CEB-FIB Model Code 1990," 1993.
- [61] W. Nana, T. Bui, A. Limam and S. Abouri, "Experimental and Numerical Modelling of Shear Behaviour of Full-scale RC Slabs Under Concentrated Loads," *Structures 10*, pp. 96-116, 2017.

- [62] R. Hawileh, M. Naser and F. Malhas, "Finite Element Modeling of Punching Shear in Two-Way Slabs Reinforced with High-Strength Steel," in *Structures Congress 2013: Bridging Your Passion with Your Profession*, 2013.
- [63] R. Pourreza, "*Investigating the Effects of Hybrid Fibres on the Structural Behaviour of Two-Way Slabs*", Memorial University of Newfoundland, 2014.
- [64] D. Darwin and D. A. W. Pecknold, "Inelastic Model for Cyclic Biaxial Loading of Reinforced Concrete," University of Illinois, Urbana, Illinois, July 1974.
- [65] J. Lubliner, J. Oliver, S. Oller and E. Onate, "A Plastic-Damage Model for Concrete," *International Journal Solids and Structures*, pp. 299-326, 1989.
- [66] J. Lee and G. Fenves, "Plastic-Damage Model for Cyclic Loading of Concrete Structures," *Journal of Engineering Mechanics*, pp. 892-900, 1998.
- [67] H. Kupfer, H. Hilsdorf and H. Rusch, "Behavior of Concrete Under Biaxial Stresses," *ACI Journal*, vol. 66, no. 8, pp. 656-666, 1969.
- [68] P. Kmiecik and M. Kaminski, "Modelling of Reinforced Concrete Structures and Composite Structures with Concrete Strength Degradation Taken into Consideration," *Archives of Civil and Mechanical Engineering*, 2011.
- [69] Abaqus Analysis User's Manual 6.12-3, Dassault Systems Simulia Corp, Providence RI.
- [70] V. Birtel and P. Mark, "'Parameterised Finite Element Modelling of RC Beam Shear Failure'," *2006 Abaqus Users' Conference*, pp. 95-107, 2006.
- [71] T. Belytschko, W. Liu and B. Moran, *Nonlinear Finite Elements for Continua and Structures*, 2nd ed., J. W. & S. Inc, Ed., West Sussex, 2014, p. 804.
- [72] H. Tlemat, K. Pilakoutas and K. Neocleous, "'Modelling of SFRC Using Inverse Finite Element Analysis," *Materials and Structures*, pp. 221-233, 2006.
- [73] P. Grassel and M. Jirasek, "Plastic Model with Non-Local Damage Applied to Concrete," *International Journal for Numerical and Analytical Methods in Geomechanics*, vol. 30, no. 1, pp. 71-90, 2006.
- [74] A. M. Shaaban and H. Gesund, "'Punching Shear Strength of Steel Fiber Reinforced Concrete Flat Plates'," *ACI Structural Journal*, pp. 406-414, 1994.

- [75] A. N. Talbot, ""Reinofrced Concrete Wall Footings and Column Footings.," *Engineering Experiment Station, University of Illonois, Urbana, Bulletin No. 67*, p. 114, 1913.
- [76] J. M. Alwan, A. E. Naaman and W. Hansen, "Pull-Out Work of Steel Fibers From Cementitious Composites: Analytical Investigation," *Cement & Concrete Composites*, pp. 247-255, 1991.
- [77] P. Robins, S. Austin and P. Jones, "Pull-Out Behaviour of Hooked Steel Fibres," *Materials and Structures*, vol. 35, pp. 434-442, 2002.
- [78] M. Cheng and G. Parra-Montesinos, "Evaluation of Steel Fiber Reinforcement for Punching Shear Resistance in Slab-Colun Connections - Part I: Monotonically Increased Load," *ACI Structural Journal*, pp. 101-109, 2010.
- [79] H. Higashiyama, A. Ota and M. Mizukoshi, "Design Equation for Punching Shear Capacity of SFRC Slabs," *International Journal of Concrete Structures and Materials*, pp. 35-42, 2011.
- [80] C. Forsell and A. Holmberg, "Concentrated Load on Concrete Slabs," *Betong*, vol. 31, no. 2, pp. 95-123, 1946.
- [81] R. Evans and M. Marathe, "Microcracking and Stress-Strain Curves for Concrete in Tension," *Materiaux et Constructions*, pp. 61-64, 1968.
- [82] ACI Committee 544, "Design Considerations for Steel Fiber Reinforced Concrete," *ACI Structural Journal*, vol. 85, no. 5, pp. 563-580, 1988.
- [83] ACI Committe 544, "Report on Fiber Reinforced Concrete," *American Concrete Institute*, 1996.
- [84] T. Lim, P. Paramasivam and S. Lee, "Analytical Model for Tensiule Behavior of Steel-Fiber Concrete," *Materials Journal*, vol. 84, no. 4, pp. 286-298, 1987.
- [85] A. Ramaswamy, F. Barzegar and G. Voyiadjis, "Postcracking Formulation for Analysis of RC Structures Based on Secant Stiffness," *Journal of Engineering Mechanics*, vol. 120, no. 12, pp. 2621-2640, 1994.
- [86] M. Duque, F. Ruiz, A. Muttoni and S. J. Foster, "Punching Shear Strength of Steel Fiber Reinforced Concrete Slabs," *Engineering Structures*, vol. 40, pp. 93-94, 2012.

- [87] M. A. Mansur, M. S. Chin and T. H. Wee, "Stress-Strain Relationship of High-Strength Fiber Concrete in Compression," *Journal of Materials in Civil Engineering*, vol. 11, no. 1, pp. 21-29, 1999.